SINTERED NANOPOROUS COPPER DIE-ATTACH INTERCONNECTIONS: SYNTHESIS AND CHARACTERIZATION

A Dissertation
Presented to
The Academic Faculty

by

Kashyap Mohan

In Partial Fulfillment
of the Requirements for the Degree
Doctorate of Philosophy in the
School of Material Science and Engineering

Georgia Institute of Technology
August 2020

SINTERED NANOPOROUS COPPER DIE-ATTACH INTERCONNECTIONS: SYNTHESIS AND CHARACTERIZATION

Approved by:

Dr. Rao R. Tummala, Advisor
School of Electrical and Computer Engineering
Georgia Institute of Technology

Dr. Naresh Thadhani
School of Material Science and Engineering
Georgia Institute of Technology

Dr. Antonia Antoniou, Co-Advisor
School of Mechanical Engineering
Georgia Institute of Technology

Dr. Preet Singh
School of Material Science and Engineering
Georgia Institute of Technology

Dr. Vanessa Smet, Co-Advisor
School of Mechanical Engineering
Georgia Institute of Technology

Date Approved: June 9, 2020

Dedicated to my parents,

Rakesh and Bharti

ACKNOWLEDGEMENTS

I would like to express my sincere gratitude to my advisor, Professor Rao R. Tummala, for providing the opportunity to pursue this interdisciplinary research and for his valuable guidance. I would also like to thank my co-advisors Prof. Vanessa Smet and Prof. Antonia Antoniou for their mentorship and exceptional guidance. I sincerely thank my committee members, Professor Naresh Thadhani, and Professor Preet Singh, for providing their critical feedback.

I would like to thank all the members of my research team at the Georgia Tech 3D System Research Center, especially Ramon, Omkar, Haksun, and Ninad for their support and help. I would also like to acknowledge the support of the Semiconductor Research Consortium (SRC) and our PRC industry partners for their funding and technical support.

Finally, I would like to thank my family for their unconditional love and support in helping me achieve my ambitions.

TABLE OF CONTENTS

LIST OF TABLES

LIST OF FIGURES

LIST OF SYMBOLS AND ABBREVIATIONS

AM	Additive manufacturing
CTE	Coefficient of thermal expansion
DBC	Direct bonded copper
ECA	Electrically conductive adhesives
EDX	Energy dispersive x-ray spectroscopy
EMI	Electromagnetic interference
ECM	Electrochemical migration
FEM	Finite element method
IGBT	Insulated gate bipolar transistors
IMC	Intermetallic compounds
LSV	Linear sweep voltammetry
RoHS	Regulations on hazardous substances
RTP furnace	Rapid thermal processing furnace
SEM	Scanning electron microscope
SLID bonding	Solid-liquid interdiffusion bonding
TLP bonding	Transient liquid phase bonding
WBG devices	Wide bandgap devices
XRD	X-ray diffraction

SUMMARY

Die-attach interconnections form a critical part of any power electronics packaging. Next-generation WBG devices-based power packages require die-attach solutions with excellent electrical and thermal properties and capable of operating at elevated temperatures greater than 200°C. This document proposes an all-copper die-attach joint as the potential next-generation die-attach solution.

Copper interconnections, however, face many processing and reliability challenges. These challenges are: 1) room-temperature oxidation before and after assembly; 3) low diffusivity of Cu below 300°C; 3) high modulus of copper interfaces leading to inadequate deformation and accommodation of non-coplanarities during assembly.

To address the aforementioned challenges, film sintering of nanoporous copper (NP-Cu) films is proposed as a low-cost solution to realize all-Cu interconnections. Nanoporous metals can be thought of as sponge-like materials with nanoscale feature sizes, and, therefore, can also be sintered at low temperatures. In addition, they have the following advantages: 1) low-cost synthesis, compatible with standard lithography processes; 2) high design flexibility to control bondline thickness and final microstructure; 3) absence of organic additives, minimizing risks of voiding due to volatiles; 4) low modulus pre-sintering to compensate for lack of wettability and provide compliance to accommodate surface non-coplanarities during assembly.

To realize the above objective, two research tasks were identified and demonstrated. The first task details the fabrication of nanoporous Cu by chemical

dealloying of electroplated Cu-Zn alloys. An extensive characterization of the Cu-Zn plating bath was carried out which demonstrated the ability of pyrophosphate-based baths to be able to electroplate Cu-Zn alloys in a wide composition range. The Cu-Zn plated films were dealloyed to understand the impact of composition and constituent phases of the Cu-Zn films on dealloyed structure. Based on two key indicators – ligament thickness and residual Zn after dealloying, Zn ~50at.% was identified as the most promising composition for dealloying and fabrication of large-area die-attach films. Using the approach of co-electrodeposition and dealloying of Cu-Zn alloys, both standalone inserts and patterned NP-Cu films were fabricated for assembly. The fabrication results show the versatility of the fabrication approach in the sense that it can be used to fabricate NP-Cu films in several different form-factors for multiple applications using the same baseline process.

In the second task, the effect of the morphology of nanoporous Cu films on their sintering kinetics was explored, followed by the development of assembly parameters to form good metallurgical bonds with bulk-Cu interfaces. Based on the sintering results, 275-300ºC was identified as the optimal bonding temperature. Shear strengths of >40MPa were obtained when the assembly was carried out in forming gas.

In summary, this work demonstrates the potential of NP-Cu as the next generation die-attach material and provides guidelines for wafer-scale fabrication of NP-Cu films.

CHAPTER 1. NEXT-GENERATION DIE-ATTACH INTERCONNECTIONS: STRATEGIC NEEDS, CHALLENGES, AND RESEARCH OBJECTIVES

1.1 Introduction to power electronics

Reducing carbon emissions and mitigating the associated climate change and environmental concerns are global challenges. The Paris Agreement within the United Nations Framework Convention on Climate Change mandates the 189 member countries to pursue coordinated strategies for aggressively reducing the CO2 emissions to keep the increase in global average temperature to well below 2°C above pre-industrial levels [1].

The global transportation and energy sectors are rapidly evolving to keep up with this emerging scenario. In particular, the transportation industry has been aggressively pushing towards the electrification of vehicles. The total share of electric vehicles is expected to go up to 25% by 2025 from 2.4% in 2015 [2]. This demand for higher electrification and efficiency in the transportation and industrial sectors has brought unprecedented requirements for integration, miniaturization, and advancement of ultra-high power electronic systems.

Power electronics can be understood as the technologies that enable efficient power conversion and power storage to control the flow and distribution of electrical energy. Various types of discreet power devices like diodes, MOSFETS, Insulated Gate Bipolar Transistors (IGBT's) are used to perform the above-mentioned functions. The efficiency of power conversion is determined not only by the performance of the devices but also strongly depends on electronic

interconnections or packaging around these devices. Beyond devices, the packaging is essential to ensure the electrical, thermal, and mechanical performances of power electronic systems. For reference, a standard IGBT power module cross-section is shown in Figure 1.1. Various packaging technologies like the substrate, die-attach, wire bonds, encapsulants, etc. are required to be integrated together to manufacture an efficient power module.

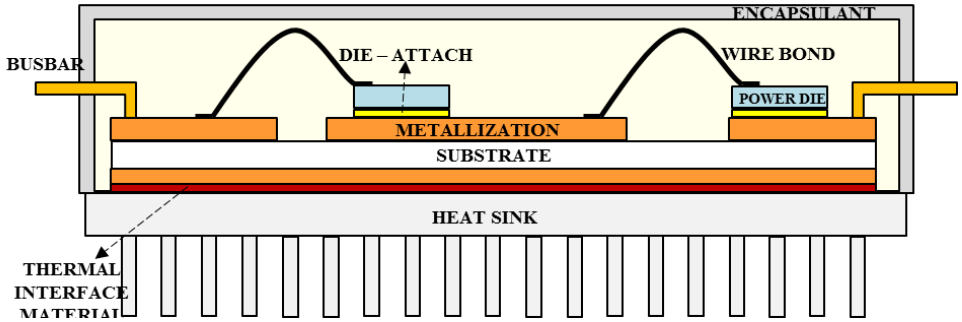

Figure 1.1 Cross-section of a standard IGBT power module.

Today, advances in power electronics to enable operation at switching frequencies, temperatures and current densities beyond that of the current conventional Si-based power modules lie at the heart of the worldwide strategy towards energy-efficient power electronics [3]. One of the possible solutions which has recently gained momentum is the adoption of wide bandgap (WBG) devices such as SiC Schottky diodes and MOSFETs or GaN FETs. These devices can be operated at increased power ratings and switching frequencies as compared to Si devices, enabling a significant reduction in the size of passive components, which results in significant gains in both weight and volume. More importantly, they can theoretically operate reliably at temperatures as high as 500°C, leading to a drastic reduction in thermal management requirements [4, 5]. With the adoption of WBG devices, due to increased power ratings, the junction temperatures are expected to go beyond 200°C as shown in Figure 1.2a. While WBG devices have already fulfilled their promise for increased power efficiencies and densities [6], they are typically packaged using conventional, well-established packaging technologies. These

technologies, though fully qualified for Si power modules, are not optimized for WBG devices, which limits the overall performance and requires the development of better performance materials for packaging.

In the realm of conventional Si devices-based power modules, we see another emerging trend towards new packaging architectures. Multi-chip power modules are being increasingly sought after to enable miniaturization and higher integration, but they come at the cost of increased complexity and higher heat dissipation. In response to increasing power densities and heat generation, double-sided cooling architectures are also gaining traction. Double-sided bonding of heat sinks on both sides of power devices provides multiple heat transfer paths, leading to significant improvement in thermal management. Examples of double-sided cooling structures are reported to allow more than 50% increase in dissipated power [7].

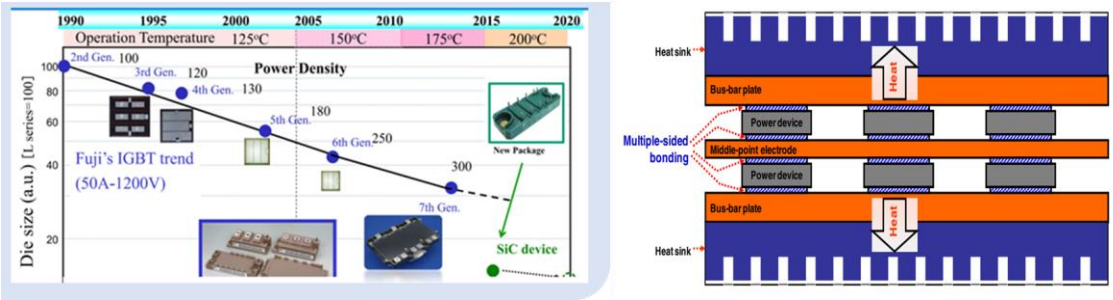

Figure 1.2 a) Increase in current densities with WBG devices will push junction temperatures beyond 200°C [8]; b) Schematic illustrating the idea of multiple stacks of power devices and need for sequential multiple-sided bonding [7].

A conceptual view of an advanced power module package stacked with multiple power devices is shown in Figure 1.2b. The design uses double-side cooling for better thermal management. Both sides of the integrated power devices are bonded to either bus-bar plates (which are connected to the heat sinks) or middle-point electrodes, thus requiring multiple bondings. Such an architecture enables higher integration and package

miniaturization, reduces electromagnetic interference (EMI), and significantly improves the thermal performance.

In the context of the above new developments and the limitations of the current packaging technologies, new packaging materials and integrations are, therefore, required to fully benefit from the properties of WBG devices to make the high-power modules more efficient, smaller, and lighter [9].

1.2 Strategic need for die-attach interconnections

Die-attach interconnections are one of the most critical components of a power electronics package. To ensure that the package is reliable and efficient, the die-attach interconnections must satisfy certain requirements. In most of the power modules, die-attach layers are in immediate contact with the device and therefore, form the primary pathway for transfer of the heat generated by the device. To maximize this heat transfer, the die-attach materials should have high thermal conductivity and should form low thermal resistance interfaces with both the device and the substrate. Besides thermal dissipation, die-attach layers act as electrical interconnections between the vertical-conduction devices and the substrate. Therefore, high electrical conductivity also becomes very critical. High electrical resistance would result in a higher generation of heat by Joule heating, reducing the efficiency of the power conversion. The die-attach layers also act as the mechanical adhesive interfaces between the devices and the substrates. Therefore, the die-attach materials should be able to form strong, stable bonds with both devices and substrate. Due to the large mismatch in the thermal expansion coefficient (CTE) of devices and substrates, thermal expansion stresses are generated in the package which can lead to

die cracking and premature device failures. Ideal die-attach materials should, therefore, provide for CTE matching between devices and substrate to minimize these thermal stresses. Additionally, they should have low modulus to provide for stress-relaxation on the die and high fatigue resistance to absorb the thermal stresses without abrupt failure. Another highly critical property for assessing die-attach materials is their manufacturability and cost. Material cost includes the cost of raw materials as well as processing to form the die-attach. Added to this is the assembly cost, which is dependent on manufacturing throughput and yield. Moreover, low bonding temperatures, pressures, and times are desirable to improve the manufacturability, throughput, and minimize the thermal stresses.

The abovementioned technology trends towards the advancement of power electronics systems help us define strategic requirements for next-generation die-attach materials, as shown in Figure 1.3. First and foremost, die-attach interconnections with thermal stability at temperatures above 250ºC and superior thermal and electrical conductivities are needed in response to increasing junction temperatures and power densities. Die-attach joints with higher thermal dissipation capability would be able to handle higher power densities, leading to greater performance per unit area of the power dies. The new materials should provide higher mechanical reliability as the thermal stresses due to CTE mismatch in the package are expected to increase with increasing temperature cycling ranges. Also, to enable more complex multi-chip package architectures, essential to meet the demand of emerging power electronic systems, the die-attachment method should be able to provide planar and reproducible joints to both sides of the power dies. While higher performance and reliability are mandatory, the cost-sensitive nature of the power electronics sector must equally be kept in mind.

Figure 1.3 Strategic requirements for next-generation die-attach materials.

1.3 Evolution of die-attach interconnection technologies

A wide range of die-attach materials are used in power electronics packaging depending on the type of application and operating requirements. Innovations in die-attach materials have been primarily guided by the need for increased operating temperatures, improved electrical and thermal performances, and enhanced thermo-mechanical reliability of the joints. In this section, a brief and concise description of the evolution of die-attach technologies for high-power modules is given, as shown in Figure 1.4. Key challenges with different technologies have also been listed which helps us in further refining the requirements for the development of next-generation die-attach interconnection systems. A more detailed discussion on the different die-attach technologies has been provided in Chapter 2.

High-Pb solders, e.g. $Pb_{90}Sn_{10}$, remain one of the most widely used die-attach material, particularly for high-power electronics for industrial, automotive, and military applications [10]. Overall, they have a highly desirable set of properties which include low cost, good ductility (elongation of 25%-30%), acceptable thermal (46W/m-K) and electrical conductivities, and low Young's modulus (19GPa) [9]. Moreover, their melting points are greater than 300°C, and therefore they can reliably function at temperatures

beyond 200°C. A major issue with their continued use in the industry is their high toxicity, and, consequently, their adverse impact on health and environment. Various environmental regulations, like Regulations on Hazardous Substances (RoHS) seek to limit and gradually ban the use of Pb-containing solders. To address these concerns, several Pb-free alternatives have emerged and are being actively employed as well. Among them, the most important are Pb-free solder systems, electrically conductive adhesives (ECAs) based on polymers, solid-liquid interdiffusion (SLID) bonding systems, also known as Transient Liquid Phase (TLP) bonding and die-attach processes based on sintering of metal nano- or micro-scale pastes.

Conventional Pb-free, Sn-based solders like $SnCu_{0.7}$ or $SnAg_{3.5}$ have relatively low melting points of 220-230°C, limiting their reliable temperature of use to below 150ºC [11]. At higher temperatures, they are highly susceptible to creep and electromigration and can thus fail prematurely [12, 13]. Although solder systems that can sustain higher temperatures have been proposed, they face their own set of limitations: Au-rich solders have high stiffness and are expensive. Bi-based systems suffer from low thermal conductivity while Zn-based systems exhibit brittleness and poor wettability [9].

ECAs involve the use of polymer resins, generally, epoxies, loaded with metallic flakes of Ag, Au, or Al among other options. These polymer-based adhesives offer the advantages of low cost, relatively low modulus, and ease of processing. They are however limited in their electrical and thermal properties and cannot sustain high temperatures beyond 250ºC because of polymer degradation. Moreover, they form high thermal resistance interfaces with the die and the substrate due to localized segregation of the

polymer on the interface. Thus, the use of ECAs is generally limited to small die sizes and for low-power applications [14].

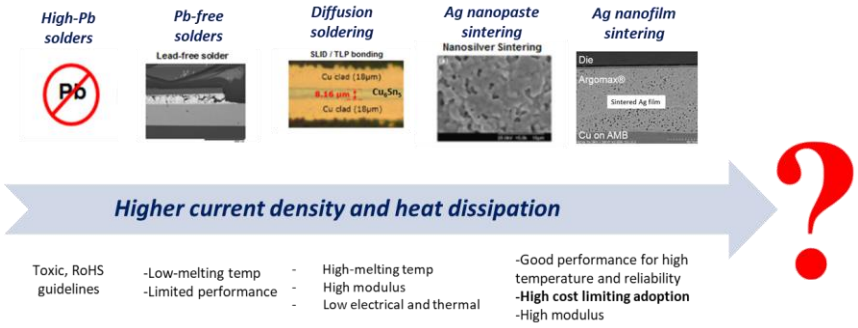

Figure 1.4 Evolution of die-attach technologies in power electronics.

Beyond solders and ECAs, die-attach solutions based on SLID bonding and sintering of metallic nanopastes are being developed for high-power, high-temperature applications. SLID bonding is an emerging technology and has recently been implemented in limited volume production by Infineon in their PrimePack IGBT module. It is based on the formation of high-melting temperature intermetallics (IMCs) between a high melting point component (e.g. Cu, Au, Ag) and a low melting point component (e.g. Sn, In) at processing temperatures slightly exceeding the melting point of the latter. For instance, the Cu-Sn system forms IMCs with melting points higher than 675°C while the joints are formed at normal reflow temperature in the 230-260°C range [15]. The formed intermetallic joints have superior thermal stability and power handling capability and can operate at temperatures much beyond their processing temperature. The fundamental drawbacks of this approach include long annealing time to reach the stable IMC phase, unavoidable formation of shrinkage and Kirkendall voids in the intermetallic joints, degrading their thermal and electrical performances, and the relatively high modulus of

intermetallics (>50GPa), which hinders scalability to large die sizes due to reduced stress relaxation capability [16-18].

Sintering of metal nanopastes, particularly silver (Ag) nanopastes, has gained momentum in the last decade owing to their low-temperature processing due to their high surface area and outstanding performance [19]. These nanopastes are essentially Ag nanoparticles stabilized in a matrix of different organic components that, when sintered, form diffusion-enabled metallurgical joints with metal finish on both the dies and the substrates. The resulting sintered joints have excellent thermal and electrical conductivities as well as high-temperature stability. For instance, commercial Ag nanopastes can be sintered at as low as 250°C. However, despite intensive R&D efforts and excellent properties, adoption of the Ag sintering technology in mass production has been slow due to manufacturability and reliability challenges that are yet to be comprehensively addressed [20].

These challenges originate partly due to the organic additives in the nanopastes and partly due to the inherent limitations of Ag as the material of choice for interconnections. Sintered joints suffer from retained porosity due to partial densification, and voids caused by the evaporation of organic volatiles during the sintering process [21]. Voiding becomes even more of a challenge with increasing die sizes. Pores and voids degrade the mechanical, thermal, and electrical properties of the sintered joints. Further, they are found to coalesce and grow when the joints are subjected to high operating temperatures, which can potentially lead to early failures. Moreover, evaporation of the voluminous organics leads to high shrinkage during the assembly process which makes precise control of bondline thickness a challenge, especially for large die-sizes. Ag, as a material system is costly and

is known for its relatively poor electrochemical migration (ECM) performance [22], which can be a concern in high-power modules. Moreover, the bonding of Ag sintering pastes directly to copper (Cu) metallization is considered difficult due to the oxidation of copper. Therefore, noble interfaces like Au or Ag have to be applied on standard Direct Bonded Copper (DBC) substrates for strong bonding which further increases the overall cost [23].

Another set of challenges originates from the proportional relationship between physical properties (like elastic modulus, thermal and electrical conductivities) and densification. In principle, sintered joints with high densification are desirable for the best electrical and thermal performances. However, higher densification also results in higher modulus joints which can induce severe mechanical stresses on the thin semiconductor devices and limit scalability at large die sizes.

A recent innovation, pioneered by Alpha materials [24], has been the development of sinterable nanoscale Ag films. These films have much reduced organic content as compared to the nanoscale pastes and thus helps address some of the challenges related to the deleterious effects of organics during the assembly process.

To offset the high cost of Ag, the sintering of Cu nanoparticle systems has also recently been getting attention. Cu has comparable electrical and thermal properties to Ag but much lower raw material cost. However, it inherently faces the same limitations as Ag sintering, like the presence of organics and high modulus of sintered joints. Moreover, oxidation of Cu nanoparticles pre, during, and post sintering is an additional challenge that is typically addressed through expensive surface treatments [25], possibly offsetting the

cost advantage. Based on the above discussion, the key advantages and challenges of Ag nanopastes sintered die-attach joints have been summarized in Table 1.1.

Table 1.1 Advantages and key challenges of sintered Ag nanopastes die-attach interconnections.

Die-attach technology	Advantages	Challenges
Ag nanopastes sintering	• Can operate at T>250°C. • Excellent electrical and thermal performances. • Sintering temperatures <250°C.	• Organic additives in Ag nanopastes, resulting in voids after densification. • High-shrinkage due to evaporation of organics leading to warpage after assembly. • High modulus joints as compared to solders. • High cost and poor ECM.

1.4 Next-generation die-attach technology beyond sintered silver: research objectives, technical challenges, and research tasks

It has been discussed in the previous sections that nanosilver sintered joints have become the current state-of-the-art die-attach technology for high-performance systems. To define the key attributes of the next-generation die-attach technology, two key

assumptions are made based on extensive literature survey and discussions with the industry –

i) All-metal joints (e.g. Ag/Au/Cu), without any presence of intermetallic compounds, provide the best of both electrical and thermal performances. For instance, in Ag sintering, the highly densified sintered Ag joints can have properties approaching that of bulk-Ag. In the case of Ag/Au/Cu finish on the dies and the substrates, no intermetallics are formed at the bonding interfaces, resulting in very good high-temperature stability of the interfaces. Therefore, the new material system should be a low-temperature sinterable system which can provide bulk-metal like properties after sintering.

ii) Copper provides a significantly lower cost alternative to silver with almost similar electrical and thermal conductivities. Therefore, copper should be the natural choice for the die-attach material.

Based on the two above mentioned hypothesis, the objective of this research is to identify, design, and demonstrate a low-cost, all-copper die-attach material system capable of sintering at low temperatures (<250°C) and low-pressures (<5MPa). After sintering, the all-copper joints should have high electrical and thermal conductivities as well as high-temperature stability like that of sintered silver joints while having the stress-relaxation capability like that of solders.

The overall objective of the study is divided into two broad areas or tasks. In the following sections, to achieve each objective, the technical challenges are identified, followed by a proposed research task to address those challenges, as shown in Figure 1.5.

1.4.1 Objective 1 – Fabrication of a novel Cu die-attach material system capable of low-temperature, low-pressure assembly by film sintering

Sintering is a solid-state material transport process based on atomic diffusion driven by the reduction of total surface energy and/or interfacial energy. For a material to be sinterable at low-temperatures, the material should be designed such that diffusion mechanisms, in particular, bulk-diffusion mechanisms activate at temperatures significantly lower than its bulk melting point. One of the methods to realize this is to increase the overall surface energy by designing a high specific surface area material system. Ag nanopastes are based on this concept, wherein the silver nanoparticles, because of their extremely high specific surface area, are highly reactive even at room temperature. Due to the high reactivity, the silver nanoparticles tend to form agglomerates which in turn detrimentally impacts the overall surface energy of the system. To stabilize the nanoparticles, organic additives are added which encapsulate the nanoparticles and prevent them from agglomerating. However, as discussed in the previous sections, these organics result in process complexities during sintering and degrade the performance of the sintered joints. A high specific surface energy Cu nanopastes material system will also face the same challenges as Ag nanoparticles/pastes.

To address the above challenges, the first research task involves the design and demonstration of a novel nanoscale Cu interconnection material system with a high specific surface area. The new material system must not rely on organic additives for stabilizing the nanoscale copper to mitigate the challenges faced by silver nanopastes during sintering. Moreover, this material should have low modulus for accommodating surface roughness and non-coplanarities during assembly. The fabrication process must be compatible with

both standard industry processes and wafer-scale processing and the material itself should be scalable in different sizes and form factors.

1.4.2 Objective 2 – Demonstration of Cu-Cu joints by film sintering

The electrical and thermal conductivities are directly proportional to the densification after sintering. Very high densification of >90% after sintering is desirable to achieve bulk-Cu like properties [26]. The high surface energy of the novel nanoscale Cu interconnection material is a prerequisite but does not necessarily guarantee high densification under low-temperature, low-pressure assembly conditions. Moreover, densification and the ability of the die-attach material to form metallurgical bonds with the metallizations on the dies and the substrates are two parallel, and possibly competing mechanisms during the assembly process. Greater and faster densification of the die-attach material during the assembly process will decrease its overall surface energy and can detrimentally impact its ability to form metallurgical bonds with the die and substrate metallizations. The nanoscale Cu system, due to its high reactivity, is also expected to form surface oxides, which are known to retard the densification process during sintering.

To address the above-mentioned challenges, the second research task involves understanding the sintering kinetics of the novel nanoscale Cu system, evaluating the effect of oxides on sintering, and designing the assembly process to achieve the highest densification after sintering with seamlessly bonded, void-free die-attach-to-metal interfaces.

		Research Focus		Target	Prior art vs. proposed			Technical challenges (TC)	Research Tasks
					Ag paste	Ag films	Cu paste (Research)		
1	Before assembly	Novel Cu die-attach material system capable of low-temperature, low-pressure assembly	Fabrication	Preforms, directly on wafer	Printing	Preforms	Printing	High reactivity → difficult to stabilize material, oxidation	Design and demonstration of nanoscale, solid-state, low-modulus organics-free Cu interconnection material
			Thickness	Easily tailorable 5-50um	Multiple printings	Tailorable	Multiple printings		
2	After assembly	Sintering and die-attach joint characterization	Shear strength	>40 MPa	20-50	30-50	~25	Incomplete and uncontrolled densification after sintering, voids at interfaces	Material and assembly process design for very high densification and joint shear strengths by understanding the sintering kinetics

Figure 1.5 Key objectives, associated challenges, and research tasks proposed for this research.

CHAPTER 2. LITERATURE SURVEY OF HIGH-TEMPERATURE DIE-ATTACH TECHNOLOGIES

High Pb-based solders, $Pb_{95}Sn_5$ and $Pb_{90}Sn_{10}$, with melting points of 310°C and 305°C, respectively, have been the workhorse die-attach materials in the power electronics industry. They have highly desirable properties such as good wettability, high ductility, low modulus, acceptable thermal conductivity (~35W/m.K) [27], high thermo-mechanical reliability, good corrosion resistance, among other beneficial attributes. However, due to the toxicity of lead and RoHS guidelines, efforts are being made to replace high-Pb based solders with other reliable high-temperature die-attach alternatives.

A wide range of die-attachment methods is being considered for replacing high-Pb solders for high-temperature die-attach applications. Amongst Pb-free solders, solders like Au-Ge, Zn-Al, and Bi-Ag, which have been around since the 1980s [28, 29], are the most widely considered choices. TLP bonding is another promising approach and has been applied to many metallic systems throughout the ages (Au-Sn, Au-In, Cu-Sn, Cu-Ni). It has been traditionally used to bond metals, ceramics, and composites and was first suggested for use as a bonding material in aerospace and electronic applications in the early 1990s [30]. The last considered approach is based on the low-temperature solid-state sintering of Ag/Cu nanoparticles. The origins of the sintering of Ag micro-scale particles for joining in electronic applications can be traced to the early 1990s [31]. In the early 2000s, the reduction in required sintering temperature and pressure with the use of nanoscale Ag pastes was demonstrated [32]. This landmark study led to intense research towards advances in sintered nano and micro-scale Ag pastes technology. Today Ag pastes

sintering is a maturing technology and the current state-of-the-art for high-temperature die-attach applications. More recently, in the last few years, to offset the high cost of Ag, the sintering of Cu particles is also gaining attention [33]. However, this technology is still in the early phase of development and has immense potential for further research and improvements. The evolution of high-temperature die-attach technologies is shown in Figure 1.4.

In the following sections, the above-mentioned alternative high-temperature die-attach technologies based on high-temperature Pb-free solders, TLP bonding, and solid-state sintering are reviewed in more details from the published literature.

2.1 High-temperature solders

Table 2.1 lists the compositions and melting points of most known and used Pb-free solders. They can be divided into two groups based on high-temperature requirements less than or greater than 250°C.

Sn-based solders made by alloying Sn with Ag/Cu with additions of In, Bi or Sb are widely considered for replacing the Pb-based solders. However, these solders have melting points in the range of 180-230°C, limiting their maximum operating temperatures to <150°C [13].

Amongst the high-temperature solder alloys, the Au-Sn eutectic solder system is the most commonly used. It has a melting point of ~280°C. The thermal and electrical conductivities of $Au_{80}Sn_{20}$ are 57 W/m.K and 16.4 x 10^{-8} Ω·cm, respectively. Au-Ge, Au-Si, and Au-In eutectic solders with melting points of 356°C, 363°C and 521°C,

respectively, have also been explored. Au-Ge and Au-Si solder alloys showed good stability during thermal storage at 325°C, thus demonstrating their good high-temperature stability as shown in Figure 2.1. However, the high cost of Au remains a major challenge in the widespread adoption of these solder systems [9].

Table 2.1 Pb-free solder compositions and melting temperatures [34].

Classification	Solder Type	Composition	Melting Temperature (°C)
Melting temperature < 250°C	Sn-Bi	Sn63 Pb37	183
	Bi-Sn	Bi58 Sn42	138
	Sn-In-Ag	Sn77.2 In20 Ag2.8	187
	Sn-Ag	Sn96.5 Ag3.5	221
	Sn-Cu	Sn99 Cu1	227
	SAC 305	Sn96.5 Ag3.0 Cu 0.5	217
	SAC 387	Sn 96.5 Ag 3.8 Cu 0.7	217
	Sn-Sb	Sn95 Sb5	240
	Sn-Bi-Ag	Sn91.8 Bi4.8 Ag3.4	213
Melting temperature > 250°C	Sn-Sb	Sn90 Sb10	250-272
	Bi-Ag	Ag11 Bi 89	262-360
	Au-Sn	Au80 Sn 20	~280
	Au-Ge	Au88 Ge 12	~356
	Zn-Al	Zn95 Al5	~382
	Ge-Al	Ge55 Al45	~424

Bi-Ag alloys have the right melting temperature range to be considered as an option for replacement of Au-Sn eutectic solders. However, they suffer from low ductility and poor wettability [9]. Indium Corporation has developed a mixed alloy technology called BiAgX^{TM}, in which BiAg alloy (main component) particles were alloyed with other

secondary alloy particles like BiSn [34]. These secondary alloy elements react with surface finish materials and provide the required wetting. BiAgX^{TM} mixed solder technology showed higher shear strength both after thermal storage (200°C for 500h) and thermal cycling (-55 to 125°C for 2000 cycles) as compared to high-Pb containing solder, $Pb_5Sn_{2.5}Ag$.

In contrast to the costly Au/Ag-based solders, the Zn-Al solder system is cost-effective and has a high melting point of ~382°C. Zn-Al solder joints have been reported to have good stability during storage at 200°C as can be seen in Figure 2.1. However, its use at high temperatures has been limited by the low substrate wettability and self-fracturing of the solder layer after soldering due to the growth of brittle intermetallics.

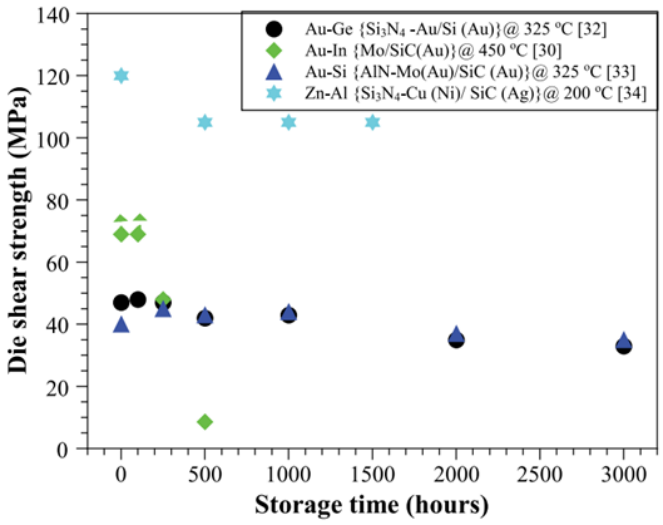

Figure 2.1 Variations of die shear strength during thermal storage for different Pb-free high-temperature solders [9].

Major advantages associated with using high-temperature Pb-free solders for die-attachment are: i) ability to rework as processing temperatures are the same as the melting

temperatures, ii) pressureless, reflow-based bonding processes that result in reduced process complexities and high throughput.

In addition to specific challenges associated with each solder system, high-temperature solders, in general, have a few drawbacks. First, their very high melting points also limit the adoption of these solders, as these processing temperatures can be prohibitively high and can damage other components of the power modules. Moreover, solder-based bonding technologies do not facilitate sequential bonding. The lack of sequential bonding leads to a complex assembly process for emerging multichip or double-sided bonded packages and can lead to module failures due to potential issues such as misalignment or solder overflow [7].

2.2 Transient Liquid Phase (TLP) Bonding

TLP bonding, also known as SLID bonding, is a die-attachment process based on solid-liquid interdiffusion, where a low melting point material (e.g. Sn, In) melts, diffuses and reacts with a high melting point material (e.g. Cu, Ni, Ag, Au) to transform into intermetallic compounds (IMCs) as shown in Figure 2.2 [7]. These resulting IMCs generally have considerably higher melting points (>350°C) than the operating temperatures expected to be observed by advanced power modules. Currently, various material combinations such as Cu-Sn, Ni-Sn, Au-In, Ag-In are under investigation to understand their suitability as an optimum die-attachment solution [7, 16-18, 35].

TLP bonding technologies, because of the high melting point of the IMCs, are well-suited for high-temperature operations as compared to conventional solders. The bonding is usually carried out at temperatures greater than the melting point of low-temperature

melting constituents. This temperature is usually less than 250°C. Moreover, since the melting point of IMCs is much higher than the process temperatures, TLP bonding is repeatable and TLP materials can be used for sequential bonding, as demonstrated by Toyota [7]. As has been pointed out earlier, sequential bonding is a major constraint with solders. The thermal and electrical conductivities of IMCs also fare well when compared to high-Pb solders as highlighted in Table 2.2.

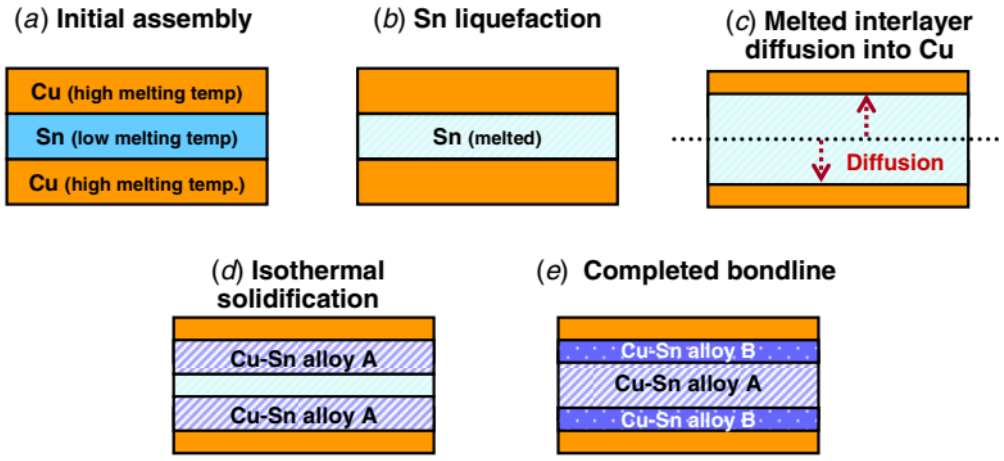

Figure 2.2 Cu-Sn TLP bonding stages [7].

A major challenge with TLP bonding is the high modulus of IMCs as compared to conventional high-Pb solders [36]. The high modulus of the intermetallic-based die-attach joints reduces the fatigue resistance of the joints, leading to a build-up of residual stresses during thermal cycling in operation, and results in the degradation of system-level thermo-mechanical reliability. Moreover, TLP bonding is specific to the surfaces to be bonded, therefore it has a narrower range of surface compatibility than solders, and no rework is possible due to the high-temperature melting points of the bonds formed [35]. Most often, due to the complex phase diagrams of TLP materials, multiple IMCs are formed during

TLP bonding. At high operating temperatures, the IMC structure evolves and can result in the formation of Kirkendall voids, deleteriously affecting the reliability of TLP bonds [37]. Achieving a joint with void-free interfaces and a homogeneous formation of IMCs are the major parameters to be controlled during TLP bonding.

2.3 Solid-state sintered die-attach materials

The third die-attachment approach capable of operating at higher temperatures is based on solid-state sintering of metal particles to form bulk metal like joints. Though the sintering of Au, Ag, and Cu particles has been demonstrated in recent times for interconnection applications, this chapter will mainly focus on Ag sintering because of the high maturity of the technology. In this section, the physical basis of the sintering process is briefly discussed, followed by recent results on sintered Ag die-attach joints. Next, technological challenges hindering the mass adoption of Ag sintering are detailed. Lastly, recent efforts to overcome these challenges are discussed. A very brief mention is also made on the advantages and advances made in the recently emerging technology based on the sintering of Cu particles.

2.3.1 Sintered Ag die-attach material

In the quest for developing high-temperature die-attach technologies, solid-state sintering, especially of Ag pastes systems, provides an attractive solution. The decrease in particle sizes to micro-scale and below results in enhanced surface energy of the particles. The thermodynamic driving force σ for sintering can be expressed equation (1):

$$\sigma = \gamma\kappa = \gamma\left[\frac{1}{R1} - \frac{1}{R2}\right] \quad (1)$$

where γ is specific surface energy, κ is curvature, and R1 and R2 are the principal radii of curvature of a particle surface. It can easily be shown that the driving force for sintering would be two magnitudes higher when the particle size is decreased from 1,000 nm to 10 nm. The specific surface energy γ also increases with decreasing particle size in the nanometer scale due to an increase in the number of defects per unit area, which further contributes to enhancing the sinterability of micro/nano-scale powders.

During the sintering of such a particle system, the particles have enhanced diffusivity and therefore can sinter and densify at much lower temperatures as compared to the bulk melting point. For example, silver has a bulk melting point of 970°C, however, nanosilver particles can be sintered at much lower temperatures in the range of 150 – 300°C [38]. Such a sintered silver die-attach can theoretically operate at temperatures beyond 500°C and therefore, like SLID bonding, helps in decoupling operating temperatures from processing temperatures. The other very attractive advantages of sintered metallic joints are their much higher electrical and thermal conductivities compared to both solders and SLID bonding technologies, as shown in Table 2.2.

Table 2.2 Comparison of different die-attach bonding technologies for power modules.

	Lead-free solders (Sn-Ag, Sn-Au)	High-Pb solder (Toxic)	Diffusion soldering (Cu-Sn)	Sintered joints	
				Ag paste	Cu paste (Research)
Operating temperature (°C)	<175	<275	>250	250-500	250-500
Bonding pressure (MPa)	Reflow	Reflow	0-20	0-20	5-40
Thermal conductivity (W/m.K)	60-80	55-60	~70	180-200	<100
Material formulations	Flux	Flux	Pastes, stack plating with precise composition	Complex organic additives	Complex organic additives
Shrinkage in assembly / modulus after assembly (Stress in/after assembly)	Low/Low	Low/Low	Low-Medium/High	High/tailorable modulus	High/tailorable modulus * Cu modulus higher than silver
Microstructure evolution under thermal and power cycling	Intermetallics	Intermetallics	Kirkendall voiding	Porosity evolution	Porosity evolution

2.3.2 Formulation and processing of Ag pastes:

Ag sintering pastes, in general, consists of Ag particles dispersed in different organic additives such as binders, thinners, resins, and surfactants. Binders and thinners are added to adjust the viscosity and the printability of the pastes. Surfactants are used to encapsulate the Ag particles, and therefore protect them from agglomeration and corrosion. Resins are added to tailor the properties of sintered Ag joints. Ag sinter paste is printed or dispensed on the substrate, die is placed on top and the paste is sintered under temperatures between 200-300°C to form the sintered joint. For larger die-sizes or enhanced joint properties, bonding pressures up to 40MPa are also applied [39].

Based on the particle sizes, the formulation of pastes can be broadly divided into three categories, namely, micro-scale Ag pastes, hybrid Ag pastes, and nano-scale Ag pastes [39]. Micro-scale Ag pastes have a long history of development compared to the others and consist of micron-sized Ag particles, with typical sizes less than 15μm, mixed with organic solvents. Nano-scale Ag sinter pastes, as the name suggests, consist of particles typically less than 100nm. The increase in the surface area provides more driving force for sintering as compared to micron-sized particles and therefore, high densification can be achieved at comparatively lower temperatures and pressures. However, increased reactivity of the particles also creates some challenges. On exposure to the ambient environment, the particles can rapidly oxidize and form oxide coatings, that can inhibit sintering. There is also a risk of self-agglomeration of particles, which can reduce the reactivity of particles. Current paste formulations employ the use of organic additives called surfactants, which act as capping agents, prevent corrosion and agglomeration of particles, and help in delaying low-temperature non-densifying surface diffusion mechanisms. Hybrid Ag pastes contain a mix of nano/sub-micron-sized particles mixed with micron-scale flakes [40]. It helps to reduce cost, improves initial packing density, and reduces the volume of organics needed to stabilize the paste. The micro-flakes play the role of a skeleton, and nano/sub-micron particles improve the interconnection and fill the voids between flakes. On the sintering of hybrid pastes, high-density joints with low levels of residual organics can be achieved.

The processing of Ag sinter pastes can be classified into two broad categories based on the application of a load during the sintering process – pressureless and pressure-assisted sintering [20]. The basic steps for processing are:

Printing on wafer/die → low-temperature preheat →wafer dicing (optional) → die placement → sintering

Printing of Ag pastes onto the substrates is followed by a low-temperature preheat process. The temperature is usually between 50-100°C, enough to evaporate the volatile organic solvents in the paste but not high enough to initiate sintering. After drying the paste, silicon dies are attached to the printed substrate with just enough force to provide temporary adhesion. After this step, the paste is sintered at temperatures of more than 200°C with or without the bonding pressure. This pressure sintering step can be performed on dies, one by one, or together (gang or collective bonding) if the geometry and equipment permits. A pressureless joint will have inferior mechanical, thermal, and electrical properties as compared to the pressure-assisted sintered joints and therefore, lower reliability as well.

2.3.3 Parameters affecting sintered die-attach joint properties

Sintering is a complex process and the final mechanical, thermal, and electrical performances of sintered die-attach joints depend on the complex interaction of several factors. The impacting factors can be broadly classified into three categories, as shown in Figure 2.3. Schematic highlighting the complex nature of the sintering process and various factors that affect the properties of sintered joints [39].

- Design factors such as die size, required thickness of the joints (bondline thickness), substrate metallization, and roughness;

- Process factors such as the sintering temperature, pressure, time and environment;

- Ag paste composition such as the formulation of pastes, as has already been discussed in the previous sections.

Among all these factors, the design factors are generally fixed as per the requirements of the application. To obtain the final desired properties, say for a given die-size, metallization, and joint thickness, the process parameters and paste formulations are optimized. In general, higher sintering temperatures and pressures enable faster sintering and higher densification, resulting in better initial shear strength of the joints.

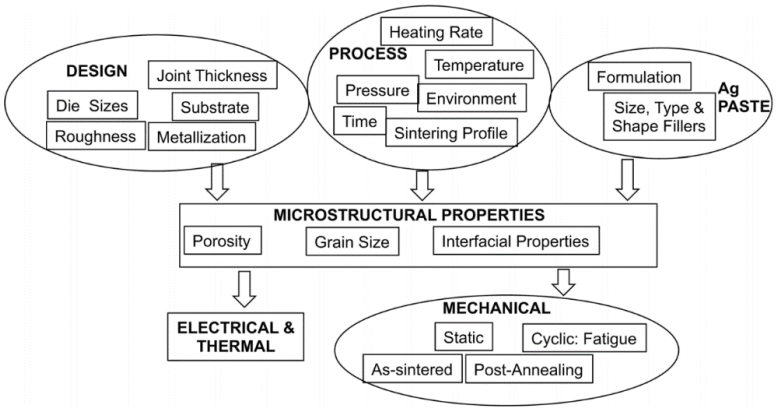

Figure 2.3 Schematic highlighting the complex nature of the sintering process and various factors that affect the properties of sintered joints [39].

Figure 2.4 shows the effect of particle size distribution on the shear strengths reported in different publications for pressureless sintering [41]. As can be seen, the maximum average shear strengths were observed for two main size distributions: <50nm, and nano + micro mix. Less than 50nm particle sizes are expected to show higher shear strengths because of the higher driving force for sintering. On the other hand, hybrid particles can provide a very high initial packing density and therefore higher densification after sintering.

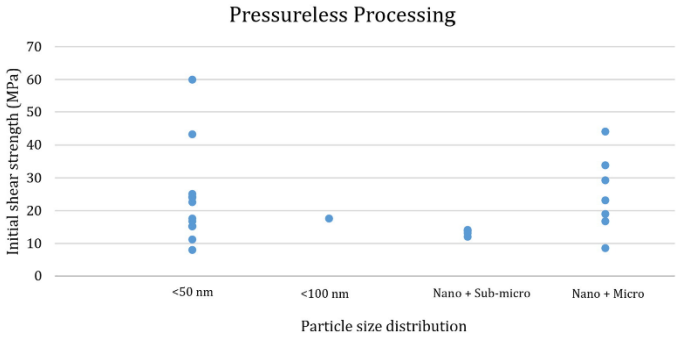

Figure 2.4 Variation of the sintered Ag joints initial shear strengths with the particle size distribution [41].

The application of external pressure during sintering helps in improving the mechanical contact between the particles and between the particles and the bonding interfaces, thereby creating more efficient pathways for atomic diffusion and enabling higher densification. The effect of sintering pressure on the average of initial shear strengths reported in different publications is shown in Figure 2.5 [41]. As expected, an increase in sintering pressure resulted in higher shear strength of the sintered silver joints. However, it has been reported that the application of pressure beyond a limit can negatively impact the joint shear strengths. This was attributed to a very high initial compaction of the particles which hindered the outgassing of decomposed organics from the die-attach joints [42].

Sintering temperature and dwell time at peak sintering temperature are another important set of parameters impacting the shear strengths of the die-attach joints. During sintering, both densification and coarsening of grain structure compete simultaneously. A sufficiently high peak temperature is required for enabling diffusion-led densification of the joints. However, too high a dwell time or peak sintering temperature can lead to coarsening and an increase in pore sizes inside the die-attach joints. This can have a

detrimental impact on the joint shear strengths. For example, an increase in the shear strength of the die-attach joints from 10MPa to 25MPa was reported by increasing the peak sintering temperature from 220C to 250°C [43]. However, no further increase was reported on further increasing the temperature to 270°C, indicating that the temperature increase within the 250-270°C range did not have a significant impact on the densification of the joints.

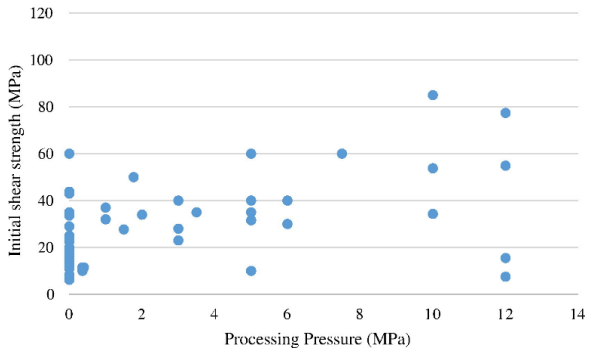

Figure 2.5 Variation of the sintered Ag joints initial shear strengths with processing pressure [41].

The effect of three different substrate metallizations - Ag, Au, and Cu - on the average of initial shear strength is shown in Figure 2.6 [41]. It was observed that Ag metallization gave slightly better performance, but overall, all three metallizations were found compatible with silver sintering. However, contrasting results can also be found in the literature, wherein Ag sintering on Cu metallizations resulted in poor bond quality due to the presence of native oxides on the Cu surface [44].

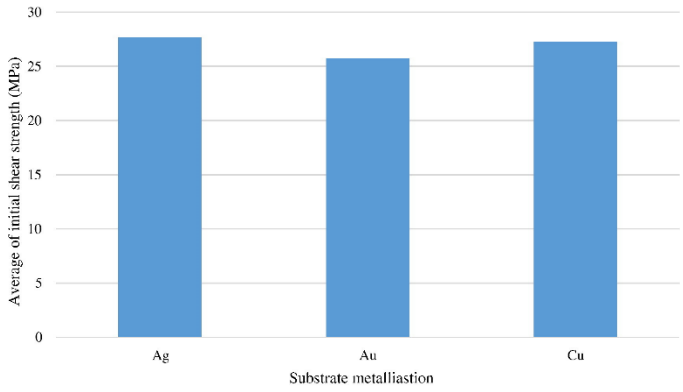

Figure 2.6 Variation of the sintered Ag joints average of initial shear strengths with different substrate metallizations [41].

In conclusion, sintering is a complex process and as discussed above, the final joint properties are dependent on several factors. This makes it very difficult to provide a universal process and design recommendations that can be applied across all applications. Rather, the best approach is to understand the application, extract the die-attach joint requirements, and tailor the process and paste formulations to meet those requirements. This process can be prohibitively expensive and time-consuming and requires the end-user to work closely with the material supplier.

2.3.4 Reliability of sintered silver die-attach joints

As discussed in the previous section, the mechanical properties of the sintered Ag die-attach joints are significantly impacted by the processing parameters. However, a few general trends can be extracted from the literature on the reliability of sintered silver joints. The sintered Ag joints when subjected to thermal aging, an increase in the shear strength was generally observed followed by a subsequent drop in the shear strength [20] as shown in Figure 2.7. During the initial phase of thermal aging, the sintered joints continue to undergo densification. Additionally, the Ag atoms from the sintered joints also diffused

into the bonding metallizations, strengthening the joints. However, during the later phase of thermal aging, grain growth, and an increase in the pore sizes due to diffusion-led coarsening resulted in a drop in the shear strengths [45].

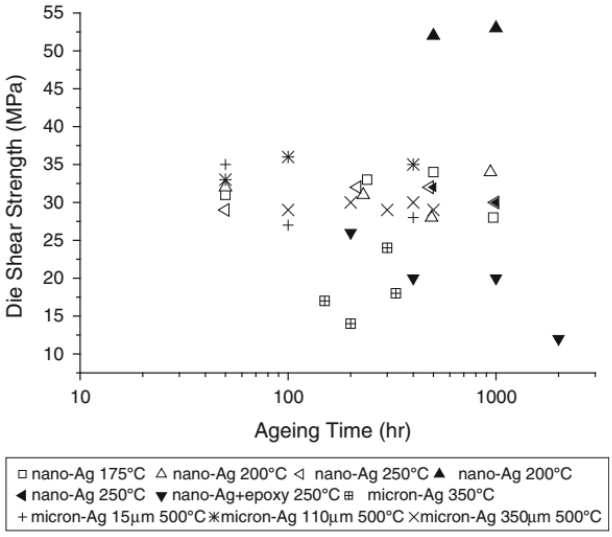

Figure 2.7 Variation of average die shear strength of sintered Ag joints under high-temperature storage [20].

The shear strength variation with thermal cycling showed a monotonically decreasing trend with an increase in the number of thermal cycles as shown in Figure 2.8 [46]. This drop was attributed to the generation of cracks due to the thermal stresses induced by CTE mismatch [45]. Multiple reports have shown that sintered Ag joints can survive a higher number of thermal cycles as compared to $Pb_{95}Sn_5$ or SAC solder alloys [12, 45, 46] and attributed it to the low modulus of sintered Ag joints with residual porosity, especially at elevated temperatures.

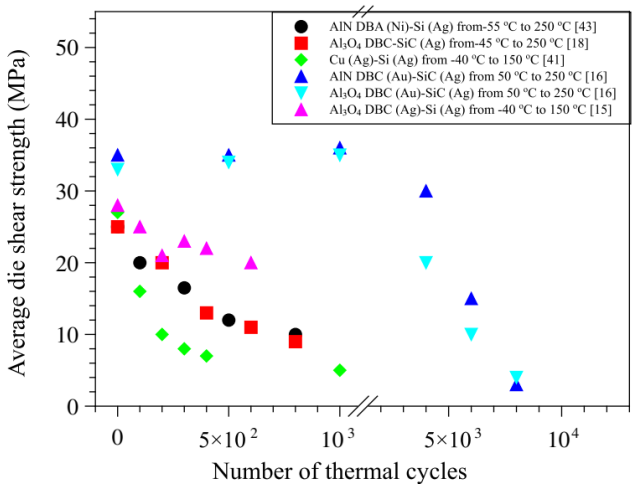

Figure 2.8 Variation of average die shear strength of sintered Ag joints with thermal cycling [20, 46].

2.3.5 Modeling and lifetime predictions of sintered silver die-attach joints

Another important aspect of the reliability characterization of a die-attach material is its lifetime prediction models. Sintering of Ag particles is a relatively new die-attach approach and the reports in the literature on the dependence of physical properties of sintered silver joints on density, porous structure, and aging time and temperature are rather limited [47]. In one such study, it was found that for porosity < 20%, the elastic properties were mainly dependent on the density and were independent of the pores structure and spatial distribution [48]. However, material properties like ultimate tensile stress and elongation showed a strong dependence on the porous structure as well [49]. A few studies have also looked at the relationship between pore structure and thermal conductivity of the sintered Ag joints [47, 50]. It was found that thermal conductivity was mainly dependent on the pore volume fraction, especially for porosity values. A weak dependence on the pore morphology and distribution was also reported with an increase in the porosity [47]. Due to the limited number of such studies, the reliability modeling of sintered Ag joints using

suitable constitutive models is very challenging. A few attempts have also been made to predict the lifetime of the joints using FEM modeling based on the Anand Model [51, 52]. The Anand model parameters for sintered Ag joints were reported by CPES using silver pastes from NBE Tech [53]. However, the dependence of Anand model parameters on the evolution of porosity with thermal aging is not considered which can lead to misleading simulation results [54].

2.3.6 Manufacturing challenges associated with silver sintering

Residual organics in sintered joints [21]: Organic additives play an important role in pastes formulation. However, the presence of these additives also adds to the process complexities. Given the huge specific surface area of nanomaterials, the absolute amount of this coating layer can be considerable, and its residue in the sintered Ag joints can also be significant. It is highly desirable to get rid of the organics as the presence of organics during sintering can inhibit densification by acting as a barrier layer between Ag particles, thus degrading the properties of the joints. Moreover, organics residue can also accelerate the corrosion of the joints.

High modulus of sintered joints [26]: Highly sintered nano-Ag pastes can have a higher modulus as compared to eutectic solders. For instance, at densification levels exceeding 90%, the modulus of the sintered joints can exceed 60GPa. This can induce high stresses on the die during bonding as well as during operation and can result in die cracking.

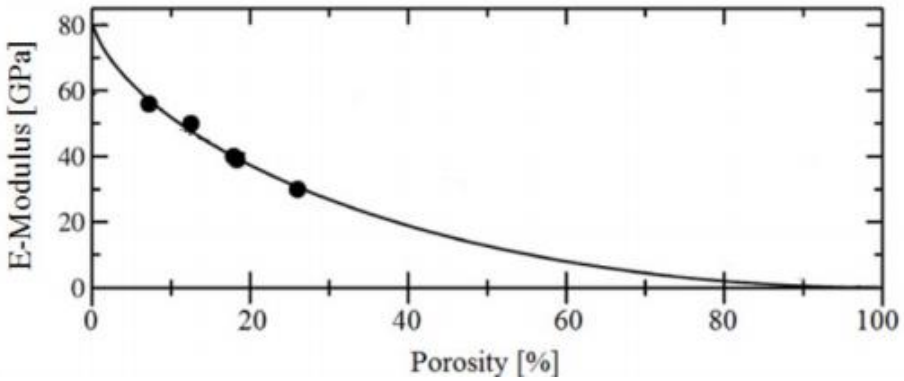

Figure 2.9 Relationship between elastic modulus and porosity in sintered Ag at 25°C [26].

Reliability challenges at large die sizes [55-57]: An increase in die sizes worsens the challenge of residual organics in the sintered joints. The most commonly employed method to remove the organics is decomposition either due to temperature (e.g. volatile solvents like toluene) or through reaction with an oxidizing agent. This decomposition of the organic additives produces gaseous by-products which, if trapped in the sintered joints, can cause reliability issues, including a decrease in shear strength or, in the worst case, even catastrophic failure by delamination. The problem of efficient venting of gaseous by-products during sintering becomes more severe at large die size, as shown in Figure 2.10. Moreover, the thermal stresses during thermal cycling due to CTE mismatch get further exacerbated at large die sizes and can severely impact the reliability of packages with high-modulus sintered silver joints.

Microstructural evolution during operation [45, 46]: With the rapid advancement and commercialization of WBG devices, the maximum junction temperatures are expected to reach 200°C and beyond. Under such aggressive high-temperature conditions, the remnant porosity in the sintered joints starts to evolve and can coalesce together to form

bigger pores. These pores can act as crack initiation sites and may result in failure either from the degradation of the joint's properties, or, in the worst case, complete delamination. Various studies have confirmed a decrease in the shear strength of joints with time subjected to either aggressive thermal aging or thermal cycling. There is also a lot of variation in the reported lifetime the joints can sustain without showing a significant reduction in their properties. This also impacts the mass adoption of the technology, as extensive qualification cycles must be run for each new package design.

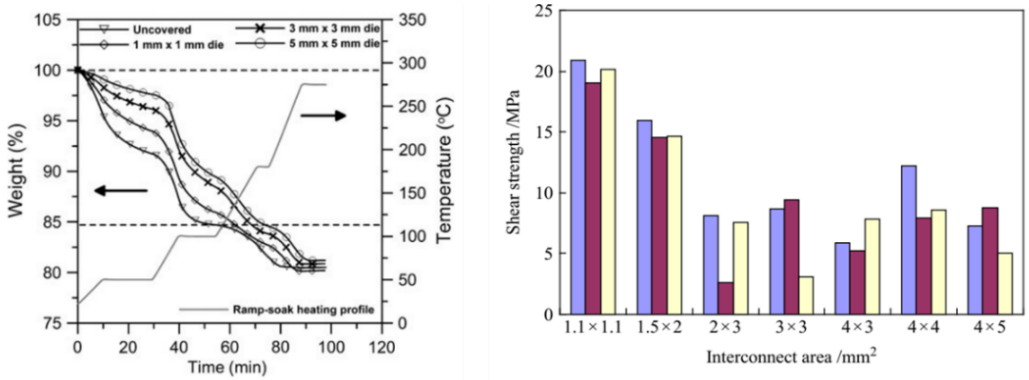

Figure 2.10 a) Increase in residual organics weight percentage with an increase in the joint area [57]; b) Shear strength variation with interconnect area for silver sintered joints [56].

Ag electrochemical migration (ECM): Ag and, by extension, sintered Ag are amongst the most susceptible to ECM failure among different metals. ECM issues associated with Ag sintering and Ag solders are well documented [22]. The presence of external electric field/bias, in combination with moisture and high temperatures, can create favorable conditions for the formation of Ag dendrites, causing leakage and eventually short circuit.

Equipment and throughput challenges [20]: Pressure-assisted sintering requires special production equipment with the capability to apply uniform pressure without breaking the dies (preferably over multiple dies in one go). While pressureless sintering does not require any new capital investment, however, the properties of pressureless sintered joints are inferior as compared to pressure-assisted sintered joints. For applications where WBG devices are to be employed, pressureless sintered joints might not be suitable. Today we see material suppliers working very closely with both customers and equipment makers to make the transition process for the users smooth and efficient. However, high initial capital investment for the purchase and installation of such specialized equipment is a big hindrance to the mass adoption of pressure-assisted silver sintering technology by the power electronics industry. Application of pressure, especially if the pressure is applied one die at a time also reduces throughput greatly as compared to batch processes such as mass reflow. Therefore, the users must see enough value in pressure-assisted silver sintering technology for them to justify its high initial capital cost and lower throughput.

2.3.7 Recent advances in silver sintering to address its challenges:

Addition of filler particles like SiC to Ag pastes [58]: One of the strategies to increase the high-temperature stability of Ag sintered joints is the addition of high melting point ceramic particles such as SiC or BN to Ag pastes. It was reported that the addition of 2% SiC particles by weight did not have a significant effect on the initial shear strength but helped in controlling the bondline thickness and improved the high-temperature stability of the sintered joints. SiC particles, because of their very high modulus, prevented the coarsening of porous Ag grains, which reduced the risk of void formation. After storage at 250°C for 500h, the shear strength of joints with added SiC particles was similar to the

original value (~20MPa). For joints without the addition of SiC, the degradation in shear strength was obvious (from 27MPa to 7MPa). This was attributed to excessive Ag grain growth and the related micro-voids in the joints as can be seen in Figure 2.11.

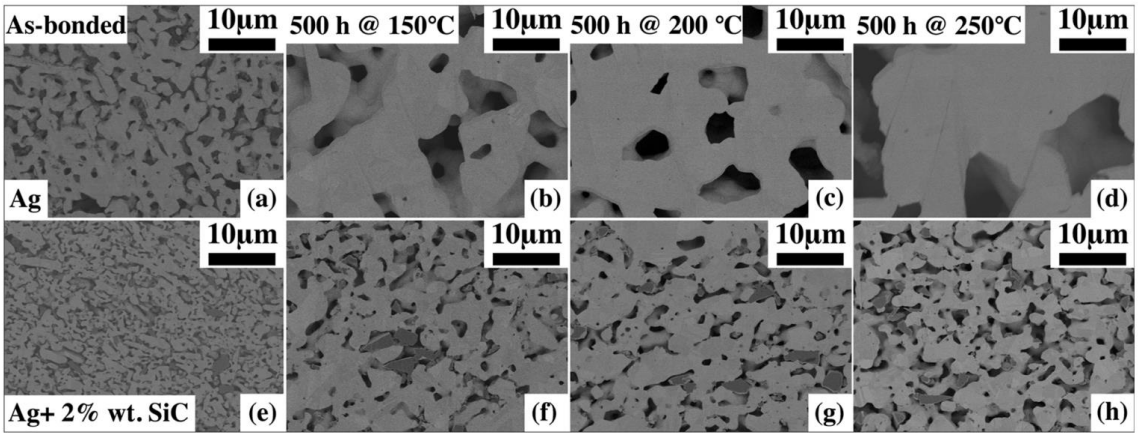

Figure 2.11 Evolution of cross-sectional morphology after aging at 150°C, 200°C, and 250°C for 500 h: (a)–(d) joints with no additive; (e)-(h) joints with added SiC; (a) and (e) are the as-bonded state.

Sinterable Ag films [24]: In this approach, pioneered by Alpha materials [], individual dies or complete wafers can be laminated with a sinterable Ag film. Not many details are given about the composition of the film. A tacking agent is deposited onto the substrate and a temporary attachment between the laminated die and substrate is realized. Subsequently, the stack is sintered under temperature and pressure for 30-120sec to form a silver sintered joint as shown in Figure 2.12. This approach has several advantages over traditional paste printing and sintering. Some of them are - reduced organic contents as compared to paste, giving lower shrinkage, warpage, and risks of organics residue entrapment, precise control over bondline thickness, no bleed out and die-tilt, ease in handling of large die sizes and higher throughput.

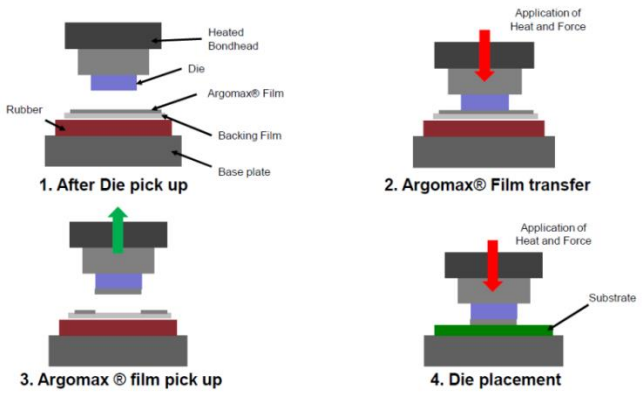

Figure 2.12 Die transfer film process and die placement for Alpha's ARGOMAX die-attach film using die-bonder equipment [59].

Resin-reinforcement of silver-sintered joints [60]: In this approach, developed by Namics Corporation, epoxy resins are also added in the Namic's proprietary nano-Ag pastes based on MO (organo-metallics) technology. The resin cures after the sintering of nano-silver particles and prevents the sintered Ag microstructure from further evolution at elevated temperatures. Resin-reinforced sintered joints showed better reliability after thermal cycling, as shown in Figure 2.13. However, the addition of epoxy resins limits the operating temperature of the joints to 200°C.

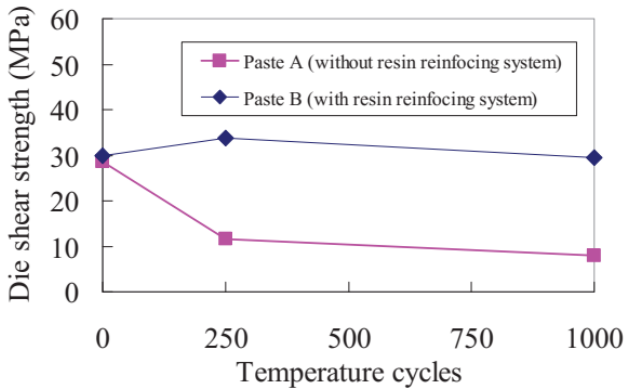

Figure 2.13 Die-shear strength variation with thermal cycling for simple silver-sintered joints and resin-reinforced silver-sintered joints [60].

2.3.8 Alternatives to sintered Ag joints

In summary, sintered silver represents the current state of the art die-attach technology capable of producing joints with excellent electrical and thermal properties. The technology is maturing rapidly and is expected to be employed in WBG power modules in high volume. Although sintered Ag joints have excellent properties, Ag has some inherent limitations: i) very high cost, ii) Ag is prone to ECM under applied electric field, a critical issue especially in high power modules. This has motivated the researchers to also consider the sintering of Cu-particles.

2.4 Sintered-Cu die-attach joints

Sintering of Cu pastes to form all-Cu die-attach joints is a relatively new area, which is expected to gain momentum in the coming years. This approach benefits from the following main advantages: i) much lower cost of Cu compared to Ag pastes; ii) no requirement of noble metal surface finish, which are generally required for Ag sintering. The bonding can be carried out on bare-Cu surfaces; iii) very high electrical and thermal conductivities, almost matching that of Ag; iv) more resistant to electrochemical migration as compared to Ag.

However, the sintering of Cu particles is considered more challenging as compared to the sintering of Ag particles. Because of the higher melting point of Cu (1083°C) as compared to Ag (962°C), a higher sintering temperature than silver sintering is also expected. Further, because the Cu particles have a very high affinity towards oxygen, especially at higher temperatures, oxidation becomes a huge challenge. Moreover,

oxidation of sintered Cu-Cu joints post assembly and during field operation can lower the joint properties significantly.

The research in the area of sinterable Cu pastes has mainly looked at different strategies for the prevention of oxidation and characterizing the impact of sintering parameters and Cu particle size on joint shear strengths [61]. First studies on sintered Cu die-attach used Cu particles which were not mixed with any organic surfactants and therefore, immediate oxidation of Cu particles was observed after getting exposed to the ambient atmosphere [33, 62]. The bonding of Cu nanoparticles, 30-50nm, was carried out at 350-400°C under 5% H_2 – 95% N_2 environment [62]. A pressure of 5-15MPa was applied and bonding time was varied between 15-20mins. The highest shear strengths were obtained for the samples bonded at 400°C and 10MPa pressure. Successful bonding using micron-scale Cu particles with size < 5µm at 350°C was also demonstrated [33]. The shear strength of the joints varied between 17-23 MPa. The bonding was carried out in the air for 2mins, however, the Cu paste was treated with H_2 at 350°C before bonding to remove the surface oxides. The discussed results did not employ use if any organic binders or additives to prevent oxidation or provide a reducing atmosphere during the bonding process. As such, bonding temperatures higher than 300°C were required to form successful Cu-Cu joints.

More recent studies have looked at novel paste formulations which can provide for self-reduction of existing Cu oxides during assembly as well as protect the formation of further oxides on the surface of Cu particles. It was reported that the addition of ascorbic acid (AA) to the Cu pastes provided both self-reduction and self-protection characteristics to the Cu paste against surface oxides [63]. AA successfully reduced the native oxides present on the Cu particles after their preparation. Moreover, during the sintering process,

the decomposition of AA produced a reducing atmosphere which prevented any further growth of oxides during the sintering process. Sintered joints with a shear strength of 24.8MPa were obtained after sintering at 300°C and 0.4MPa applied pressure for 30mins in the N_2 atmosphere.

The latest studies have focused on leveraging the interaction of Cu oxides with formic acid to develop low-temperature assembly processes [61, 64]. Cu particles mixed in ethylene glycol were bonded to Cu substrates without any surface oxide pre-cleaning treatments for both the Cu nanoparticles and the Cu substrates. Assembly was carried out at 250°C under 5MPa for 30min in Ar gas atmosphere with Pt-catalyzed formic acid vapors [64]. Pt-catalyzed formic acid vapors were found to be highly effective in reducing the oxides at 250°C and joint strength of 20.6MPa was observed.

2.5 Summary of sintered die-attach interconnections

Sintering of Ag pastes can enable all-metal die-attach joints with excellent electrical and thermal performances. Owing to continuous research and investments, rapid advancements have been made in the sintered silver technology which is highlighted in the increasing industry adoption of sintered Ag die-attach joints. Pressureless Ag sintering pastes capable of providing moderate performance at bonding temperatures less than 250°C have been successfully developed. However, paste based sintering has a few drawbacks, particularly the presence of organics, which brings complexities in the assembly process and degrades the performance and reliability of the joints. The residual organics are can detrimentally impact the sintering of Cu pastes, lead to the formation of voids the bonding interface, and cause corrosion-related challenges during operations. The

organic additives can make up to 90% volume of the pastes, and therefore, the sintering of such pastes is accompanied by large shrinkage due to the decomposition of the organic additives. Large shrinkages during assembly can lead to process complexities such as paste bleed out, warpage of the die, and non-uniform bondline thickness. At large-die sizes, back-pressure due to the outgassing of the volatiles is an added concern.

Sintering of Cu pastes is relatively a young technology as compared to the sintering of Ag pastes. In addition to the challenges intrinsic to Cu, like oxidation and high stiffness, Cu pastes face the same challenges as faced by the Ag pastes. Additionally, the shear strengths of sintered Cu joints are lower as compared to sintered Ag joints. The assembly process requires pressure and bonding temperatures are generally higher than 250°C.

As such, any die-attach solution beyond the current Cu nanoscale pastes based approach must - i) give all-Cu joints by low-temperature processing (preferably <250°C) and low-pressure assembly, ii) be devoid of any organic additives, iii) provide joint shear strengths >25MPa, iv) provide a high degree of tailorability in modifying the joint properties, and v) be low-cost and manufacturing friendly.

CHAPTER 3. NANOPOROUS COPPER PROPOSED AS NEXT GENERATION DIE-ATTACH INTERCONNECTION MATERIAL

The previous chapter extensively covered the technical limitations of state-of-the-art die-attach technologies, with a focus on silver sintering. As has been mentioned before, to define the key attributes of the next-generation die-attach technology, two key assumptions have been made based on extensive literature survey and discussions with the industry:

i) All-metal sintered joints (Ag/Au/Cu), without any intermetallic formation, provide the best of both electrical and thermal performances. Therefore, the new material system should be a low-temperature sinterable system which can provide bulk-metal like properties after sintering.

ii) Copper provides a significantly lower cost alternative to silver with almost similar electrical and thermal conductivities. Therefore, copper should be the natural choice of material.

In this chapter, the sintering of nanoporous copper is proposed as the next-generation die-attach technology to realize all-Cu interconnections with bulk-Cu like electrical and thermal performances, and stability at operating temperatures >250°C.

This chapter introduces nanoporous metals and their characteristics, physical properties, and fabrication techniques. The motivation for proposing nanoporous copper as the next-generation novel interconnection material over nano-Ag/Cu paste sintering is detailed and the unique approach is explained.

3.1 Introduction to nanoporous metals

Nanoporous metals (NP-metals) are unique nanostructured material with nanosized porosity, nanoscale structural features, and very high specific surface area [65]. For simple visualization, they can be construed as porous metal sponges made of nanoscale structural features. A simple model used to describe cellular materials [66], as shown in Figure 3.1, can be used to model NP-metals. The model consists of a cubic framework made of connector elements joining two corners together while connecting to the next repeating lattice set. These corners are called the nodes while, the smallest features, i.e. the connector elements, joining the two nodes are called ligaments. Structural features such as the number of node-ligament junctions, the ligament length/width (t/l) aspect ratio, node/junction dimensions, and overall pore size define the macroscopic morphology as well as mechanical, thermal and electrical properties of these NP-metals.

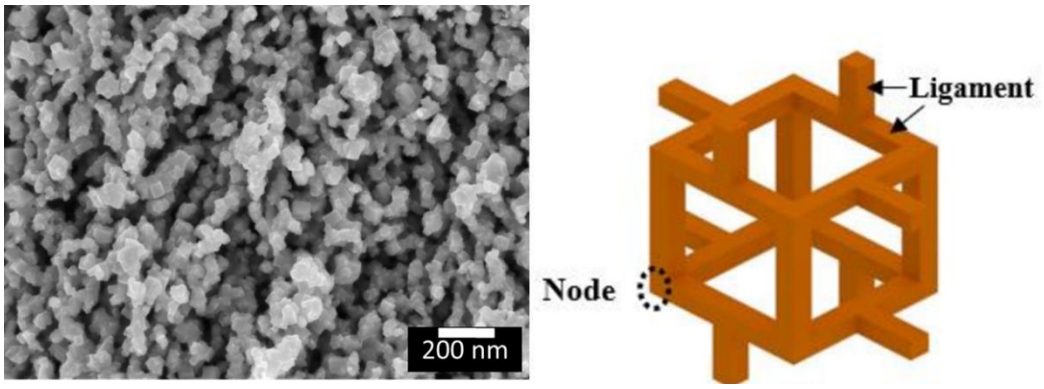

Figure 3.1 SEM images of NP-Cu (left); working model of a cellular solid with defined nodes and ligaments (right).

3.1.1 Properties of NP-metals

3.1.1.1 Mechanical properties

NP-metals exhibit moderate specific modulus and higher specific yield strength (ratio of modulus and relative density) compared to the bulk values. For instance, NP-Cu can have Young's modulus ranging between 10-45GPa, as compared to the bulk-Cu value of 120GPa, depending on the nanoporous structure [67]. Two possible reasons can be attributed to this change in the mechanical properties as compared to the bulk properties - First is the nanoscale effect due to the nanostructuring of the ligaments. It has been widely reported that below a threshold feature size (5-20 nm), dislocation generation, thus dislocation mediated plasticity, becomes very restricted resulting in drastic improvements in mechanical properties at the nanoscale. Second is the geometric effect, i.e. the specific morphology of NP-metals, with mass aggregation at junctions and very small aspect ratio of ligaments result in the higher modulus [66, 68, 69].

3.1.1.2 Electrical and thermal properties

NP-metals show lower thermal and electrical conductivities than the bulk. On a macroscopic scale, the thermal and electrical conductivities decrease with an increase in the pore fraction. Additionally, the conductivity values are dependent on the ligament thickness, pore sizes, and defects induced in the ligaments during fabrication. Thicker ligaments increase the conductivity, but pores and defects act as scattering centers and thus are detrimental. A comparison of the thermal conductivity and electrical resistivity between the NP-systems and bulk systems is given in Table 3.1[70-72]. NP-metals, like other porous solids, have a magnitude of order less thermal conductivity than the bulk. Upon

densification, however, both their electrical and thermal conductivities are expected to increase to values closer to that of the bulk.

Table 3.1 Comparison of thermal conductivity (κ) and electrical resistivity (ρ) between NP-metals and bulk system (at 300K).

Material system	Bulk - κ (W/m.K)	Nanofoam - κ (W/m.K)	Bulk -ρ (μΩ.cm)	Nanofoam - ρ (μΩ.cm)
Au	320	8 *(5)*	2.2	70 *(7)*
Cu	385	13.48 *(6)*	1.68	54.5 *(6)* *42.5 (8)*

3.1.2 Fabrication of NP-metals

Chemical dealloying is the most widely used method to synthesize NP-metals. The method of alloying and dealloying starts with the formation of a binary or ternary precursor alloy system followed by selective chemical etching of the undesirable element(s). The initial alloy can be synthesized in sheets or ribbons or build on wafers or substrates using different techniques: 1) arc or furnace melting 2) electrodeposition 3) sputtering [73-77]. Under the action of an etchant, the active elements of the alloy get dissolved while the relatively nobler element(s) self-assemble(s) to form a nanoporous structure with interconnected ligaments and pores, as shown in Figure 3.2. This method is the most common way for large-scale manufacturing of nanoporous metals.

For the precursor alloy systems to form porous structures upon dealloying, a few guidelines can be established [65]:

- A significant electrochemical potential difference between the nobler and less noble components.
- The alloy is usually rich in the less noble component.
- Homogeneous single-phase alloys with no phase separation prior to dissolution are expected to yield a more uniform nanoporous structure. Multiple phases can show different etching rates for the same component, which can result in non-uniform porosity.
- The diffusion of more noble atoms at the alloy-to-electrolyte interface must be sufficiently fast.

Dealloying processes can be classified as either free dealloying in which the alloy is simply immersed in the etchant or electrochemical dealloying where an additional external potential is also applied [73, 78, 79]. The dealloying rate is slower and cannot be easily controlled in free dealloying as compared to electrochemical dealloying and therefore, it takes a longer time for fabrication of NP-metals, usually running into a few hours. Longer dealloying duration also results in the coarsening of ligaments and non-uniform morphology.

Alternatively, electrochemical dealloying can reduce the dealloying time by an order of magnitude, resulting in finer ligament and pore sizes as well as provide uniform control over the evolution of the nanoporous morphology. The physical properties of NP-metals change with variations in ligament thickness, relative density, and morphology. These design features can be tuned by changing the dealloying parameters like time,

etchant chemistry, or the initial alloy composition, to optimize the physical properties for different applications. Electrochemical dealloying gives an additional knob, i.e. the applied potential, for controlling the nanostructure, especially the size of pores and their geometrical distribution [68, 69].

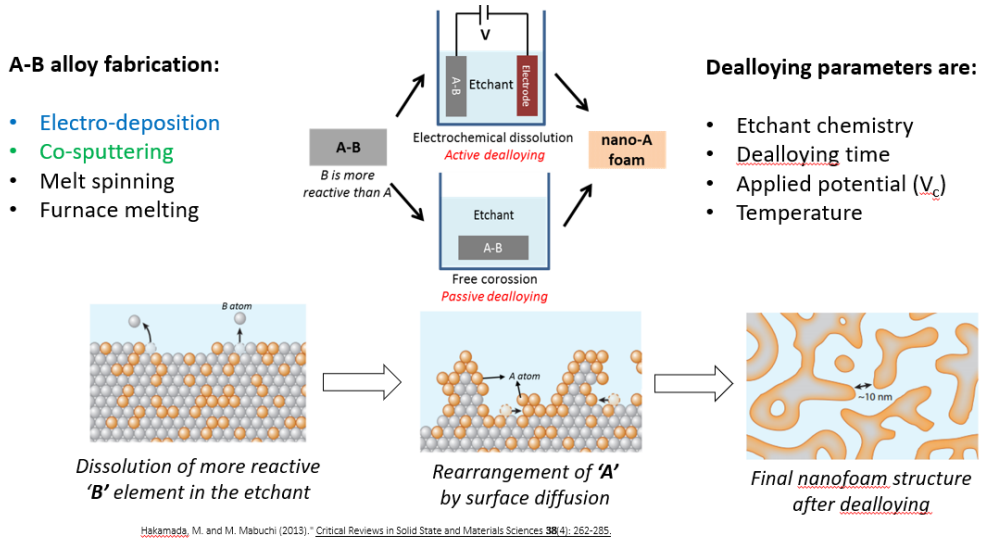

Figure 3.2 Schematic showing the different routes to fabricate the initial alloy, the key dealloying parameters, and the mechanism of chemical dealloying [73].

3.1.2.1 Effect of precursor alloy composition

The structure of NP-metals is dependent on the composition, phases as well as microstructure of the initial parent precursor alloy. First and foremost, there should be a significant electrochemical potential difference between the nobler and less noble components in the precursor alloys. Additionally, the concentration of the more noble constituent should be below the parting limit. The parting limit is the percentage of reactive element below which de-alloying stops and no re-assembly of the noble constituent is possible [80]. Different alloy systems exhibit varying parting limits. For example, for Au-

Ag alloys, the concentration of Au should be 20<Au<45 at% to ensure complete dealloying and formation of NP-Au [80]. For Cu-Zn, alloys with Zn>20 at% for successful dealloying [81]. The composition also impacts the morphology of the dealloyed NP-metals. For example, it was observed that on dealloying of Ag-Al alloys, an increase in Ag from 15 at.% to 50 at.% increased the ligament sizes of NP-Ag from 94+5nm to 448+5nm [82]. Similarly, the composition can also significantly impact the size of the pores. In general, the alloys with lesser noble constituents are expected to exhibit larger pores or open channels upon dealloying.

The NP-metal morphology is also significantly impacted by the phases present in the parent alloy. Single-phase solid solutions or intermetallics are likely to give uniform bicontinuous NP-morphology. For multi-phase alloys, the dealloyed NP-structure will depend on the interaction of different phases with the etchant. Assuming all the present phases can be dealloyed, the dealloyed NP-metal will potentially have a combination of different ligament/pore size distributions. For example, Au-Al alloys containing two phases AlAu and Al_2Au on dealloying exhibited two different ligament/pore size distributions [83]. In case, if one of the phases can be completely etched, it can lead to the formation of big channels and the dealloyed NP-metal will exhibit a bimodal channel/pore morphology where the size of the channels can be a magnitude greater in size than the pores or the ligaments [84]. Moreover, it has been observed that the dealloyed NP-structure follows the microstructure of the parent alloys [78].

3.1.2.2 Effect of dealloying time

Dealloying time is an important parameter for the fabrication of completely dealloyed NP-metal films with a low concentration of remnant more reactive components. Dealloying front progresses from the top surface, and therefore, thicker alloys need more dealloying time as compared to thin alloy films. For example, on an increase in the thickness of Au-Ag alloy from 100nm to 10h, the dealloying time in HNO_3 increased from 3min to 10h [78]. It has been also observed that in general, the NP-metal morphology coarsens with an increase in dealloying time. This can be attributed to the diffusion of noble metal atoms along the NP-metal surface/etchant solution interface to form coarser ligaments with reduced surface energy. The extent of coarsening was found to be dependent on both the concentration of the etchant as well as the interfacial diffusivity of metal atoms [79]. For example, the pore size of NP-Cu increased from ~15nm to ~120nm with an increase in the dealloying time from 0.5h to 32h upon dealloying of Cu-Mn alloy films in HCl [85].

3.1.2.3 Effect of dealloying solution

Dealloying of single-phase solid solutions Mn-Cu alloy films with composition $Mn_{0.7}Cu_{0.3}$ in four different electrolytes gave different NP-Cu ligament morphologies and length scales - ligament diameter of 125 ± 30 nm in pH 1.3 HCl, 80 ± 20 nm in 1M citric acid, 45 ± 11 nm in 0.01M H_2SO_4 + 0.001M $MnSO_4$, and 53 ± 8 nm in 1M $(NH_4)_2SO_4$ + 0.01M $MnSO_4$. The residua Zn and dealloying rate also varied with different electrolytes. Moreover, dealloying in HCl gave smooth and uniform ligaments whereas dealloying in citric acid gave more rugged and non-uniform ligament morphology. The SEM images can

be seen in Figure 3.3 [85]. The large differences in the NP-Cu morphology were attributed to different dealloying rates and surface mobilities of Cu atoms in different electrolytes. Other studies have also reported faster dealloying rates and coarser ligaments after dealloying in HCl as compared to other etchants. NP-Au, Pd, Cu, and Ag dealloyed in HCl had larger ligament sizes than the ones dealloyed in NaOH solutions [79]. It was found that the presence of Cl^- increased the surface diffusivity of the noble atoms, which resulted in a coarser and more uniform structure. The addition of NH_4Cl to HCl increased the dealloying rate of Cu-Zn alloys as well and gave NP-Cu with lower residual Zn and uniform morphology [76].

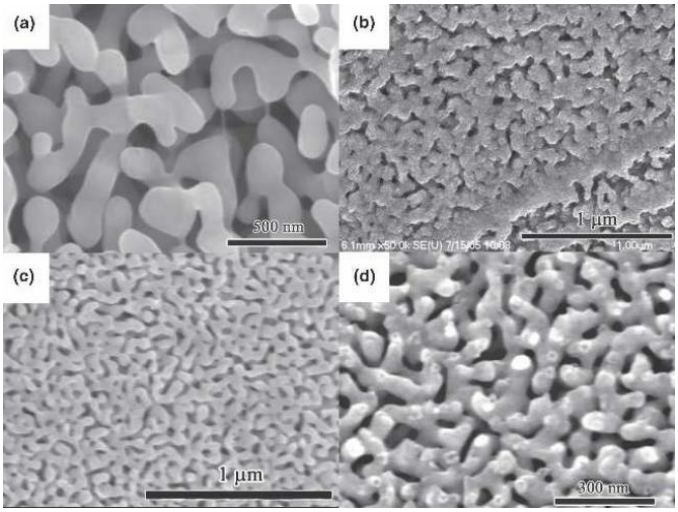

Figure 3.3 Dealloying electrolytes affect both the ligament size and morphology. These SEM micrographs show the structure resulting from dealloying $Mn_{0.7}Cu_{0.3}$ in (a) pH 1.3 HCl, (b) 1 M citric acid, (c) 0.01 M H_2SO_4 + 0.001 M $MnSO_4$, and (d) 1 M $(NH_4)_2SO_4$ + 0.01 M $MnSO_4$.

3.1.2.4 Effect of dealloying potential

The applied potential significantly impacts the dealloying kinetics, and thus the dealloyed NP-structures. The critical potential is defined as the potential which marks the

transition from a passivated alloy surface to the sustained dealloying. The applied potential must be higher than the critical potential. The applied potential is essentially an additional driving force for selective etching, and therefore, as compared to free dealloying can significantly reduce the activation energy. The lower activation energy for etching results in faster dealloying rates, reduction in the dealloying time by an order of magnitude, finer ligament, and pore sizes as well as provide uniform control over the evolution of the nanoporous morphology [78]. For example, in Cu-Mn alloys, potentiostatic dealloying of $Cu_{0.3}Mn_{0.7}$ in 0.01M H_2SO_4 + 0.001M $MnSO_4$ reduced the dealloying time from 6 days to 14h and resulted in a decrease of ligament size from 45 ± 11 nm to 16 ± 4 nm as compared to free dealloying [85].

3.1.3 Challenges with scaling the fabrication NP-metals

Several studies have demonstrated the immense potential of NP-metals in various applications like catalytic sensing, actuators, energy storage, and electrical interconnections. However, the industry penetration of these novel materials stands low. A primary reason for the low penetration is the difficulty in the fabrication of large size NP-metal films or ingots due to the development of cracks. Very often, dealloying is also accompanied by a volume shrinkage. For example, Au-Ag alloys showed a volume shrinkage up to 30% upon electrochemical dealloying. Especially in the case of precursor alloy films onto a substrate, the volume change due to dealloying is constrained in the axial plane []. This results in the build-up of residual tensile stresses, which are compensated by the formation of cracks. Aspect ratio of such deposited alloy also significantly impacts the crack formation on dealloying.

During chemical dealloying, two competitive processes – etching and removal of more reactive element/s and surface diffusion of more noble element play an important role in influencing the cracking behavior. For example, it has been argued that electrochemical dealloying usually has a higher propensity for inducing cracks as compared to free dealloying. The electrochemical dealloying of Au-Ag alloys significantly enhanced the dissolution rate, thereby increasing the stresses due to the faster removal of Ag atoms. Additionally, faster dealloying rate also reduced the effective time for diffusion and rearrangement of Au atoms resulting in reduced stress relief.

Different techniques have been proposed for the formation of crack-free NP-metal films. For the Ag-Au alloy system, it was observed that maximizing the Au in the initial alloy by choosing the composition near the parting limit of Au is highly effective in reducing the shrinkage due to dealloying and thus, the cracking. A high temperature anneal process was also found effective in reducing the crack-area in dealloyed Ag-Au films. It was argued that the thermal treatment of Ag-Au films at 300°C removed the microstructural defects like nanoscale voids which can potentially act as nucleation sites for microscale crack-like voids during dealloying. An increase in temperature of the dealloying etchant also helped in improving the mechanical integrity of the dealloyed films due to higher surface diffusion enabled stress relief at elevated dealloying temperatures. Potentiostatic dealloying with a ramped potential increase as compared to a stepped potential increase also helped in reducing the cracking tendency by slowing down the dissolution rate.

3.2 Sintering of nanoporous-Cu for all-Cu joints

Sintering of nanoporous Cu (NP-Cu) films is proposed as a novel die-attach technology beyond silver sintering because of the following reasons:

- NP-Cu films, because of nanoscale structural features and nanoporosity, are characterized by a very high specific surface area. Like nanoparticles/pastes, they are also expected to be highly reactive because of the high surface energy. Therefore, NP-Cu films are expected to: a) sinter at low-temperatures and low-pressures assembly conditions to yield highly densified bulk like Cu; b) form metallurgical bonds with die/substrate finish at low-temperatures (Note – this is a hypothesis which has to validated by experimental results).

- Unlike nano-scale pastes, nanoporous systems are solid-state metastable systems and do not need organic additives for stabilization, thereby can enable sintered Cu joints without remnant organic residues, a major challenge with nanopastes.

- As fabricated NP-Cu films have very low sub-20GPa modulus [67], which can provide tolerance to surface roughness during assembly and compensate for lack of wettability.

- The nanostructure of the NP-Cu films can be easily tailored, giving versatility in assembly process design.

- The dealloying process is compatible with the industry bill of materials. Moreover, large-area sheets of NP-Cu can be fabricated, and subsequently diced into desired

preform sizes and used as inserts for die-attach bonding, enabling scalability and a modular supply chain.

- NP-Cu films can be directly bonded on bare Cu metallization and do not need expensive passivation and surface treatments to deal with oxidation, making them further cost-effective over sintered Ag and Cu pastes.

The unique approach with all its advantages is summarized in the schematic of Figure 3.4.

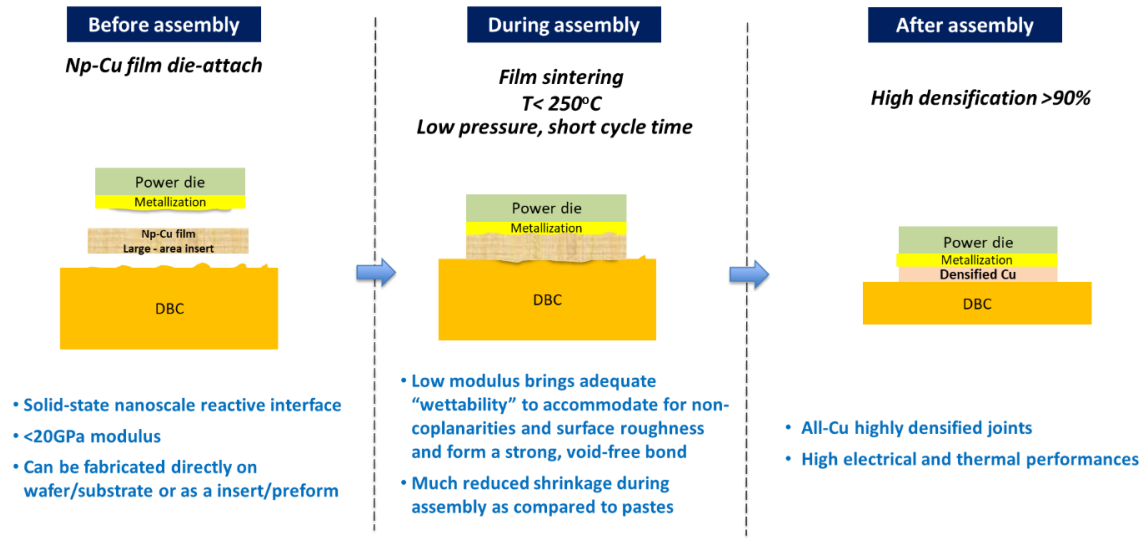

Figure 3.4 Schematic illustrating the implementation of np-Cu as a novel die-attach material.

3.3 Recent works exploring nanoporous metals as die-attach materials

Recently, few research groups have also demonstrated the feasibility of all-metal interconnections by sintering of nanoporous Ag, Au, or Cu, proving further weight to the approach.

Nanoporous-Ag sintering [21]: It was demonstrated that nanoporous-Ag can sinter and densify at low-temperatures (<350°C). Two Cu surfaces with Au finish were joined together using Ag-nanoporous film inserts as the bonding layer. Bonding was performed at 200-400°C for 30min at 20MPa pressure. The shear strength and joint microstructure variations with bonding temperatures are shown in Figure 3.5 and Figure 3.6.

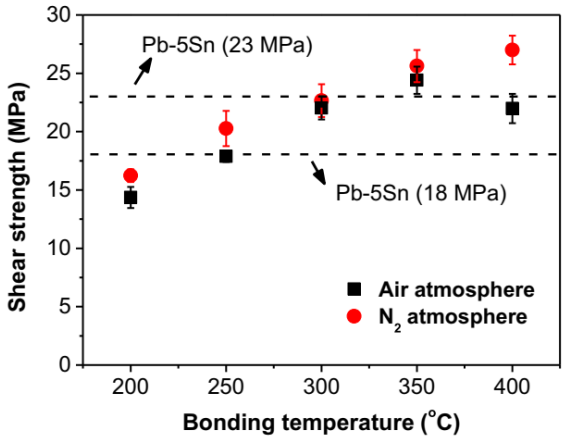

Figure 3.5 Shear strength of Ag nanoporous bonding joint for various bonding temperatures in air and N_2.

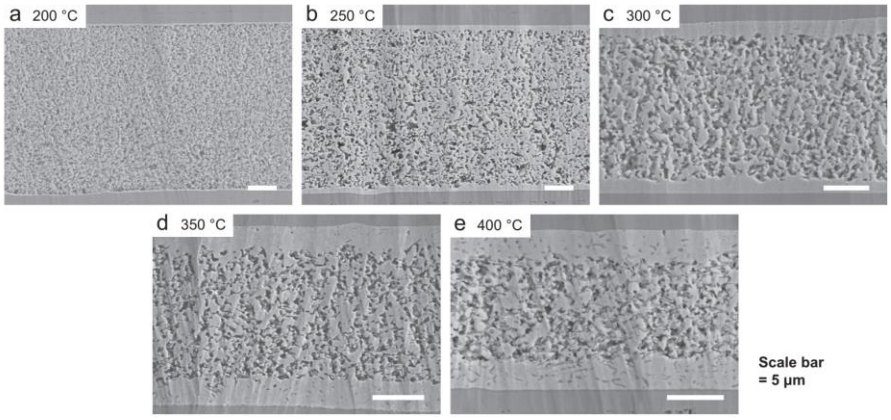

Figure 3.6 Cross-sectional images of bonded joints at different bonding temperatures.

This joining technique has unique advantages - such as an absence of flux and solvents; a simple method for the bondline thickness control as compared to the nanoparticle sintering; and the ability to tailor the joint microstructure with variation in bonding parameters.

Nanoporous-Cu sintering [86, 87]: $Cu_{40}Al_{60}$ alloy ingots were fabricated by the melting of Cu and Al under Ar atmosphere. Smaller sheets were sectioned from the alloy block and dealloyed in HCl to form NP-Cu sheets. Cu/NP-Cu/Cu sandwiched samples were assembled at 260°C for 5-30min under 10MPa pressure. The joint cross-section is shown in Figure 3.7. Maximum shear strength of 22.1MPa was achieved.

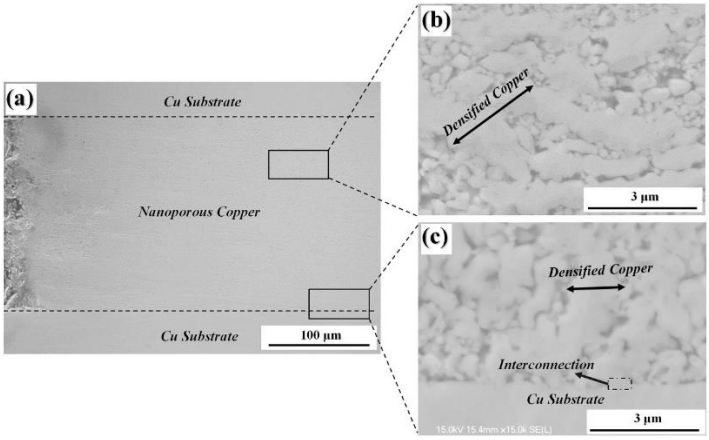

Figure 3.7 SEM images of a cross-section of NP-Cu joining: (a) whole image; (b) and (c) local magnification images.

Large-scale and repeatable fabrication of nanoporous metals is yet to be comprehensively addressed. Sintering of nanoporous metals is a very new research area and more research is required to understand their sintering mechanisms. Addressing the two challenges would form the core of this research.

CHAPTER 4. FABRICATION OF NANOPOROUS COPPER DIE-ATTACH FILMS

In the previous chapter, the motivation for the downselection of NP-Cu as the next-generation die-attach material was outlined. This chapter summarizes the work done and understanding gained towards the fabrication of NP-Cu films. To be considered as the material of choice for die-attach interconnections, first and foremost the fabrication process must be industry-friendly. It was also mentioned that scaling the size of NP-metal films remains a big challenge. Therefore, fabrication techniques are needed which can provide crack-free NP-Cu films with excellent uniformity of nanoporous structure both repeatedly and on a large-scale.

Before starting on experimental design for the fabrication of NP-Cu films, an extensive literature survey was done to identify the suitable precursor alloy and its synthesis route. The summary of the review of the precursor alloy systems, their synthesis, and the morphology of NP-Cu films dealloyed from these precursors have been presented in Table 4.1.

Based on the literature survey, it was decided to pursue the fabrication of NP-Cu films by chemical dealloying of amorphous Cu-Zr based melt-spun ribbons. The dealloyed NP-structure is significantly impacted by the microstructure of the parent precursor alloys. Defects like phase segregations and intermetallics impact the dealloyed structure and more often they are responsible for inhomogeneities in the dealloyed NP-structures [72, 78, 83, 85]. Therefore amorphous alloys are expected to be an ideal candidate for dealloying as

they can be considered a chemically homogeneous single-phase that is absent of grain boundaries, large-scaled phase segregations, and intermetallics [88-91]. Several reports have confirmed the formation of highly uniform NP-structures from different amorphous alloy systems [88-91]. Moreover, the choice was also influenced by the easy availability of moderately sized Cu-Zn-Al melt-spun ribbons and the opportunity it presented for the fabrication of standalone NP-Cu ribbons which could be used as inserts for die-attachment.

Table 4.1 Review of different alloy systems that have been demonstrated to yield NP-Cu on dealloying.

System	Fabrication Route	Electronegativity difference	Etchant	Dealloying parameters	Foam Morphology (Ligament Size*)
Cu-Mg	• Melt spinning	0.34/-2.37	5% HCl	Passive (0.5hr)	150+35nm
Cu-Al	• Melt Spinning • **Co-sputtering**	0.34/-1.66	HCl+ NaOH	Passive (2 - 4hr)	100-300nm
Cu-Zr	• Melt spinning • **Co-sputtering**	0.34/-1.45	HCl	Active (10 min)	Pore Size: 500nm
Cu-Mn	• Arc melting • **Electrochemical deposition**	0.34/-1.18V	HCl/H_2SO_4	• Passive; 2-10 days • Active 14 hrs	• 45-120nm • 16+4nm
Mg-Cu-Y	• Melt spinning		H_2SO_4	Passive (1.5 hr)	3-8nm Pore Size: 30-60nm
Cu-Zn	• Furnace melting • **Electrochemical deposition** • **Co-sputtering**	0.34/-0.76V	• $HCl+NH_4Cl$ • NaOH & HCl	• Passive • Passive (15 hr)	• 120+30nm • 100nm -500nm
Cu-Si	• **Co-sputtering**		HF	Active (3 - 5 min)	30-80 nm

4.1 Fabrication of NP-Cu films from amorphous alloy ribbons

4.1.1 Dealloying and characterization of as-received melt-spun ribbon

A melt-spun ribbon with a nominal composition of $Cu_{40}Zr_{45}Al_{15}$ by atomic percentage was procured from Nanostructured & Amorphous Materials, Inc., Houston, Texas. The procured ribbon was typically ~55 µm in thickness and ~3 mm in width. The

ribbon composition was confirmed using X-ray diffraction (Pan Analytical Alpha Pro MRD, Cu-Kα) and energy dispersive X-ray spectrometer (EDX), by Oxford instruments, that is attached to the SEM.

Figure 4.1(a) shows the XRD spectrum of the as-received ribbon with a broad diffraction halo without any distinguishable crystalline peaks, confirming the amorphous nature of the melt-spun ribbon. The EDX measurements shown in Figure 4.1(b) confirmed that the stoichiometry of the as-spun ribbon matched the manufacturer specifications.

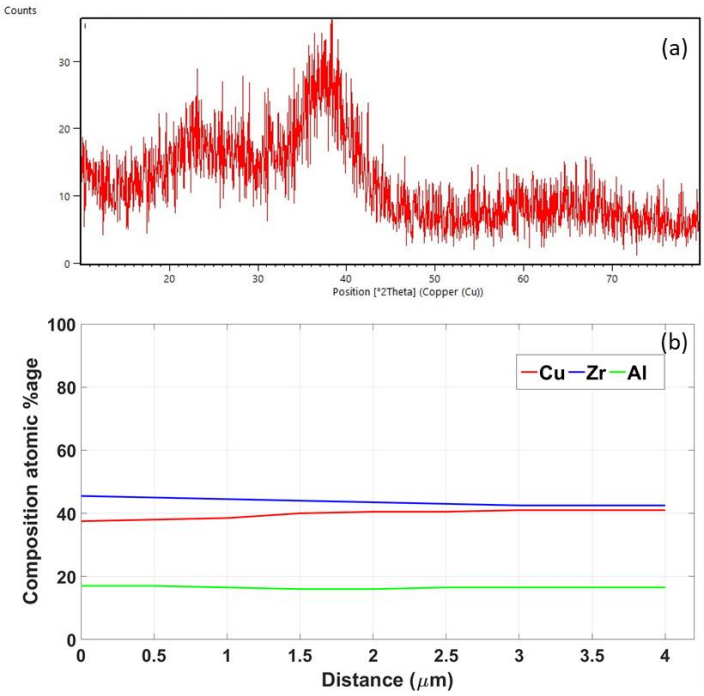

Figure 4.1 (a) XRD and (b) EDX (line-scan) on the as-received (Set A) ribbon.

To prepare samples for dealloying, ~10 mm long pieces were cut the ribbon. The cut samples were dealloyed in 0.03M HF aqueous solution under free corrosion conditions. The dealloying time was varied from 24 to 72h. The dealloyed NP-Cu samples were rinsed in deionized water and dried in N_2. The microstructures of the dealloyed samples were

characterized by Scanning Electron Microscopy (SEM, Zeiss FE 60). Dealloyed ribbon samples were sectioned and the cleaved side was imaged to obtain cross-sectional SEM micrographs. EDX was performed after dealloying and it confirmed the complete etching Zr and Al atoms.

Figure 4.2(a-b) shows the optical image of the sample before and after dealloying respectively. A color change was observed from light gray to dark brown after dealloying suggesting the formation of NP-Cu and the complete etching of the Zr and Al atoms. Figure 4.2(c-d) shows the SEM image of the cross-section of the dealloyed NP-Cu ribbons. The SEM image confirmed both the complete dealloying of the ribbon through-thickness and the formation of uniform nanoscale ligaments with size in the range of 25-60nm. However, a few not so promising results were also obtained. First, the dealloyed ribbon developed in-plane cracks as shown in Figure 4.2c. Secondly, upon dealloying, the dealloyed samples developed a net curvature which was higher than the curvature of the undealloyed samples. Both these results detrimentally impact the ability to use such NP-Cu samples for die-attachment. Cracks within the NP-Cu are the weak points and can potentially act as failure-initiation sites in the sintered NP-Cu die-attach joints. Warpage of NP-Cu films detrimentally impacts its ability to make good metallurgical contact with bonding interfaces which can lead to inferior sintered joints. Due to the high significance of both the results, experiments were designed to better understand the crack generation and curvature evolution during dealloying.

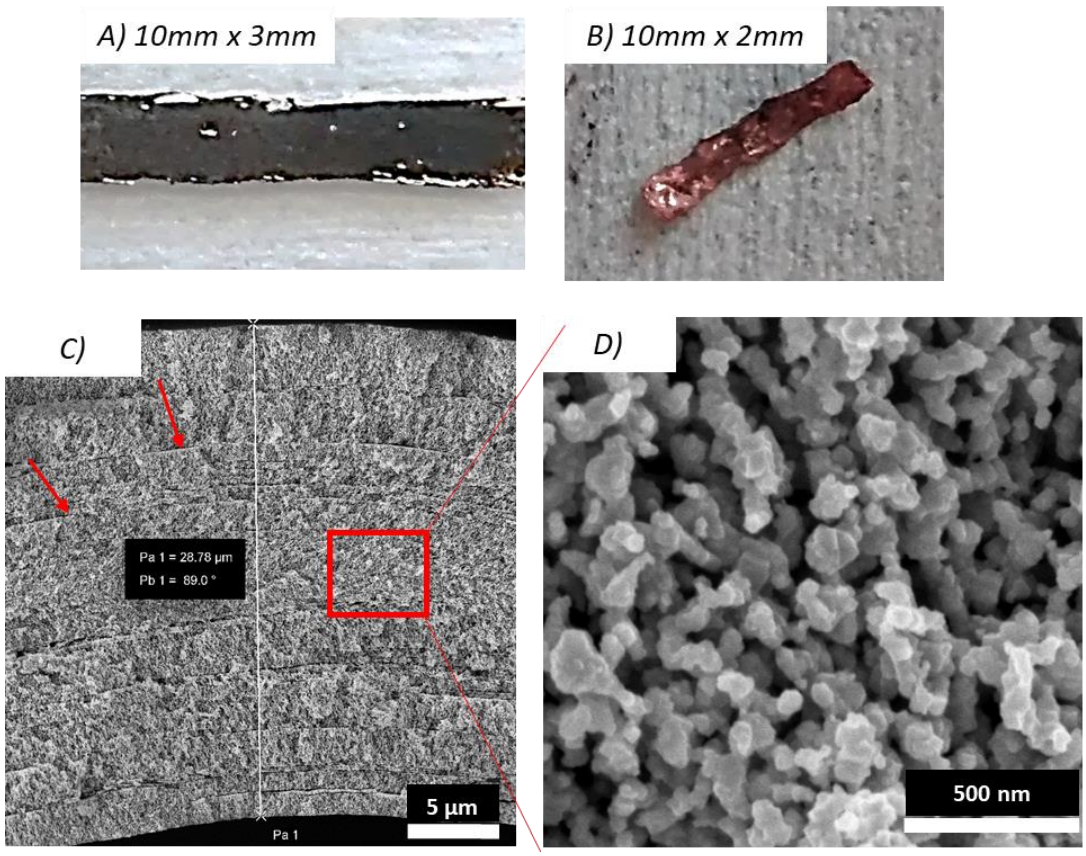

Figure 4.2. (a-b) Optical images of the 10mm cut amorphous sample before and after dealloying respectively. (c) SEM image of the cross-section of a fully dealloyed NP-Cu sample. (d) Magnified SEM image showing the nanostructure in the dealloyed NP-Cu sample.

4.1.2 Design of experiments to understand the crack generation and evolution of curvature during dealloying

4.1.2.1 Bending of as-received ribbon

The melt-spun ribbon was received as a coil of ~1cm radius. It has been widely reported that the melt-spun ribbon's surface in contact with the spinning wheel has better surface smoothness as compared to the surface in contact with the air [92]. In this paper, the two surfaces are referred to as smooth (wheel-side) and rough (air-side) faces respectively.

On releasing the as-received coil, the ribbon maintained a residual curvature such that the rough surface was the concave (inner) side (Set A seen in Figure 4.3a). As part of the experimental design, a ~15 cm section of the ribbon was cut, coiled in the opposite direction, and was kept in the coiled state for one week. After the coiled sample was released, an opposite residual curvature was obtained, such that the smooth surface was now on the inner side. This sample is referred to as Set B.

4.1.2.2 Chemical dealloying and characterization of NP-Cu

To prepare samples for dealloying, ~10 mm long pieces were cut from Set A and Set B sections. The cut samples were dealloyed in 0.03M HF aqueous solution under free corrosion conditions. The dealloying time was varied from 1 to 10h. The dealloyed NP-Cu samples were rinsed in deionized water and dried in N_2 prior to further characterization. A total of ~30 samples were dealloyed. After dealloying, optical images of the samples were used to measure the developed curvature. To determine the curvature of the dealloyed samples, the images were processed in software package ImageJ [34]. Dealloyed ribbon samples were sectioned and the cleaved side was imaged to obtain cross-sectional SEM micrographs. The junction size, relative density as well as the thickness of the dealloyed NP-Cu were measured from the cross-sectional SEM micrographs. To calculate the average junction size, measurements were done over 25 random junctions using ImageJ.

4.1.2.3 Evolution in ribbon curvature when the concave surface is either rough or smooth

10 mm long samples were sectioned and dealloyed by free corrosion. Figure 4.3(a) shows the as-received ribbons (Set A) coiled so that their rough surface is the concave

(inner) ribbon side. For Set B, the rough ribbon surface was changed to the convex side (outer side), as seen in Figure 4.3(b)-(e) optical images and illustrated in Figure 4.3(a) schematic. Figure 4.3(f) shows optical images of the 10 mm long Set A samples dealloyed for different times. After dealloying the curvature of the samples changes with the 5h sample having the most dramatic change.

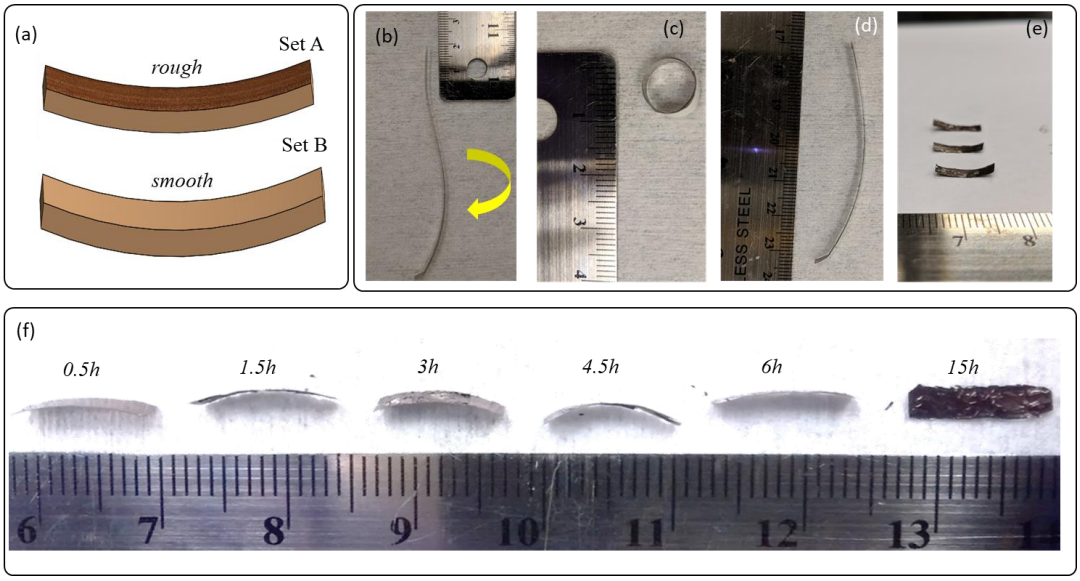

Figure 4.3 (a) Schematic of Set A and Set B ribbons. Set A is the as-received ribbon coiled by the manufacturer so that the inner side (concave) is the rough surface. Set B corresponds to a ribbon segment that was purposefully coiled so that its concave side is the smooth surface. (b-c) Set B ribbon coiling in a different orientation, (d) released after a week, (e) 10 mm samples cut from the released ribbon. (f) Optical images showing the 10 mm samples after free corrosion at different dealloying times. Note that the image contrast has been altered from the original image.

Figure 4.4 shows the evolution of curvature with dealloying time for both sets A and B. For set A samples, the initial curvature of the as-received ribbon after uncoiling was measured to be $0.012mm^{-1}$. After 2.5h of dealloying, the sample developed a curvature of $0.07mm^{-1}$, which reached a peak value of $0.16mm^{-1}$ after 5h. Further dealloying led to a gradual decrease in the curvature of the samples. It resduced to $0.12mm^{-1}$ after 7.5h and

further reduced to 0.08mm^{-1} after 10h of dealloying. A similar trend was observed in Set B samples to the extent that the curvature first increased and then subsequently decreased with dealloying time. Specifically, the curvature evolution of Set B dealloyed samples with dealloying time is shown in Figure 4.4. After 1h, the sample developed a curvature of 0.09mm^{-1}, which decreased to 0.05mm^{-1} after 3h of dealloying. Further dealloying led to a slight increase in the curvature of the samples to 0.06mm^{-1} after 6h.

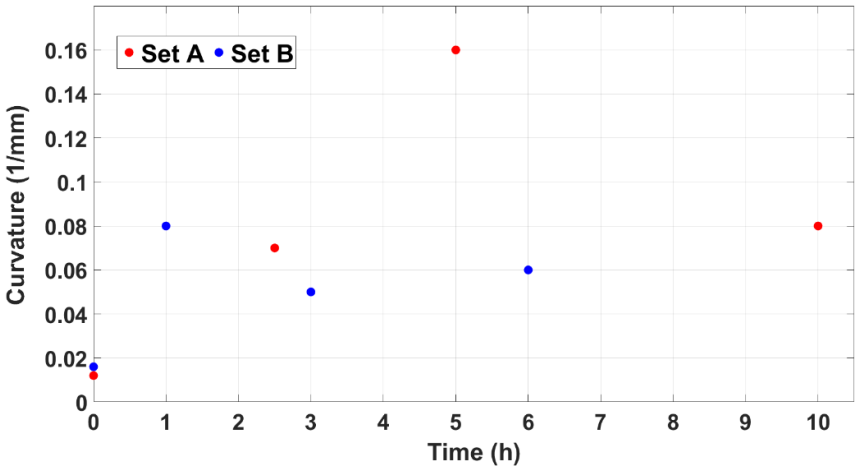

Figure 4.4 The curvature of 10 mm long ribbon segments as a function of dealloying time for Set A and Set B.

4.1.3 NP-Cu thickness with dealloying time

Figure 4.5 shows cross-sectional SEM images of the ribbon as received (Figure 4.5(a)) and after dealloying at different times (Figure 4.5(b)-(c)). The free surface reacted with the electrolyte to form NP-Cu with the dealloying front progressing through the ribbon thickness forming NP-Cu in its wake. Figure 4.5(d) and (e) show the NP-Cu ligaments near the free surface after the ribbon is dealloyed for different times. While both ribbon sides formed NP-Cu with the same relative density and morphology the junction size gradually coarsened with dealloying time. Junctions changed from ~55nm for the 2.5h dealloyed

sample to ~65nm for the 10h dealloyed sample. The relative densities were also estimated by using image processing techniques on the SEM images. The relative densities did not show a large variation with dealloying time and were found to be 57±3%.

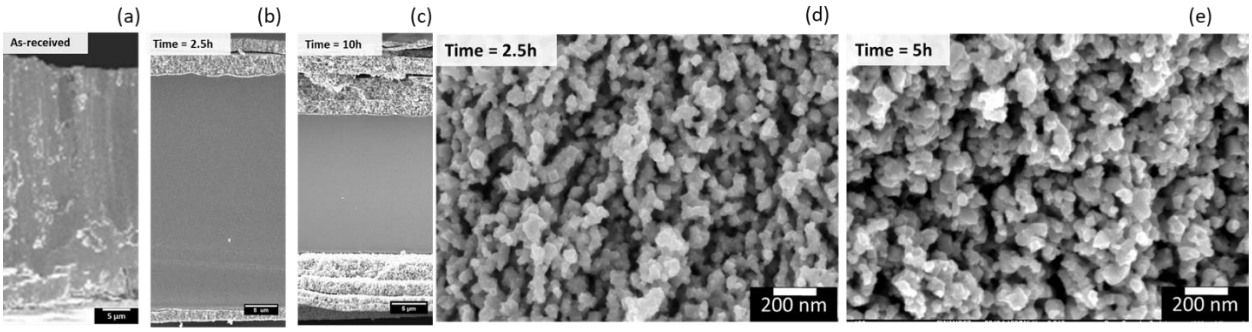

Figure 4.5 Scanning Electron Microscope images of a 90° cross-sectioned view through the thickness of the (a) as received amorphous Set A ribbon. Ribbon cross-section view after (b) 2.5 hours and (c) 10 hours of dealloying time. After dealloying, NP Cu has formed on the top and bottom sides of the ribbon whose morphology is shown in higher magnification SEM images after (d) 2.5 and (e) 5 hours of dealloying.

Figure 4.6 shows the increase in the dealloyed NP Cu thickness with an increase in the dealloying time. The smooth (outer or convex side) and rough (inner or concave side) surfaces for Set A samples showed significant differences in the dealloying rates. For the rough surface, the dealloyed thickness was 4.9μm after 2.5h of dealloying. It increased to 6.6μm after 5h and further increased to 8.6μm after 10h. For the smooth surface, the dealloyed thickness was 3.5μm after 2.5h, kept almost constant for the 5h sample, and increased to 8.6μm after 10h of dealloying. In summary, the convex surface dealloyed slower compared to the concave surface. Similar to the Set A results, the concave and convex sides for Set B samples also showed differences in the dealloying rates. For the smooth surface (concave side), the dealloyed thickness was 1.1μm after 1h of dealloying, increased to 2.8μm after 3h, and further increased to 5.3μm after 6h. For the rough surface

(convex side), the dealloyed thickness was 0.56μm after 1h and increased to 2.1μm dealloying for 3h. In summary, the convex surface dealloyed slower compared to the concave surface irrespective of the initial ribbon surface roughness.

4.1.4 Understanding curvature evolution and crack generation during dealloying

Based on the results, two important observations can be made – the curvature of the partially dealloyed ribbon changed with time, and that the concave (inner) surface consistently developed a thicker layer of NP-Cu regardless of surface roughness. The evolution of curvature during dealloying can be explained based on the differences in the NP-Cu thickness on the concave versus convex ribbon surfaces.

As the ribbon samples dealloy, the NP-Cu layer thickness increases with dealloying time and the NP-Cu / amorphous alloy interface gradually moves farther away from both the top and the bottom faces of the ribbon samples. The NP-Cu has elastic properties (E_{NP}~10-20GPa) [93, 94] that are an order of magnitude lower than the amorphous ribbon (E_{AM}~ 100GPa) and therefore, creates a composite beam whose neutral axis needs to satisfy $E_{NP}\int ydA_{NP} + E_{AM}\int ydA_{AM} = 0$, where y is the distance of an incremental area (dA) from the neutral axis. If the NP-Cu film thickness was doubly-symmetric, then the neutral axis would be located at the center of the ribbon and remain unchanged during dealloying. The differences in the NP-Cu thicknesses formed on both sides causes a shift in the neutral axis location so as to change the flexural rigidity of the beam and impact the moment curvature equation. The curvature κ in the beam then becomes

$$\kappa = M/(E_{NP}{I_{NP}}^{concave} + E_{AM}I_{AM} + E_{NP}{I_{NP}}^{convex}) \quad (2)$$

where M is the applied moment, and I the second moment of area of each material with respect to the composite neutral axis. This curvature can be plotted for the different moduli mismatch values and thickness ratios of the concave to convex films. In this case, where E_{NP}/E_{AM}~0.1, for a convex NP-Cu film thickness of 4μm, the neutral axis is going to move 2μm closer to the convex side for an unsymmetric foam thickness e.g. when $\alpha = 2$ where $\alpha = t_{concave}/t_{convex}$. For the case of $\alpha = 1$, the neutral axis is equidistant from the top and bottom side of the porous solid. The shift in the neutral axis changes the denominator of Equation (2), leading to an increase in the curvature as α becomes greater than 1. Figure 4.7 shows the experimentally measured partially dealloyed ribbon curvature for Sets A and B as a function of the α ratio. It can be seen that an increase in the aspect ratio α correlates with the increased curvature so that an uneven thickness of NP-Cu exacerbates the overall partially dealloyed ribbon curvature. One more interesting finding from classical beam analysis of composite beams is that the stresses in the NP-Cu and amorphous layers are expected to be related through their elastic moduli ratios so that $\sigma_{NP}/\sigma_{AM} = E_{NP}/E_{AM}$~0.1. However, Equation (2) cannot be simply used for the partially dealloyed ribbon problem because there are additional considerations.

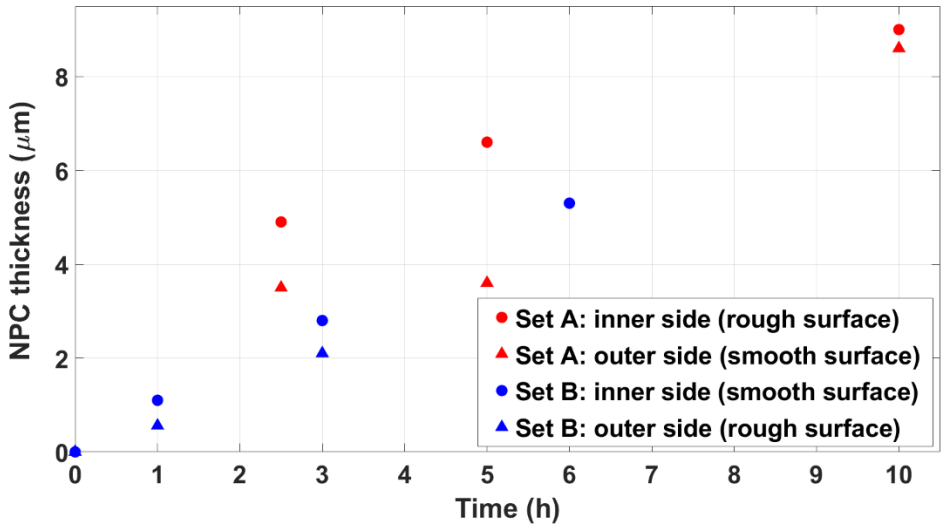

Figure 4.6 Measured thickness of NP-Cu after free corrosion of 10 mm samples for Set A (red) and Set B (blue).

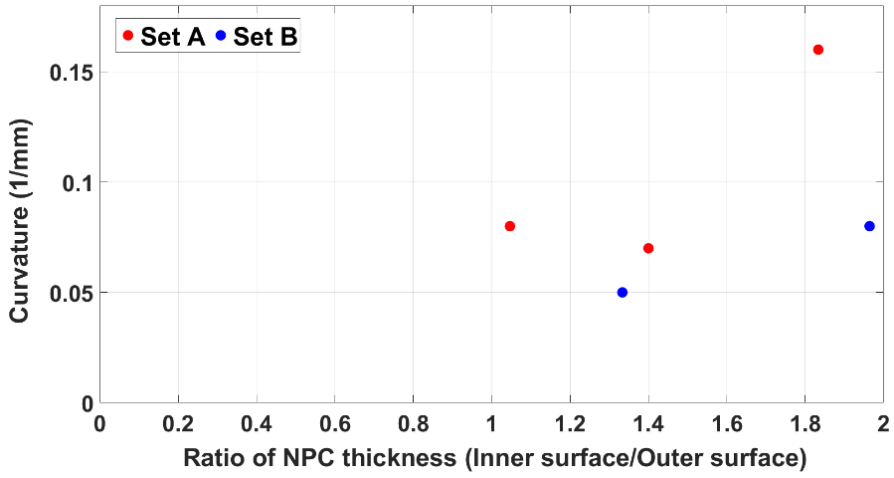

Figure 4.7 Curvature of the Set A and Set B samples as a function of the aspect ratio of the NP Copper thickness.

To add to the complexity of the problem, an unconstrained NP-Cu film will shrink in all the three directions during dealloying [95-97]. However, because of the rigid NP-Cu / amorphous alloy interface, shrinkage of the NP-Cu layer is constrained. This constraint leads to the development of tensile stresses during the dealloying of the NP-Cu film [98], which can lead to crack generation or delamination within the NP-Cu layers.

Recent works have explored the mechanism of formation of a porous layer during the dealloying of amorphous alloys [99]. A partially dealloyed melt-spun ribbon experiences tensile stress on both the concave and convex surfaces, depending on the thickness and morphology of the NP-Cu films. These tensile stresses will change the internal force balance in the beam, generate bending moments, and thereby affect the calculations for curvature. Since the morphology of NP-Cu is effectively the same on both sides of the ribbon, E_{NP} is not expected to be different on either side but will change with time. The modulus of NP-Cu was found indirectly from the ligament dimensions and experimental results for NP-Cu dealloyed from amorphous silicide [93]. Analytical calculations were then derived for the case of a composite beam while taking into account the film shrinkage during dealloying using an expression of the type described in Ref.[95]. Figure 4.8 shows the analysis for Set A. Figure 4.8(a) and (b) show the shrinkage and relative density respectively, as a function of time. The values remained nearly constant with dealloying time. Figure 4.8(c) shows the ligament and modulus of NP-Cu as a function of dealloying time. Figure 4.8(d) shows our model vs. the experimental results. Even if the shrinkage is accounted for, the analytical model overpredicts the curvature by ~60% compared to experimental results.

There can be multiple causes for this discrepancy -

(1) The development of shear stresses at the interface between the amorphous layer and the NP-Cu that can lead to delamination or cracks eventually relaxing the curvature. Delaminated parts were seen in some but not all of our cross-sections. It remains unclear if the sectioning itself was the cause of the delamination.

(2) The analysis based on Equation (2) even accounting for the shrinkage is done under the assumption of a linear elastic material subjected to a moment that is well below the moment needed to initiate yielding. The very fact that our ribbons were coiled, and then maintained a curvature after uncoiling indicates that there is a buildup of residual stresses and plastic deformation in the amorphous ribbon *before* dealloying. Indeed, it is very likely that the bent ribbon was subjected to a moment $\acute{M} > M_i$ where M_i is the critical moment needed to initiate yield at the top and bottom surfaces of the ribbon.

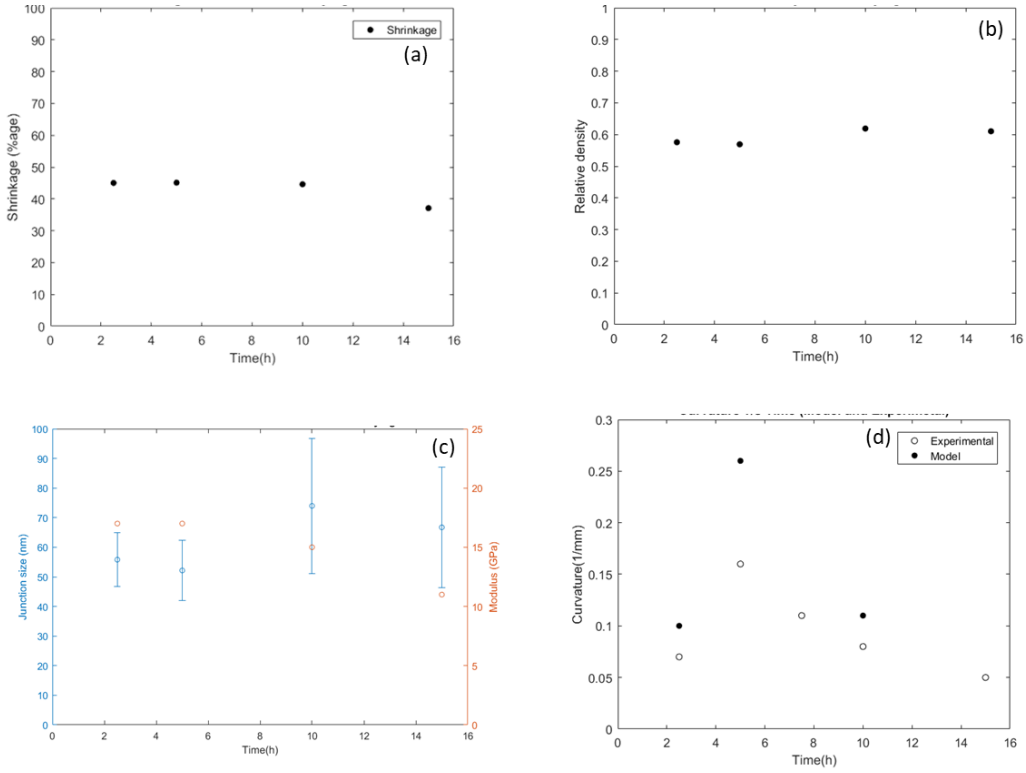

Figure 4.8 Set A experimental measurements of (a) NP-Cu film shrinkage and (b) relative density as a function of dealloying time. (c) Change in the ligament of NP-Cu as a function of dealloying time. The resulting modulus of NP-Cu is also shown on the same plot. (d) Experimental and analytical curvature of Set A as a function of time. The analytical model incorporates an evolving modulus with dealloying time.

4.1.5 Why is the NP Copper thickness higher on the concave side?

Figure 4.9 shows a schematic of the stresses developed in a rectangular beam when subjected to a bending moment $\acute{M} > M_i$ that is beyond initial beam yielding. For a rectangular beam, the moment to initiate yield on only the top and bottom faces, $M_i = 2/3\, w(H_o)^2\sigma_o$ where w is the width, H_o is the height and σ_o is the amorphous ribbon yield stress (~1GPa for our system). Therefore, the initial moment to commence yielding is M_i =110N-mm. After unloading, the elastic part is recovered by applying a differential moment, ΔM, so that the net applied moment is zero, e.g. $\acute{M} - \Delta M = 0$. However, parts of the ribbon that were permanently deformed will retain some residual stress. The profile of the residual stress is shown in Figure 4.9(b) so that application of the moment $\acute{M}$ causes compressive stresses on the concave surface. After elastic unloading, the residual stresses that develop on the concave side are tensile and the ribbon will have a remnant curvature. This was the case for the ribbons in both sets A and B so that the concave side, regardless of surface roughness was expected to be under residual tensile stress in the region near the free surface, while the convex side (outer face) was expected to be under compressive stress. When NP-Cu was formed by free corrosion, the dealloying front progresses more rapidly in the region under high residual tensile stresses (concave) than the convex. It has been reported in the literature that the tensile stresses exacerbate the dealloying rate [100] in a crystalline material. As a result of the faster dealloying under residual tension, two uneven NP-Cu film thicknesses form, thereby exacerbating the initial minimal residual curvature of the amorphous ribbon. We note that the side of the ribbon that was initially concave remains concave after dealloying but the curvature of the ribbon increases. The

observations recorded in this paper indicate the dealloying rate to be influenced more significantly by the initial residual stress state as compared to surface roughness.

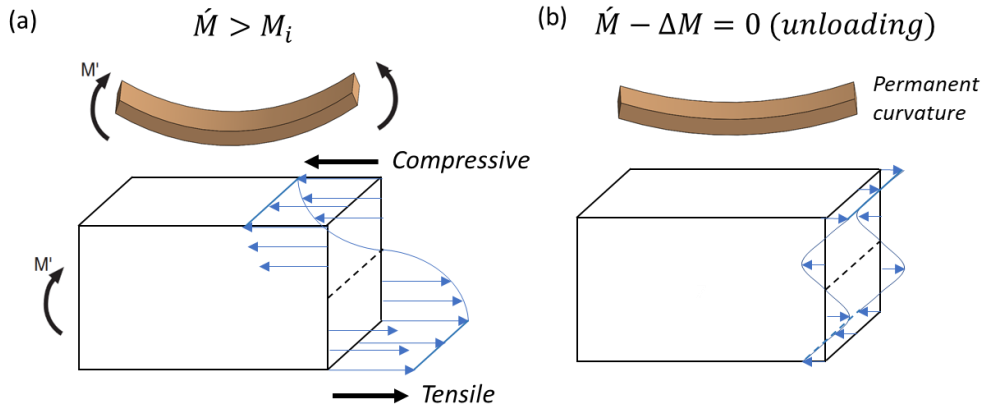

Figure 4.9 Schematic of a rectangular beam deformed beyond the point of yielding so that an applied moment M' results in (a) a linear, still elastic stresses close to the neutral axis but after removal of the moment there are (b) residual stresses in the beam after elastic spring back so that an initial compressive surface (concave) maintains residual tensile stresses close to the surface.

4.2 A shift towards electrodeposition for the synthesis of Cu-X precursor alloy

The dealloying of Cu-Zr-Al amorphous ribbons gave NP-Cu films with cracks and a residual curvature greater than the initial curvature of the ribbons. Imbalance in the dealloying rate at the two free surfaces of the amorphous ribbon due to a difference in their initial stress state was concluded to be responsible for the generation of the bending moments, and, the resulting curvature. As such, the most plausible strategy to avoid the warpage during dealloying would be to make the dealloying rates for both the free surfaces similar. This would ensure a symmetric dealloyed cross-section and the neutral axis would always continue to be located in the center. It was also hypothesized that the difference in the residual stress state of the two free surfaces was a direct result of the initial deformation of the ribbons. Moreover, such initial warpage or deformation of precursor alloy sheets is

unavoidable, especially during the handling of large alloy sheets needed to scale the fabrication process. If an argument can be made that the increase or decrease in dealloying rate is proportional to the amount of tensile or compressive residual stress at the free surface respectively, then it can be concluded that a reduction in the residual stresses will lead to leveling of the dealloying rates at the two free surfaces. A low-modulus or more complaint material will develop lower residual stresses after plastic loading – elastic unloading type deformation as compared to a high modulus material. As such, the use of a low modulus or more compliant material as an interlayer between the top and bottom NP-Cu films might help mitigate the curvature evolution during dealloying. Note – the focus here is on leveling the dealloying rates. However, if the dealloying rates are different, a reduction in the modulus of the interlayer would exacerbate the curvature as can be inferred from Equation (2).

Different fabrication techniques such as sputtering, co-electrodeposition, additive manufacturing (AM) can be used to fabricate such a multilayer structure with Cu-X alloy films deposited on the two sides of a compliant core interlayer as shown in Figure 4.10. On chemical dealloying, large-sheets of NP-Cu films with a compliant core can be fabricated and used for die-attachment. Among the listed fabrication approaches, it was decided to pursue electrodeposition for the deposition of Cu-X alloys because of the following reasons: i) Cu:X ratio can be easily tailored by changing the deposition potential, thus giving flexibility in designing the Cu-X alloys; ii) In addition to fabrication of blanket films, electroplating can also be used to fabricate patterned Cu-X films, which can be subsequently dealloyed to provide patterned NP-Cu films as shown in Figure 4.10; iii) both electrodeposition and chemical etching or dealloying are compatible with semi-additive

processing (SAP) techniques and can be scaled to wafer-level processing, thus improving the overall manufacturability; iv) abundance of existing literature on electrodeposition; v) low-cost and high-throughput as compared to sputtering or AM.

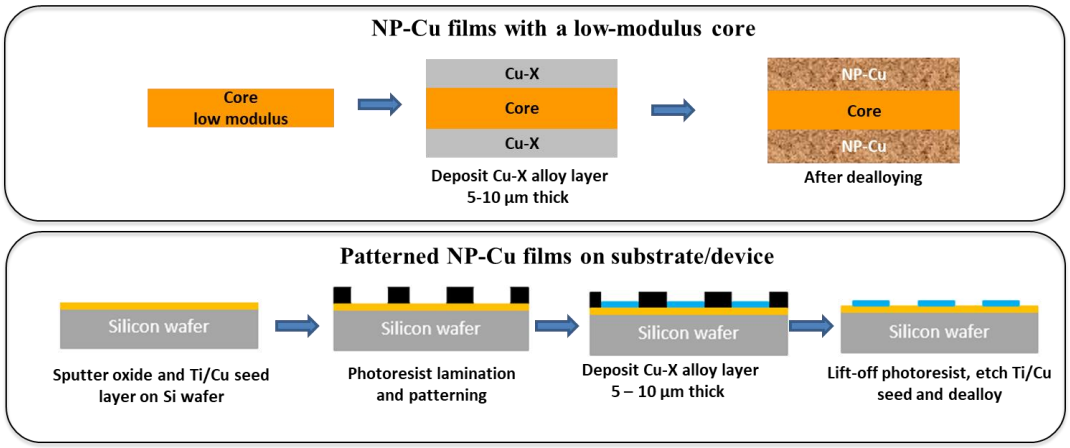

Figure 4.10 Process flow for fabrication of blanket NP-Cu film with compliant core and patterned NP-Cu on die/substrate

4.3 Co-electrodeposition of Cu-Zn alloy films

The chemical composition, phases, and the microstructure of the initial precursor alloy has a strong influence on the properties and morphology of NP-metals [76, 78, 79, 84, 85, 98]. The composition of the more reactive element should be at least more than the parting limit for a complete through-thickness dealloying. However, it is generally recommended to have a significantly higher concentration of the reactive constituent/s as compared to the noble component for a faster dealloying rate and uniform dealloyed structure [76, 78, 79]. This leads to a complicated situation, as the co-electrodeposition of an alloy with a higher concentration of the more reactive component is more difficult as compared to an alloy with a higher concentration of the nobler component. A greater difference in electrochemical potential between the alloy components will generally

provide better selective etching of the reactive element/s. However, for co-electrodeposition elements with similar reduction potentials are preferred. This paradoxical situation severely limits the available Cu-X alloy systems for electroplating and subsequent chemical dealloying. Based on the extensive literature review highlighted in Table 4.1, two alloy systems, Cu-Zn and Cu-Mn were identified. The standard reduction potentials for Cu^{2+}, Zn^{2+}, and Mn^{2+} are listed in Table 4.2.

Table 4.2 Standard reduction potentials of Cu^{2+}, Zn^{2+}, and Mn^{2+}[101].

Half reaction	E^o (V)
Cu^{2+} (aq.) + $2e^-$ → Cu(s)	+0.34
Zn^{2+} (aq.) + $2e^-$ → Zn(s)	-0.76
Mn^{2+} (aq.) + $2e^-$ → Mn(s)	-1.18

From the chemical dealloying perspective, Cu-Mn is more suitable because of a greater difference in the reduction potential. Moreover, Cu-Mn alloys form a single-phase solid solution for a very large composition range. It was discussed in the previous sections that single phase precursor alloys are better for the fabrication of NP-metals with a uniform bi-continuous structure. Cu-Zn, on the other hand, has a lower, but sufficient, reduction potential difference and forms several phases depending on the Cu-Zn composition. Taking into consideration all the above factors, most importantly the extreme difficulty and scanty literature reports on the plating of Mn-rich Cu-Mn alloys, the Cu-Zn system was chosen as the preferred alloy system for the fabrication of NP-Cu.

4.3.1 Selection of pyrophosphate bath for Cu-Zn plating

Electrodeposited Cu-rich brass is one of the most widely used surface coatings and has been plated for well over 100 years. Because of a significant difference of 1.1V between the standard reduction potential of Cu^{2+} and Zn^{2+}, Cu atoms will plate preferentially during the co-electrodeposition process. Therefore, a complexing agent is added to the plating bath to stabilize Cu^{2+} ions in the plating solution, reduce their electrochemical reactivity, and allow co-electrodeposition. Although many types of plating baths and complexing agents have been investigated for plating Cu-Zn alloys [102-109], cyanide-based baths remain the workhorse of the industry. Cyanide-based baths provide coatings which are bright and adherent and have good mechanical properties. Moreover, they provide very good plating control over the full range of Cu-Zn composition and phases [110]. However, due to the extreme toxicity of cyanide baths, it was decided to choose alternate non-toxic bath chemistry for this work. Amongst the non-cyanide baths, a pyrophosphate bath was found to be very promising. Pyrophosphate baths have several desirable characteristics – non-toxic, non-corrosive, high stability, good throwing power, low-cost, and very importantly can produce Cu-Zn alloys in a wide range of alloy compositions [108, 110-112].

4.3.2 The interplay between Cu-Zn alloys composition, phases, and plating parameters

An extensive review of reports on the fabrication of Cu-Zn alloys revealed an interesting and significant finding as illustrated in Figure 4.11. Cu-Zn phases reported for different compositions and fabrication protocols were plotted on a single graph. Different phases or combination of phases are represented on the Y-axis, The light yellow

rectangular bars indicate the equilibrium Cu-Zn phase expected for a particular composition range. It was observed that Cu-Zn alloys fabricated using different plating baths showed significant differences in the as-plated phases even if they had the same composition. Also, the observed phases, for most plating baths, were different from the equilibrium phases expected for a given composition.

Cu-Zn alloys plated using a pyrophosphate bath with the addition of potassium nitrate, represented by dark blue square markers, very closely matched the equilibrium Cu-Zn phases [110]. However, Cu-Zn alloys plated using a pyrophosphate bath with the addition of boric acid, represented by dark blue diamond markers, showed large deviations from the equilibrium phase diagram. XRD analysis revealed the presence of Cu_5Zn_8 (γ phase) for composition as low as Zn ~36 at.% [112].

Since the dealloyed NP-structure is significantly impacted by both the composition and the phases, this is a very significant finding. It can be inferred that composition alone is not an all-inclusive parameter to define the state of the Cu-Zn alloys. The compositional analysis must be complemented with phase analysis as well to fully understand the dealloying behavior of Cu-Zn films with different Zn content. Moreover, any significant change in the fabrication protocol from a set baseline might warrant a fresh characterization of the plated Cu-Zn alloys and subsequent dealloying, even if the composition is kept constant.

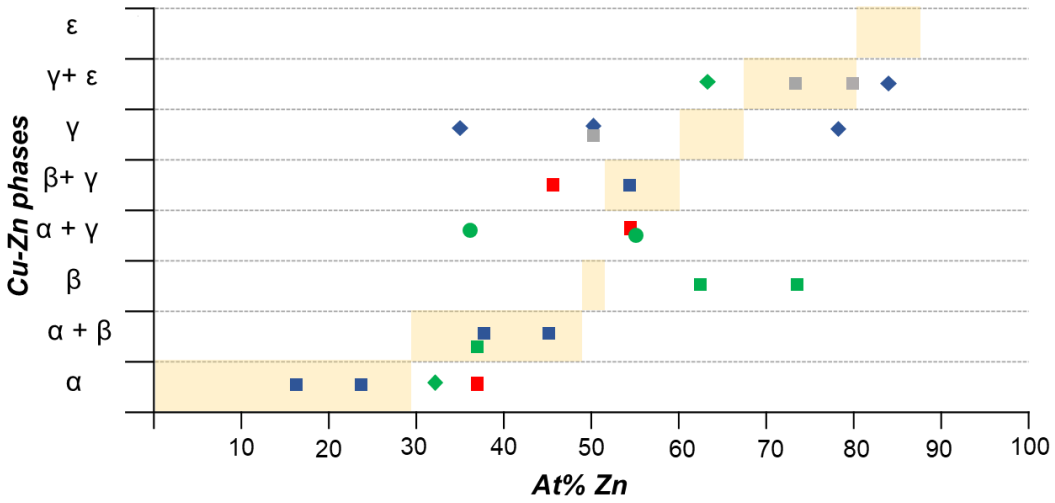

Figure 4.11 Variation in Cu-Zn phases with composition and plating bath summarized from the literature [72, 105, 110, 112-115].

4.3.3 Characterization of Cu-Zn plating bath

4.3.3.1 Motivation

From the very start, the ability to plate on large-area samples was kept in mind. As such changes in the bath volume, design of plating tank, and choice of counter electrodes had to be made as compared to the baseline plating parameters reported in the literature for pyrophosphate-based baths [108, 112, 116]. Moreover, the baseline studies provided compositions with Zn<50at%. However, based on existing literature reports on Cu-Zn dealloying, for this work, Zn-rich Cu-Zn alloys were more desirable [72, 111, 112]. These factors necessitated an extensive re-characterization of the modified plating bath.

4.3.3.2 Methods and materials

Potassium pyrophosphate (PP) ($K_4P_2O_7$, 97%, anhydrous, VWR), $CuSO_4.5H_2O$, $ZnSO_4.7H_2O$ were dissolved in DI water to make the plating solution. The plating solution

was agitated with 99.99% pure N_2 for 60min before starting the plating experiments. The concentration of PP and $ZnSO_4$ was fixed at 0.35M and 0.15M respectively. $CuSO_4$ concentration was varied between 0.004M and 0.025M as shown in Table 4.3. The volume of the plating bath was fixed at 3.5L.

Table 4.3 Composition of the plating baths used in this study.

	$K_4P_2O_7$	$ZnSO_4.7H_2O$	$CuSO_4.5H_2O$	Stirring
Bath 1	0.35M	0.15M	0.004M	100rpm
Bath 2	0.35M	0.15M	0.01M	100rpm
Bath 3	0.35M	0.15M	0.025M	100rpm
Bath 4	0.35M	0.15M	0.01M	No stirring

Polycrystalline Cu sheets (>99.9% purity), 4cm x 5cm (~30µm thick), were used as working electrodes. The plating area was fixed between 16-18cm^2. The sheets were cleaned with acetone, then dipped in 5M H_2SO_4 followed by a DI water rinse, and finally dried in N_2 before plating. Additionally, the plating was done only on one side of the Cu sheets. The other side was covered with an insulating Kapton tape. Zn sheets with >99.9% purity (Alfa Aesar) were used as counter electrodes. Zn sheets were cleaned with acetone, then dipped in 1M HCl followed by a DI water rinse, and finally dried in N_2 before immersing in the plating bath. The change in counter electrodes to Zn from the more commonly used Pt electrodes in literature reports was made from a manufacturability and cost perspective. The area of Zn electrodes was fixed at 35cm^2. The side of the Zn sheet

facing away from the plating side of Cu sheets was insulated using Kapton tape. Ag/AgCl electrode was used as the reference electrode.

Linear sweep voltammetry (LSV) measurements were performed to identify an optimal range of Cu^{2+} and Zn^{2+} co-reduction potential. Potentiostatic electrodeposition was subsequently carried out to deposit Cu-Zn alloys on the Cu sheets. A fixed charge of ~300C was passed for all the potentiostatic platings. The electroplated films were analyzed using SEM, EDX, and XRD.

4.3.3.3 Linear sweep voltammetry (LSV)

LSV measurements were carried out in the range of 0V to -1.8V with a scan rate of $10mVs^{-1}$ for baths 1-3. It was observed that an increase in the Cu concentration in the plating shifted the reduction potential of Cu slightly towards more positive values, however, the impact was not significant. LSV results for bath 1 are analyzed in Figure 4.12. Cu reduction started at ~ -0.4V. A change in slope is observed at ~ -0.9V, which points towards the start of H_2 evolution. Another change in slope was observed at ~ -1.25V, which points towards the reduction of Zn^{2+}.

Based on the analyses, a co-reduction potential window of -1.25V to -1.4V was selected for further exploration. The rationale was to maximize the plating current density to be able to plate Zn rich Cu-Zn alloys while also minimizing H_2 evolution at the working electrode. H_2 evolution during Cu-Zn plating has been shown to form cracks and voids in the electrodeposited films as well as increase their embrittlement [104, 108, 112, 116].

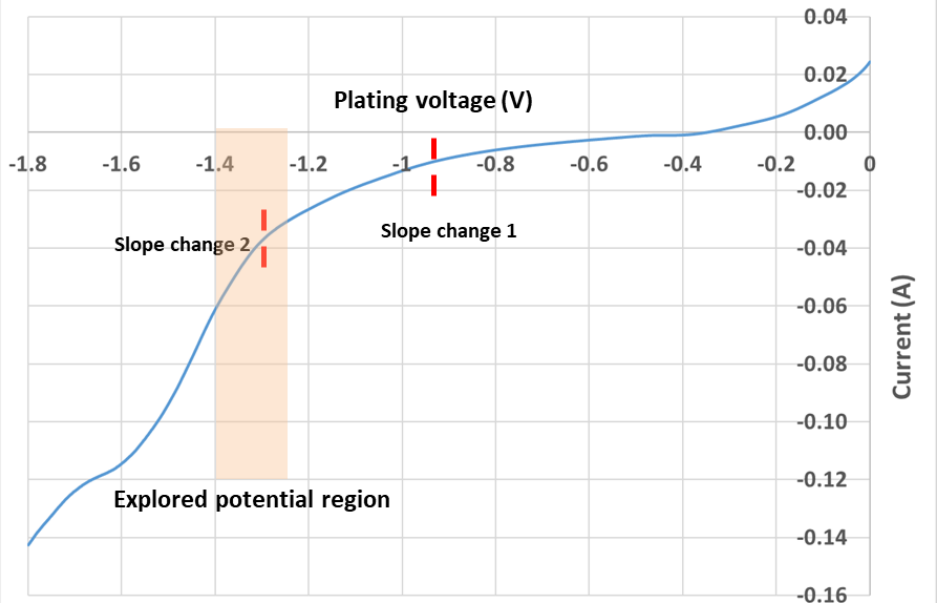

Figure 4.12 Linear sweep voltammetry for Bath 1 (voltage measured with respect to Ag/AgCl reference electrode).

4.3.3.4 Electrodeposition and characterization of Cu-Zn alloy films

Potentiostatic electrodeposition was carried out for the four plating baths highlighted in Table 4.3. Four different plating potentials were considered: -1.27V, -1.3V, -1.33V, and -1.36V. A fixed charge of ~300C was passed and the plating time for the different runs varied between 2-8h. The current densities were measured to be in the range 0.8 – 2.5mA/cm^2 for different runs. However, for all the platings, current density remained stable throughout the plating, suggesting high stability of the plating bath.

The composition of the plated films was analyzed using EDX. EDX measurements were carried out on five points on the top surface of the plated films. The results indicated the presence of Cu, Zn, O, C, K, and P on the surface of the electrodeposited coatings, confirming the presence of contaminants from both the electrolyte and the atmosphere. Moreover, the contamination of C, O, P, and K was higher for films with Zn<50 at.%. The

EDX results also confirmed the very high uniformity of the plated composition across the plated area. Cu and Zn concentrations were normalized to remove the effect of the contaminants. Normalized average Zn concentrations (by at.%) are shown in Figure 4.13 for all the Cu-Zn platings. A few key observations can be made:

- The selected combination of plating bath composition and process parameters can provide Cu-Zn films within a wide composition range.

- Increasing the reduction potential increased the Zn content in the Cu-Zn films for all the plating baths. This was expected as the plating baths have an excess of Zn^{2+} salts. Therefore, any increase in the plating potential in the co-reduction potential range should result in a comparatively higher increase in the deposition rate of Zn^{2+} as compared to Cu^{2+}.

- The increase in the amount of Zn seems to taper off with an increase in reduction potential. This suggests that sluggish mass transport of pyrophosphate metal complexes limits the plating current density at higher reduction potentials. As such, the use of additives to improve the mass transport of metal ions in the bath can be considered for achieving higher plating current densities or for plating even more Zn-rich alloy films.

- Stirring or agitation of the bath increases the Cu concentration in the platings. In a bath with no agitation, the electrolyte at the surface of the Cu electrode would get depleted of Cu^{2+} faster than Zn^{2+} because of a significantly higher starting concentration of Zn^{2+} in the bath. The agitation of the bath would replenish the Cu^{2+}

at the Cu electrode/electrolyte interface, giving higher Cu concentration in the Cu-Zn coatings.

- Since the mass transport becomes the critical factor in limiting the plating current densities at higher reduction potentials, varying the concentration of Cu^{2+} in the plating bath is a better strategy to adjust the plated compositions, especially when Zn-rich coatings are more desirable.

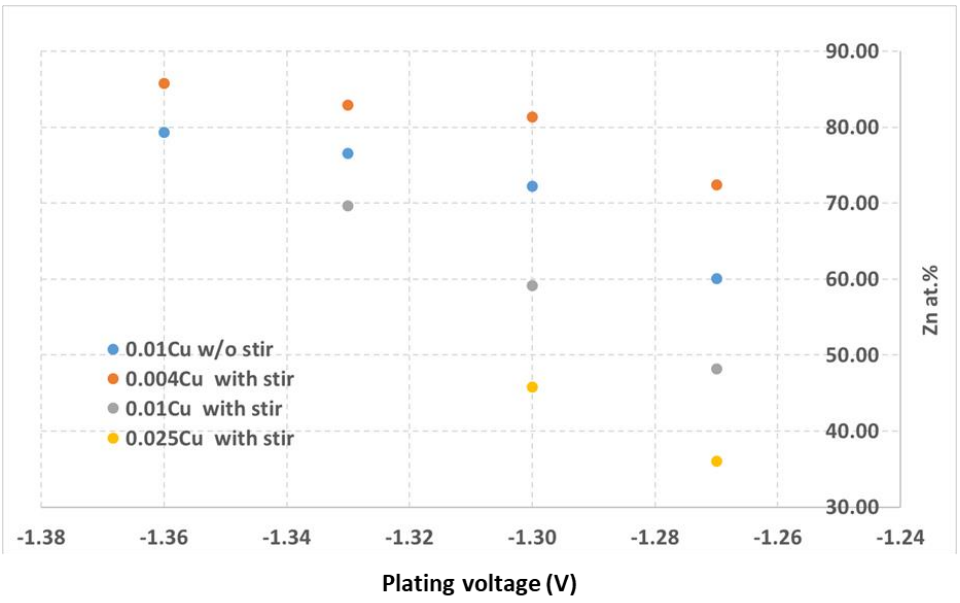

Figure 4.13 Effect of plating potential and bath conditions on plating composition.

All the plated films were further characterized for top-surface microstructure using SEM and for constituent phases using XRD with two-fold objectives: a) To understand the relationship between composition, microstructure, and phases present; b) To downselect a limited number of compositions or plated films for further evaluation of their chemical dealloying behavior. The limited selection must be able to capture the dealloying behavior of the Cu-Zn alloys in a wide composition range.

SEM analyses showed a very clear trend for the change in microstructure with increasing Zn content in the Cu-Zn platings. For films with Zn <50at.%, the plated surface was characterized with large spherical grains with well-defined grain boundaries. With a further increase in Zn concentration, the plated structure became finer and compact with cauliflower-like morphology. When Zn concentration became ~75at.%, thin plate-like structures with hexagonal appearance were observed along with the cauliflower-morphology grains. As the Zn increased to more than 80at.%, the transformation was complete, and the plated surface was characterized by grains with hexagonal morphology and well-defined facets.

Based on the microstructural changes, five different plated films A-E with Zn concentration - ~35at.%, ~50at%, ~70at%, ~75at%, and ~85at% respectively as highlighted in Table 4.4, were selected for XRD and further dealloying analysis. The microstructures and XRD graphs of the selected compositions are shown in Figure 4.14 and Figure 4.15 respectively. For composition A and B, XRD signals indicated primarily the presence of the α phase. As the Zn increased to ~70at%, a phase shift from α to primarily γ occurred, however weak signals of the ε phase were also be detected. For sample E with Z n>85%, the signals indicated primarily the presence of the ε phase. The peak values used for analysis are highlighted in

Table 4.5. XRD analyses confirmed beyond doubt that indeed the change in the microstructure is directly related to the change in phases in the plated alloys with an increase in Zn content. The phases observed in the plated films very closely match the equilibrium phase diagram. One possible reason for this could be the low current densities and lower overpotentials as compared to other pyrophosphate-based studies in the

literature. It has been reported that higher overpotentials could result in higher lattice distortions and non-equilibrium phases [116]. Since the plating current densities were low, the plating overpotentials must also be small. XRD analysis also increased the credibility of the downselection approach. The selected compositions did show very different phases, confirming that composition A-E is a good set to understand the dependence of dealloying behavior on the trio of as-plated phases, compositions, and the microstructures.

Table 4.4 Zn concentration in plated samples selected for further studies.

Sample ID	Zn concentration (at.%)
A	~35
B	~50
C	~70
D	~75
E	~85

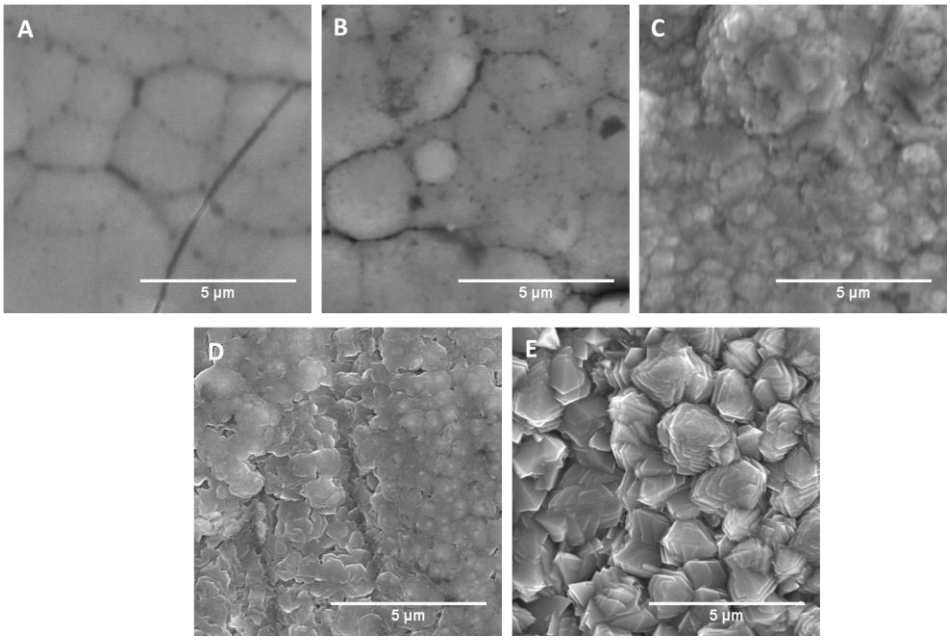

Figure 4.14 SEM microstructure (plan-view) of samples A, B, C, D, and E

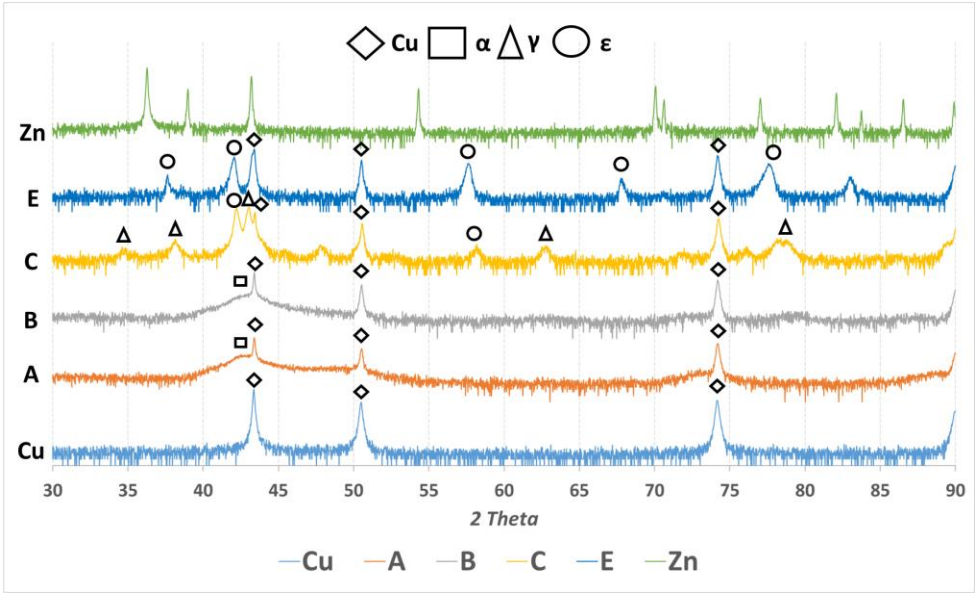

Figure 4.15 XRD peak analysis for Cu, Zn, and samples A, B, C, and E.

Table 4.5. Peak values of different phases used for XRD analysis.

Phase	Peak values	Reference database
Cu (FCC)	43.9°, 51.0°, 74.7°, 90.4°	ICDD ID: 003–1018
α (Cu_3Zn)	42.4, 49.3, 72.7	ICSD ID : 629461
γ (Cu_5Zn_8)	35.6°, 38.3°, 42.8°, 48.6°, 53.3°, 63.4°, 79.8°	ICDD ID: 025– 1228
ε ($CuZn_4$)	38.1°, 42.4°, 43.8°, 58.2°, 68.6°, 78.2°	COD ID:1524894

4.4 Dealloying behavior of plated Cu-Zn films

The primary objective of the above-discussed work on Cu-Zn plating was to understand the dealloying behavior of Cu-Zn plated films with different compositions and structures and choose the optimal composition for the fabrication of large-area NP-Cu films. To this end, the five different plates samples that were selected in the previous section were dealloyed in HCl. Two different HCl concentrations were used 1M and 0.05M. Smaller sections, ~ 10mm x 5mm, were cut from the plated samples and free dealloyed in HCl for four different dealloying times – 15min, 60min, 180min, and 360min. SEM and EDX analysis were performed on the top surface of the dealloyed films for characterizing the nanostructure evolution and residual Zn after dealloying.

Figure 4.16 shows the microstructure after 60min of dealloying time in 0.05M HCl. It was observed that all the samples except sample C gave microstructures with nanoscale morphologies. Prior work suggests that Zn-rich Cu-Zn alloys are better for the dealloying and formation of NP-Cu films [111, 112]. Therefore, dealloying results for composition D and E were on expected lines. Composition C with ~70at.% Zn and containing predominantly γ phase can also be considered as Zn-rich, and therefore its dealloying results were unexpected. Contrary to our findings, multiple reports have indeed demonstrated the successful fabrication of NP-Cu from Cu-Zn alloys containing the γ phase [72, 112]. One possible reason for the chemical resistance of sample C could be the very compact plating coupled with the presence of predominantly a single γ phase which makes the penetration of etchant difficult due to the absence of plating inhomogeneities and defects.

The most interesting results were obtained for samples A and B. Both these compositions have Zn<50% and therefore, can be considered Cu-rich. Contrary to most reports which suggest Zn-rich Cu-Zn alloys for good dealloying, the dealloying results indicated very good dealloying ability for both A and B. The dealloyed surface of sample B showed a uniform bi-continuous nanoscale morphology while the dealloyed surface of sample A appeared more like a network of coalesced nanoscale ligaments.

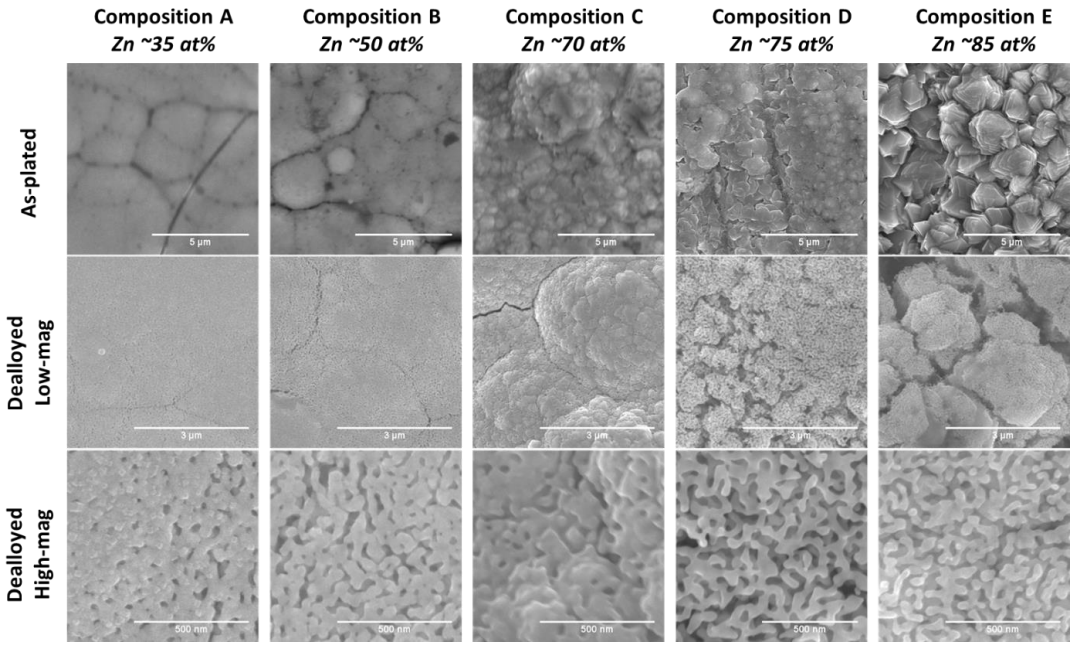

Figure 4.16 SEM images showing the plan-view microstructures after 60min of dealloying in 0.05M HCl for samples A, B, C, D, and E.

An additional literature review was done to confirm these results focusing on Cu-rich Cu-Zn alloys. It was found that very limited prior work exists on the dealloying of Cu-rich electroplated Cu-Zn films [111, 117]. One of the reports demonstrated successful NP-Cu fabrication after dealloying of Cu-Zn plated films with Cu>95%, however, the formation of nanostructure was attributed to etching of CuO rather than Zn. In another report, Cu-Zn alloy with surface Zn concentration of 36at.% showed effective removal of Zn after dealloying in 1M HCl, however, a nanoporous structure was not observed. It is interesting to note that the parting limit for removal of Zn was established at Zn>20%, though the penetration depth of dealloying as such low Zn concentrations was not quantified [81].

In addition to uniform nanostructured morphology, NP-Cu films also need to have low residual Zn for them to be considered for die-attachment. High residual Zn after

etching can result in intermetallics formation and cause corrosion of the sintered joints, thereby, decreasing the reliability of the die-attach joints. To quantify residual Zn, EDX measurements were done on the dealloyed films. Figure 4.17 shows the variation of residual Zn with dealloying time up to 360min for the 5 different Cu-Zn plated films. It was observed that Zn was almost fully etched (Zn < 3at.%) for samples A, B, and E. Sample C showed a very small decrease in the Zn concentration with dealloying time which is consistent with the observed dealloyed microstructure. Sample D showed slow and steady removal of Zn, with ~40 at.% residual Zn after 360min of dealloying. It is expected that with an increase in dealloying time will further decrease the residual in sample D.

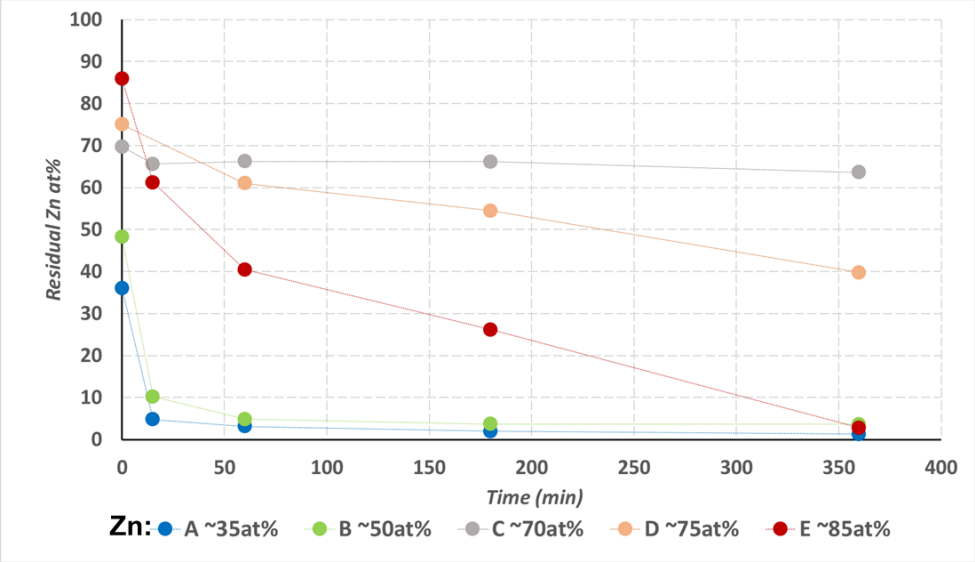

Figure 4.17 Variation of residual Zn with dealloying time for samples A, B, C, D, and E in 0.05M HCl.

Another interesting aspect was the rate of removal of Zn during dealloying from the plated films. Very fast Zn etch rates were observed for samples A and B, so much so that the residual Zn dropped to less than 10 at.% within 15min, and was less than 5at.% after 60min. Sample E also showed a fast Zn etch rate for the first 60min of dealloying, but

the etch rate became slower thereafter. Prior work suggests that higher the concentration of the reactive element in an alloy faster would be its etch rate [78]. However, it is a purely composition driven argument that does not account for the relative stability of different phases in an etchant or the role of processing induced inhomogeneities or defects in the alloy on etching. One possible reason for the faster etch rate of Zn in samples A and B could be the presence of uniformly interconnected grain boundaries in the as-plated films which provide a channel for easy percolation of the etchant and the removal of the Zn atoms.

Figure 4.18 shows the effect of the etchant concentration of residual Zn. Two concentrations, 0.05M HCl and 1M HCl were used for dealloying. In general, faster etch rates are obtained by using a higher etchant concentration [78, 79]. However, samples B and D showed very similar residual Zn with dealloying time for both the etchant concentrations. In sample E, 1M HCl did etch the Zn faster, however, the residual Zn did drop to <3 at.% fo both the etchants after 360min of dealloying. These results show that 0.05H HCl is an effective etchant for dealloying Cu-Zn alloys, capable of giving both low residual Zn and good etch rates.

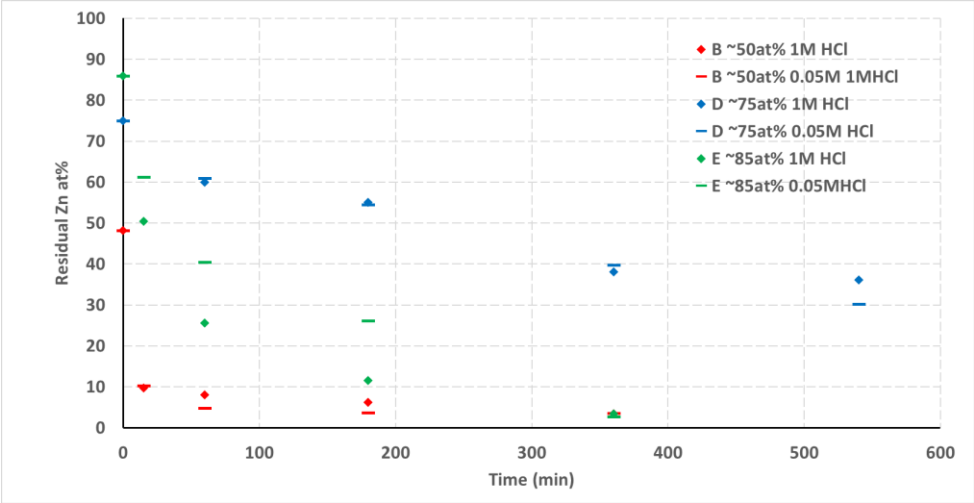

Figure 4.18 Variation of residual Zn with both dealloying time and etchant concentration.

Figure 4.19 and Figure 4.20 tracks the evolution of NP-structure with dealloying time. It was observed that for samples D and E, the ligament thickness increased with dealloying time. These results follow the trend found in literature, where surface-diffusion of Cu atoms at the etchant/NP-Cu boundary leads to rearrangement of Cu and coarsening of NP-Cu structure. Coarsening is thermodynamically favorable as it lowers the surface energy of NP-Cu. However, for composition B, ligament thickness first increased marginally and then decreased with dealloying time, which is in contrast to the general trend. Overall, the dealloying results for composition A and B show significant deviations from the prior work. More experimental data and analysis are required to understand the dealloying behavior of composition A and B.

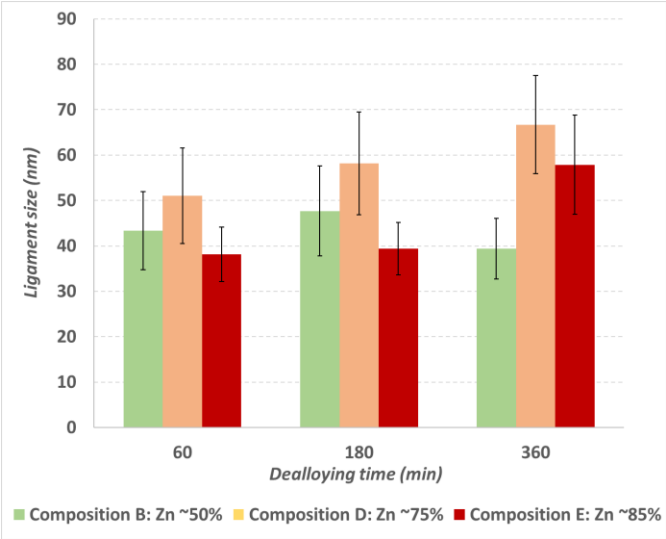

Figure 4.19 Ligament thickness evolution with dealloying time in 0.05M HCl.

Another important comparison can be made based on the ligament thickness of NP-Cu films with residual Zn below a certain threshold concentration. Such a threshold for residual Zn would have to be determined by analyzing the impact of residual Zn on the reliability of sintered NP-Cu die-attach. For now, an arbitrary value of ~5at.% was chosen for the sake of explaining the thought process. However, the analysis will hold if the actual threshold value is less than 5at.%, which is most likely going to be the case. The ligament thickness of the dealloyed NP-Cu films was measured when the residual Zn dropped below 5at.% and it was found that samples A and B gave the smallest ligament thickness. For sample B, the residual Zn dropped below 5at.% after approximately 60min of dealloying in 0.05M HCl whereas, for sample E, it took about 360min of dealloying time. The average ligament thicknesses were measured to be ~43nm and ~58nm for NP-Cu films dealloyed from composition B and E respectively.

This is significant because two of the key desired parameters for designing an NP-Cu system for die-attachment are low-temperature sinterability and low-modulus.

Nanoscale materials sinter at much lower temperatures as compared to their bulk counterpart because of their very high internal surface energy. An increase in the surface area increases the internal energy, and to that extent, NP-Cu films with finer ligament thicknesses are more desirable.

However, prior works have also suggested an increase in the modulus with a decrease in ligament thickness for NP-metal films, especially so when ligament thicknesses become smaller than 20nm [118]. Therefore, an argument can be that such a ligament thickness is desirable which gives an optimal combination of high surface area and low-modulus. In our case, the average ligament size of NP-Cu films dealloyed from samples B and E is ~43nm and ~58nm respectively. Both these values are significantly higher than 20nm, therefore not a significant difference in modulus is expected between the two NP-Cu films. However, NP-Cu films dealloyed from sample B will have a higher surface area, and potentially, higher surface energy and better sinterability as compared to NP-Cu films dealloyed from Sample E.

Therefore, it can be concluded that among the 5 selected compositions, based on Zn etch rate, residual Zn and ligament thickness, Cu-Zn alloy films with composition Zn <50at.% are the most suited for fabrication of large-area NP-Cu films for die-attachment. Moreover, Cu-Zn films with Zn<50 at.% are easier to plate as compared to Zn-rich Cu-Zn films. The plating can be carried out at lower reduction potentials which will help in reducing the in H_2 evolution and improving the charge efficiency of the plating bath. However, it must be noted that the above conclusion is based on some assumptions made on the impact of ligament size on modulus and sinterability which needs to be confirmed with experimental data.

4.5 Effect of local plating compositional variations of dealloyed NP-structure

Any manufacturing process must have some inbuilt tolerance to process variations for both high process manufacturability and high yield. Electrodeposition of binary or ternary alloys, when carried out on large-scale is very likely to give some local variations in the plating composition across the sample. The sample can be a wafer, a panel, or a metallic sheet. Such variations are likely to even more aggressive for the Cu-Zn alloy system because of the high difference in reduction potentials of Cu^{2+} and Zn^{2+}. As such, any variations in the local pH, overpotential, or concentration of metal ions at the electrode/electrolyte interface can cause significant variations in Cu-Zn composition across the sample. Therefore, it is imperative is to understand the impact of such local compositional variations on the dealloying behavior across the entire sample, if any.

To study this aspect, an experiment was designed to intentionally induce differences in the Cu-Zn composition between different areas of the sample, while also keeping the maximum Zn less than 50at.%. The target maximum Zn concentration is based on our hypothesis that Cu-Zn films with Zn <50 at.% are ideal for the fabrication of large-area NP-Cu films. Figure 4.21 shows the plated sample and the composition map of Cu-Zn films at different coupons in the sample. The concentration of Cu was lowest for the top row coupons at ~57at.%, while it was highest for the bottom row at ~67at.%, giving a significant composition variation between the top and bottom rows.

All the coupons were dealloyed in 0.05M HCl for 60min and SEM images of the top surface were taken after dealloying. It was found that all the coupons gave NP-Cu films with a similar nanostructure having an average ligament thickness of ~45nm as can be seen

in Figure 4.22. This is a very significant finding, as it shows that if Cu-Zn films with a target composition of Zn~50at% were to be plated on wafer-scale, the local variations in the composition across the large sample will have minimal impact on the dealloying of the Cu-Zn films and NP-Cu films with similar morphology are expected on the entire sample which is very good from the viewpoint of manufacturability.

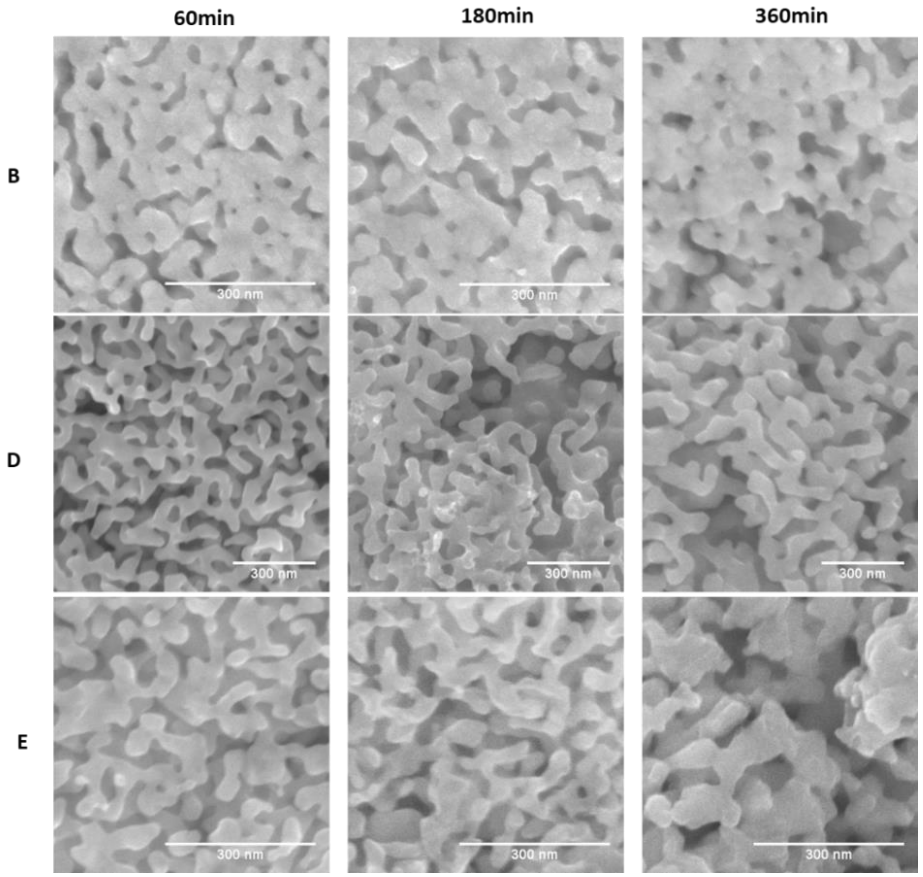

Figure 4.20 NP-Cu structure evolution with dealloying time in 0.05M HCl.

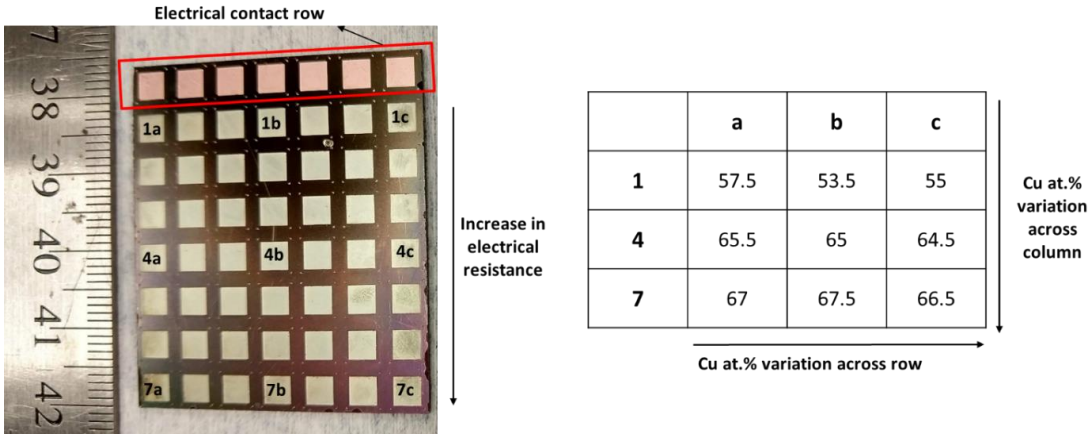

	a	b	c
1	57.5	53.5	55
4	65.5	65	64.5
7	67	67.5	66.5

Figure 4.21 Sample with induced differences in Cu-Zn composition.

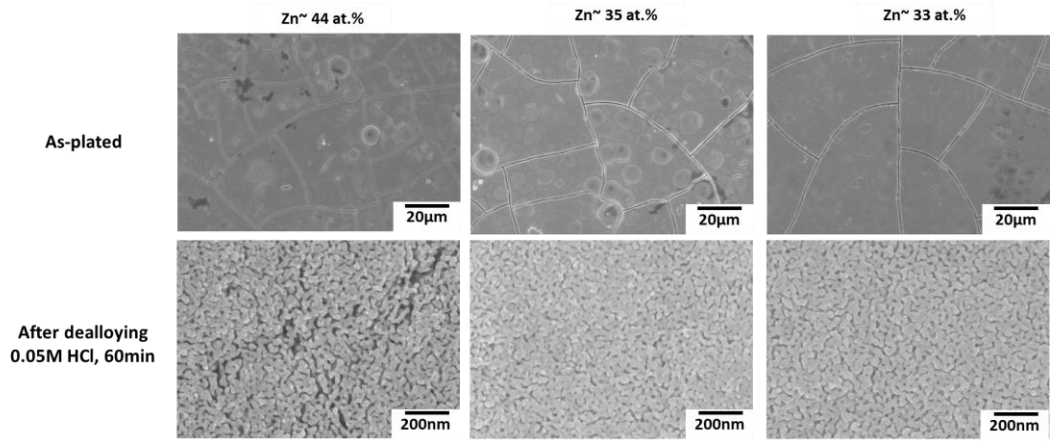

Figure 4.22 Dealloyed structure for three coupons with different Cu-Zn composition.

4.6 Demonstration of NP-Cu samples for die-attach

(Note that the Cu-Zn plating and dealloying optimization was carried out between Sep 2019 – March 2020. Before that, for all the experimental work, Cu-Zn films with Zn >80at.% were used.)

One of the main motivations for developing the co-electrodeposition process was its potential for the fabrication of both blanket NP-Cu films with Cu core and patterned

NP-Cu films directly on a conducting substrate. The fabrication of blanket sheets of NP-Cu is straightforward. Cu foil was used as the core conducting material. Cu-Zn films with Zn >80at.% were plated on both sides of the foil. Subsequently, the full stack-up was dealloyed in HCl to give standalone NP-Cu films with Cu core. SEM image of the cross-section can be seen in Figure 4.23.

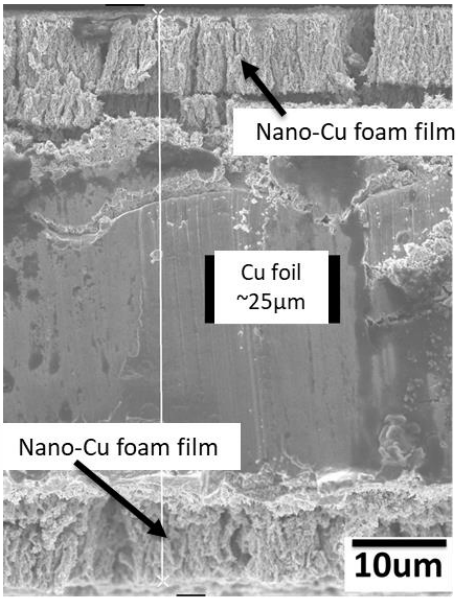

Figure 4.23 SEM cross-section of Np-Cu films with a Cu core.

However, the development of patternable NP-Cu films was more tricky as it also involved developing the patterning process itself. The process flow used to fabricate patterned NP-Cu films is highlighted in Figure 4.24.

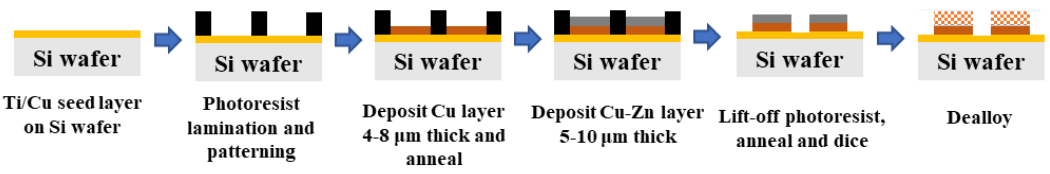

Figure 4.24 Process flow for the fabrication of patterned NP-Cu films.

Si wafers with sputtered Ti/Cu seed were used as the base substrates. Liquid plating photoresist from JSR Corporation was spin-coated, exposed, and developed to form 6.5mm x 6.5mm square patterns on the Si wafer. After photoresist patterning, 4-8μm of Cu was plated on the Cu seed layer and the samples were annealed to relieve the plating stresses in the plated Cu. Annealing was followed by the co-deposition of 5-10μm of Cu-Zn. Plating current densities were maintained in the range of 3-6mA/cm^2. Then, the photoresist was stripped and the samples were annealed at 150°C for 5-15min. This was followed by dicing the sample into smaller samples, which were finally dealloyed to fabricate np-Cu films on plated Cu. Figure 4.25 shows the samples after Cu-Zn plating, dicing, and dealloying.

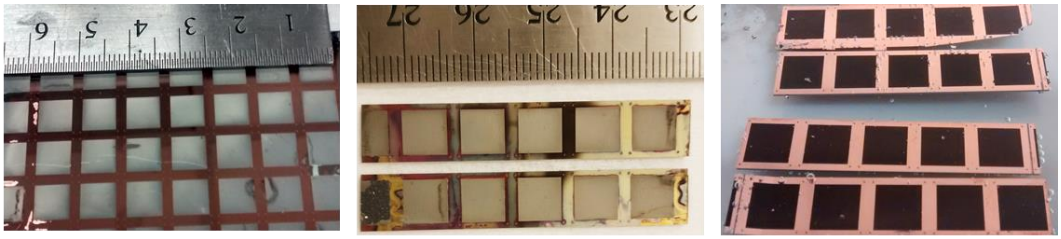

Figure 4.25 Images showing the samples at different stages in the fabrication of patterned NP-Cu films.

Figure 4.26 shows the thickness after plating both Cu films and Cu-Zn films. The images were taken using the Zeta profilometer. The initial thickness of the electroplated Cu layer was ~5μm. On top of the Cu layer, ~7μm Cu-Zn layer was deposited. Subsequently, individual dealloyed coupons were isolated and used for bonding as discussed in the following sections.

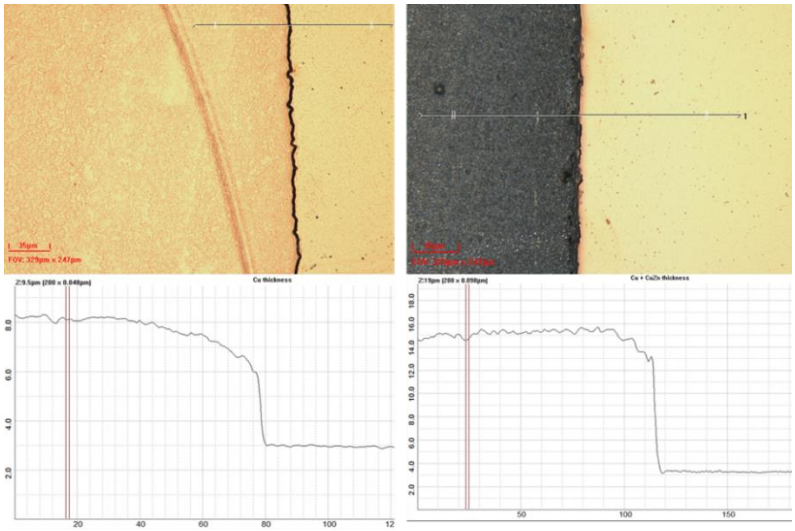

Figure 4.26 Profilometer images showing the variation in plated thickness of (left) initial Cu film and (right) Cu-Zn film for sample plated at 5.5mA/cm2 for 45min.

4.7 Chapter summary

This chapter summarizes the research done towards the fabrication of large-area NP-Cu die-attach films. Cu-Zr-Al melt-spun amorphous ribbons were dealloyed with the intention of fabrication NP-Cu inserts for die-attach applications. However, the dealloyed ribbons developed cracks and curvature during dealloying, making the dealloyed NP-Cu films unsuitable to use for die-attachment. Subsequently, an alternate approach involving co-electrodeposition and dealloying of Cu-Zn films was proposed and designed for the fabrication of both standalone as well as patterned NP-Cu films. Pyrophosphate-based baths were selected to co-deposit Cu-Zn alloys. The electroplating bath was extensively characterized using a mix of characterization techniques. It was found that Cu-Zn films with 33 at.%< Zn <50at.% and consisting primarily α phase are most suitable for dealloying and scaling the fabrication to wafer or panel scale. The dealloyed NP-Cu films from this composition were characterized for ligament thickness and residual Zn. The residual Zn

was <3 at.% while the average ligament thickness was ~42nm. It was also shown that local variations in composition if the Zn <50at.% will have minimal impact on dealloying. Finally, NP-Cu films, both patterned and standalone, that can be used for die-attachment were demonstrated.

CHAPTER 5. DEMONSTRATION OF CU-CU JOINTS BY FILM SINTERING OF NANOPOROUS-CU FILMS

NP-metals are a relatively new type of materials and many of their properties are still under research. Sintering of NP-metals, in particular, NP-Cu, is of most interest for this work. To yield an all-Cu die-attach joint, NP-Cu films must be able to form metallurgical bonding interfaces with Cu finish on both the dies and substrates, as well as show high densification at temperatures as low as 250°C. Therefore, it becomes critical to fundamentally understand the sintering kinetics of NP-Cu films, with a focus on understanding the sintering behavior with differences in np-Cu morphology and ligament sizes.

In the classical sintering models illustrated on two-particle models (Coble [119]), the evolution of particle-pore structures is identified by three stages of sintering. The initial stage is characterized as the formation and growth of contact between neighboring particles. In the intermediate stage, the pore structure evolves into an interconnected channel with cylindrical pores lying primarily along grain edges. The final stage begins when the pinch-off interconnected pore channel forms closed pores at the relative density of >0.9. The final stage of the sintering of crystalline particles is usually accompanied by coarsening and grain growth.

In previous studies [120, 121], temporal power law of grain size evolution has been used to fit coarsening kinetics of nanoporous materials. This is equivalent to the initial

stage coarsening and densification within nanoparticles [122]. The coarsening kinetics are estimated by a log-linear fit of the characteristic length v/s time, i.e.

$$\lambda(t^n) = k_0 t \, exp\left(\frac{-E_a}{RT}\right) \quad (3)$$

where λ(t) is the characteristic length evolving at time t, k_0 is pre-exponential constant, n is the coarsening exponent, E_a is the activation energy for sintering, R is the gas constant and T (K) is the annealing temperature.

In this chapter, first, the results on the sintering of NP-Cu films are presented. A comparison is made between the sintering behavior in different reducing atmospheres and at different temperatures. Finally, assembly results are shown, and the effect of different assembly parameters is discussed.

5.1 Sintering of NP-Cu films

5.1.1 Effect of sintering temperature

The Zn-rich Cu-Zn alloy films (Zn>80 at.%) were first co-deposited on Cu sheets and then dealloyed in dilute HCl to fabricate NP-Cu films on Cu sheets. The fabricated samples were kept out in the ambient atmosphere for two days to facilitate NP-Cu oxidation. On the third day, the samples were sintered in a Rapid Thermal Processing (RTP) furnace equipped with 2% forming gas (H_2 + N_2). The heating rate was maintained at 30°C/sec. Before annealing, the samples were treated with 33% formic acid for 60sec. The sintering temperatures were varied between 200-300°C and the sintering time was kept constant to 60mins.

Figure 5.1 shows the SEM images of as-fabricated NP-Cu (Figure 5.1a) and after sintering at different temperatures (Figure 5.1b-d). The SEM images were analyzed in ImageJ for the measurement of the ligament dimensions. The as-fabricated NP-Cu films had a ligament thickness of ~45nm. Different sintered morphologies were observed after sintering at different temperatures. At 200°C, the ligaments successfully fused together, however, the growth in individual ligament dimensions was not significant. Similar morphology was also observed at 250°C but with more coarsened ligaments. At 300°C, a significant increase in ligament dimensions was observed, wherein the ligament thickness increased to ~95nm. Multiple reports have suggested 250°C as the activation temperature of forming gas for the reduction of copper oxides. The limited densification at 200°C and 250°C could be due to insufficient removal of surface copper oxides during sintering or insufficient sintering temperature. Further experiments and evaluations are needed to assess the impact of temperature on sintering kinetics and oxide removal.

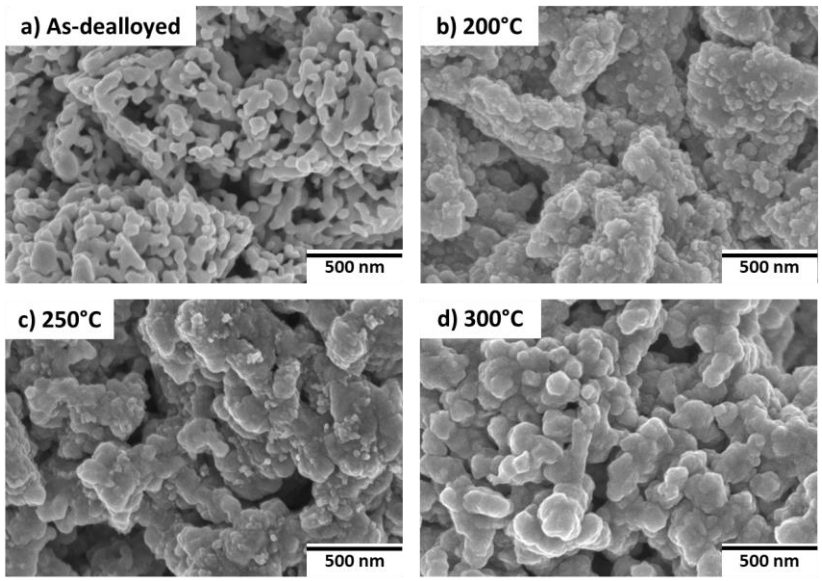

Figure 5.1 SEM images of NP-Cu: a) as fabricated; b-d) sintered at different temperatures.

5.1.2 Effect of sintering atmosphere

Cu-Zn films with ~47 at.% Zn were electroplated on Cu foils and subsequently dealloyed to fabricate NP-Cu films on Cu sheets. The fabricated samples were kept out in the ambient atmosphere for two days to facilitate NP-Cu oxidation. On the third day, the samples were sintered in a Rapid Thermal Processing (RTP) furnace at 275°C. A ramp rate of 30°C/sec was maintained. All the samples were dipped in 0.05M HCl to remove the surface oxides before sintering. Figure 5.2a shows the SEM image of as-dealloyed NP-Cu films with a ligament thickness of 40-50nm. First, the NP-Cu films were sintered under an N_2 atmosphere and an increase in the ligament thickness to ~95nm was observed as shown in Figure 5.2b. The NP-Cu films were also sintered under a 2% forming gas environment, shown in Figure 5.2c. A higher degree of densification and increase in ligament thickness was observed as compared to the NP-Cu films sintered under an N_2 atmosphere. It must be noted that there was a time gap of 4-5mins (1-2mins for transferring samples from the cleaning station to the RTP furnace and 3mins of N_2 purge of the RTP furnace) between the cleaning of surface oxides on the NP-Cu films in dilute HCl and the start of sintering in the RTP furnace and therefore, surface oxides are expected to be present on the NP-Cu films before the start of the sintering process. To prevent this surface oxidation, two drops of 33% formic acid were dropped on the NP-Cu films immediately after the oxides were removed using the dilute HCl. These samples were then sintered in the furnace under 2% forming gas and the sintered microstructure is shown in Figure 5.2d. The NP-Cu ligament thickness increased significantly from ~45nm to >600nm. The results underline the importance of a suitable reducing atmosphere for the efficient sintering of NP-Cu films.

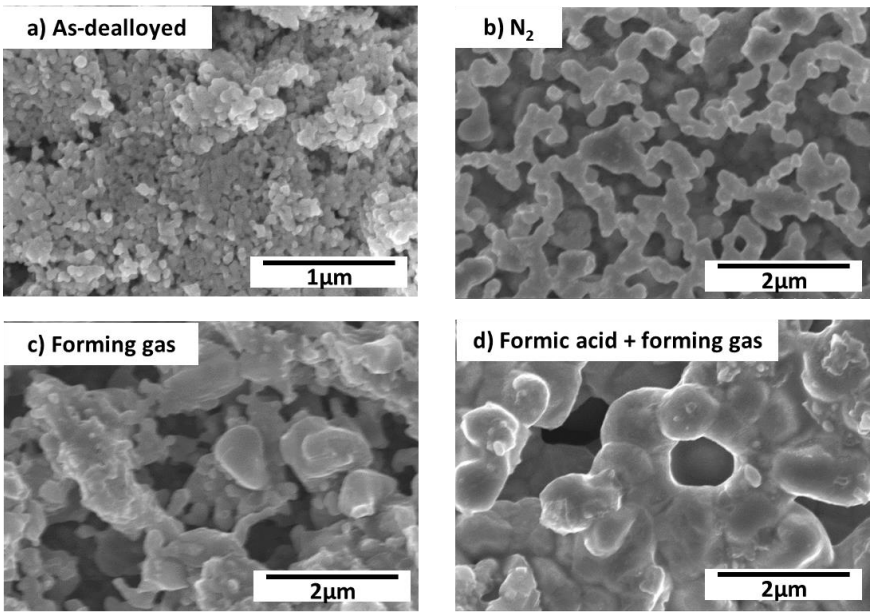

Figure 5.2 SEM images of NP-Cu: a) as fabricated; b-d) sintered at 275°C in different atmospheres.

5.2 Assembly demonstration using patterned NP-Cu films

To understand the bonding characteristics of patterned NP-Cu to bulk-Cu, thermocompression bonding was carried out on 3mm x 3mm patterned NP-Cu samples that acted as dies shown in Figure 5.3. Patterned Cu-Zn films with 46-48 at.% Zn were deposited on a Si substrate with Ti/Cu metallization on the open pads. The plated coupons were diced and subsequently dealloyed in 0.05MCl to fabricate dies with patterned NP-Cu films as shown in Figure 5.3.

The samples were bonded to 1cm x 1cm Si substrates with Cu metallizations. Before the assembly, the roughness of NP-Cu films and the Cu metallization on the substrates was analyzed using an optical profilometer. The average R_z, shown in Figure 5.4, was found to be 2.1µm for the patterned NP-Cu films and 0.96µm for the substrates. Both the NP-Cu samples and the Si substrates were dipped in 0.05M HCl for 15sec before assembly to

remove the Cu-oxides present on the surface. Assembly was carried out using a Finetech Matrix Fineplacer flip-chip bonder at 275°C for 60min in a 2% forming gas atmosphere. A bonding pressure of 10MPa was used for assembly.

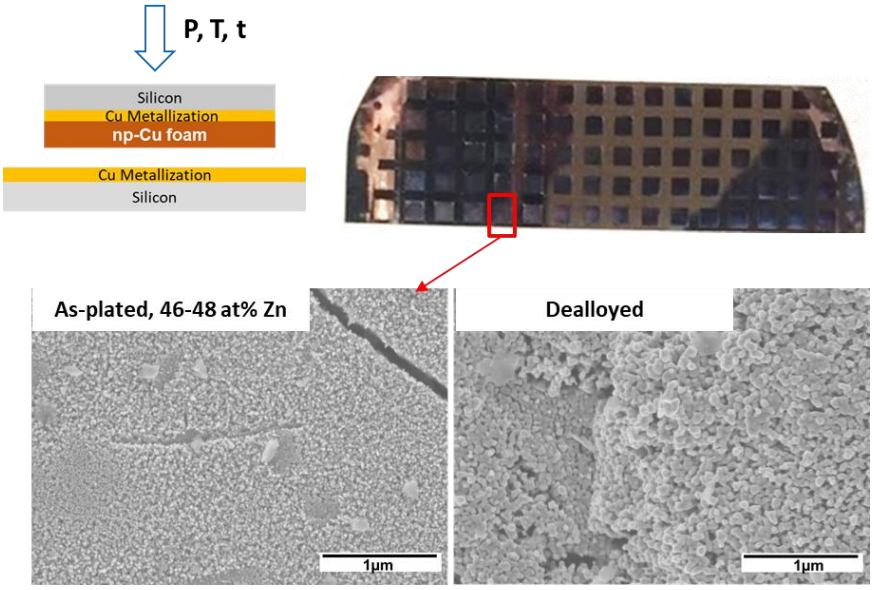

Figure 5.3 Schematic of the assembly stack up and patterned dies with NP-Cu films.

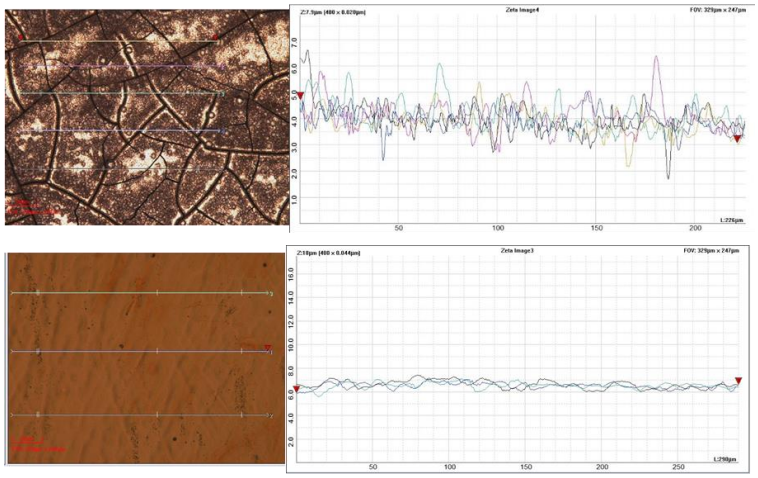

Figure 5.4 Roughness data for the die with NP-Cu film (top) and the substrate with Cu metallization (bottom).

To characterize the bond quality, shear tests were carried out using the XYZTEC Condor Sigma bond tester. Shear speed was maintained at 5µm/s and the shear height was set to 200µm from zero height (substrate-joint interface). A wide variation in the shear strengths of the Cu-Cu joints was observed as shown in Figure 5.5. The results can be divided into two groups – shear strengths < 20MPa and shear strengths > 38MPa.

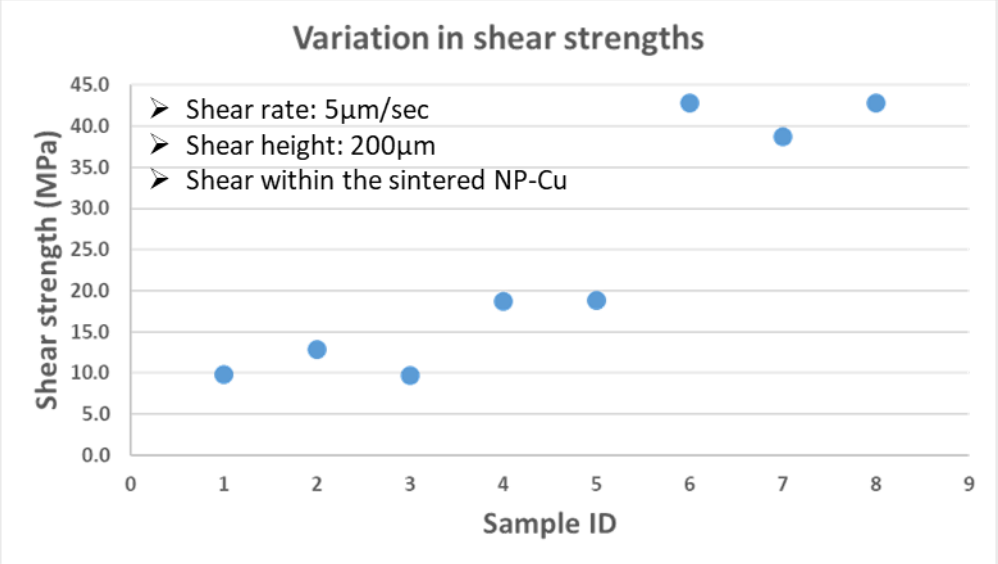

Figure 5.5 Variation in measured shear strengths after assembly.

Fracture surfaces of the sheared samples were analyzed using SEM and optical profilometer. The profilometer results on the die interface before and after assembly are shown in Figure 5.6. The NP-Cu film thickness before assembly was measured to be ~6.7µm. Upon shear, the fracture occurred within the sintered NP-Cu layer. The thickness of sintered NP-Cu film on the die after fracture was measured to be ~5.6µm. The associated shrinkage of the film was estimated at ~16%, which is a significant improvement over nanopastes which show shrinkage of >50% upon assembly.

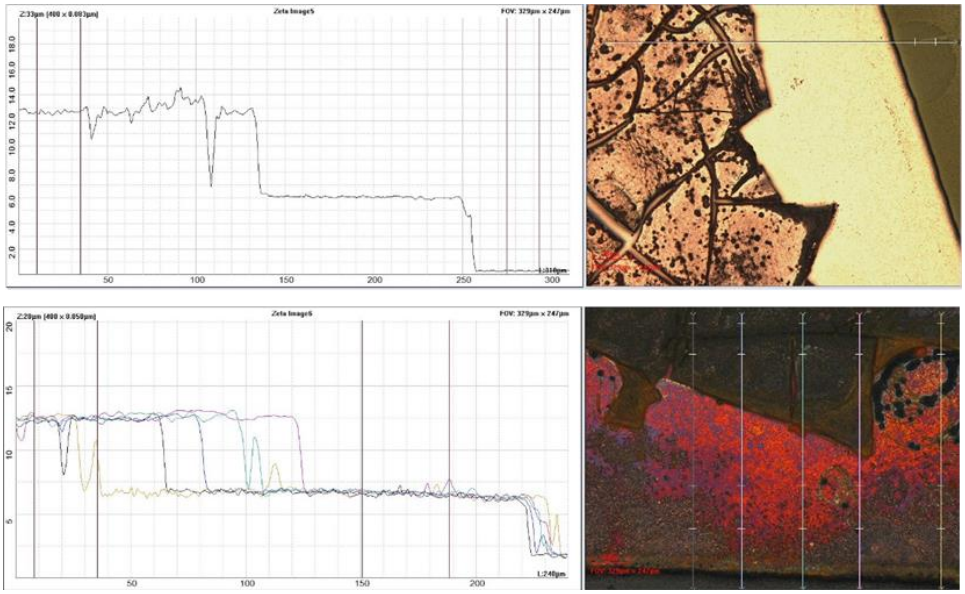

Figure 5.6 Profilometer measurements on the die bonding interface before and after assembly.

The SEM images of the fracture interface on the substrate are shown in Figure 5.7. Fracture interfaces of samples from both the groups (low and high shear strengths) were imaged. A very clear difference was observed between the two interfaces. The residual NP-Cu on the high shear strength sample fracture interface was observed to have significantly higher densification and ligament growth as compared to the lower shear strength sample fracture interface. Since the fracture mainly occurred within the sintered NP-Cu, a higher density sintered NP-Cu film will provide higher shear strengths.

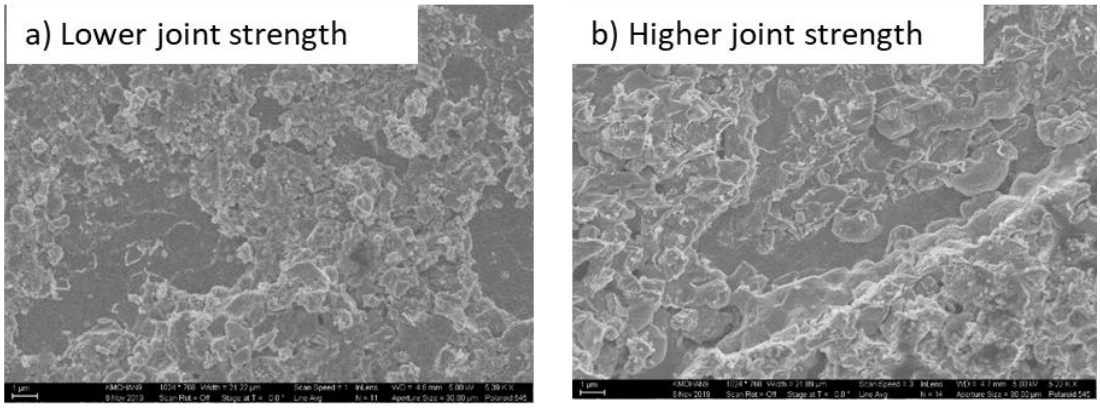

Figure 5.7 SEM images of the substrate-side fracture interfaces.

Though a high variation is observed, the initial results suggest that the sintering of NP-Cu films is a promising approach to realize Cu-Cu joints with joint strengths >40MPa. The assembly process development is still in its preliminary phase and more work needs to be done to yield Cu-Cu joints with consistent high shear strengths.

CHAPTER 6. RESEARCH SUMMARY AND CONCLUSIONS

Die-attach interconnections form a critical part of any power electronics packaging. Next-generation WBG devices-based power packages require die-attach solutions with excellent electrical and thermal properties and capable of operating at elevated temperatures greater than 200°C. This document proposed all-Cu die-attach joints as a potential solution to be realized by film sintering of nanoporous copper (NP-Cu).

All-Cu joints based on sintering of NP-Cu offer several advantages:

- Unlike nano-scale pastes, NP-systems are solid-state metastable systems and do not need organic additives for stabilization, thereby can enable sintered Cu joints without remnant organic residues, a major challenge with nanopastes.
- NP-Cu have low modulus, which can provide tolerance to surface roughness during assembly and compensate for lack of wettability.
- The nanostructure of the NP-Cu films can be easily tailored, giving versatility in assembly process design.
- The dealloying process is compatible with the industry bill of materials. Moreover, large-area sheets of NP-Cu can be fabricated, and subsequently diced into desired preform sizes and used as inserts for die-attach bonding, enabling scalability and a modular supply chain.

- NP-Cu films can be directly bonded on bare Cu metallization and do not need expensive passivation and surface treatments to deal with oxidation, making them further cost-effective over sintered Ag and Cu pastes.

To realize NP-Cu die-attach joints, two research tasks were identified and proposed: fabrication of large-area NP-Cu film and sintering and bonding demonstration using NP-Cu films.

6.1 Fabrication of large-area NP-Cu films

The objective of this task was to develop process guidelines for the fabrication of large-area NP-Cu films with excellent uniformity of the nanostructure. In the first phase, chemical dealloying of amorphous melt-spun alloys was carried out. Amorphous alloys were selected based on their advantages with respect to chemical dealloying. However, the dealloyed NP-Cu films developed cracks and warpage during dealloying, which is considered detrimental for die-attachment.

In the second phase, electroplating, and chemical dealloying of Cu-Zn alloys was proposed as an alternative to chemical dealloying of amorphous ribbons. An extensive characterization of the Cu-Zn plating bath was carried out which demonstrated the ability of pyrophosphate-based baths to be able to electroplate Cu-Zn alloys in a wide composition range. The Cu-Zn plated films were dealloyed to understand the impact of composition and constituent phases of the Cu-Zn films on dealloyed structure. Based on two key indicators – ligament thickness and residual Zn after dealloying, Zn ~50at.% was identified as the most promising composition for dealloying and fabrication of large-area die-attach films. The findings are to some extent contrary to the general trends in the literature. Prior reports

of dealloying of Cu-Zn alloys suggest the use of Zn-rich Cu-Zn alloys for the fabrication of NP-Cu films with the uniform nanostructure. However, the results from this study show beyond doubt that excellent dealloying behavior of Cu-Zn alloys for 33 at.%< Zn<50 at.%. Moving to a medium to low Zn Cu-Zn alloy also enhances the manufacturability of the process as Cu-Zn alloys with lower Zn content are easier to plate as compared to alloys with higher Zn content. Using the approach of co-electrodeposition and dealloying of Cu-Zn alloys, both standalone inserts and patterned NP-Cu films were fabricated for assembly. The fabrication results show the versatility of the fabrication approach in the sense that it can be used to fabricate NP-Cu films in several different form-factors for multiple applications using the same baseline process.

6.2 Demonstration of Cu-Cu joints by film sintering

To yield an all-Cu die-attach joint, NP-Cu films must be able to form metallurgical bonding interfaces with Cu finish on both the dies and substrates, as well as show high densification at temperatures as low as 250°C. Therefore, it is critical to understand the sintering behavior of NP-Cu films at different temperatures. The fabricated NP-Cu films were sintered at different temperatures. Coarsening and densification of the NP-Cu nanostructure were observed even at 200ºC. The effect of the reducing atmosphere on sintering was also studied and it was observed that the addition of formic acid enhances the sinterability considerably at 300ºC.

Based on the sintering results, 275-300ºC was identified as the optimal bonding temperature considering the limitations of the bonding equipment. Shear strengths of >40MPa were obtained when the assembly was carried out in forming gas.

In summary, this work demonstrates the potential of NP-Cu as the next generation die-attach material and provides guidelines for wafer-scale fabrication of NP-Cu films. NP-Cu has been proposed for use in several applications other than electrical interconnections like sensing, catalytic conversion, energy conversion, etc. Therefore, the results will be beneficial for the entire NP-metal community as it provides very extensive guidelines for the fabrication of NP-Cu films.

6.3 Technical and scientific contributions

- This research advances the understanding of chemical dealloying, and in particular, chemical dealloying of Cu-Zn alloys. More specifically, the relationship between plating parameters, Cu-Zn alloy composition, constituent phases, and chemical dealloying was extensively explored. The results provided very interesting insights, which sometimes were also contrary to the existing body of literature.

- A scientific in-depth analysis of the curvature change of the dealloyed films during dealloying was carried out using both experimental techniques and analytical modeling. A theory was proposed to explain the curvature change during dealloying. This fundamental understanding can be applied to design precursor alloys which do not show warpage during dealloying or can be potentially reverse-engineered to design precursor alloys which give NP-metal films with the desired curvature.

- The effect of temperature and reducing atmosphere on sintering of NP-Cu films was studied and the results proved the very high efficacy of formic acid in reducing Cu oxides and enabling strong Cu-Cu bonds. A new material system, nanoporous metals, has been demonstrated as an alternative to nanoscale pastes in electronics packaging.

REFERENCES

[1] *https://www.worldwildlife.org/pages/paris-climate-agreement.*

[2] *H.-P. Feustel, "Power electronics in hybrid and electric vehicles," in Postgraduate Summer School, 2016.*

[3] *https://tec.ieee.org/newsletter/november-december-2014/market-analysis-of-wideband-gap-devices-in-car-power-electronics.*

[4] Drevin-Bazin, A., F. Lacroix, and J.-F. Barbot, *SiC die attach for high-temperature applications.* Journal of electronic materials, 2014. **43**(3): p. 695-701.

[5] Su, M., C. Chen, and S. Rajan, *Prospects for the application of GaN power devices in hybrid electric vehicle drive systems.* Semiconductor Science and Technology, 2013. **28**(7): p. 074012.

[6] Fujihira, T., et al. *The State-of-The-Art and Future Trend of Power Semiconductor Devices*. in *Proceedings of PCIM Europe 2015; International Exhibition and Conference for Power Electronics, Intelligent Motion, Renewable Energy and Energy Management*. 2015.

[7] Yoon, S.W., et al., *Reliable and repeatable bonding technology for high temperature automotive power modules for electrified vehicles.* Journal of Micromechanics and Microengineering, 2012. **23**(1): p. 015017.

[8] *Presentation - Hitachi Metals, FCE 2016, Georgia Institute of Technology, Atlanta, USA.*

[9] Khazaka, R., et al., *Survey of high-temperature reliability of power electronics packaging components.* IEEE Transactions on power Electronics, 2014. **30**(5): p. 2456-2464.

[10] *https://www.powerelectronics.com/dc-dc-converters/selecting-die-attach-technology-high-power-applications#close-olyticsmodal.*

[11] Guth, K., et al. *End-of-life investigation on the .XT interconnect technology*. in *Proceedings of PCIM Europe 2015; International Exhibition and Conference for Power Electronics, Intelligent Motion, Renewable Energy and Energy Management*. 2015.

[12] Jiang, L., K. Ngo, and G.-q. Lu, *Thermo-Mechanical Reliability of Nano-Silver Sintered Joints versus Lead-Free Solder Joints for Attaching Large-Area Silicon Devices*. 2010, SAE International.

[13] Knoerr, M., S. Kraft, and A. Schletz. *Reliability assessment of sintered nano-silver die attachment for power semiconductors*. in *2010 12th Electronics Packaging Technology Conference*. 2010.

[14] *L.A.N. Melchor, 'Evaluation of die-attach materials for high temperature power electronics applications and analysis of Ag particles sintering solution" Doctoral thesis, UAB Barcelona, 2015.*

[15] Liu, H., et al., *Wafer-Level Cu/Sn to Cu/Sn SLID-Bonded Interconnects With Increased Strength.* IEEE Transactions on Components, Packaging and Manufacturing Technology, 2011. **1**(9): p. 1350-1358.

[16] Chuang, R.W. and C.C. Lee, *Silver-indium joints produced at low temperature for high temperature devices.* IEEE Transactions on Components and Packaging Technologies, 2002. **25**(3): p. 453-458.

[17] Mustain, H.A., W.D. Brown, and S.S. Ang, *Transient Liquid Phase Die Attach for High-Temperature Silicon Carbide Power Devices.* IEEE Transactions on Components and Packaging Technologies, 2010. **33**(3): p. 563-570.

[18] Yoon, S.W., et al. *Highly reliable nickel-tin transient liquid phase bonding technology for high temperature operational power electronics in electrified vehicles*. in *2012 Twenty-Seventh Annual IEEE Applied Power Electronics Conference and Exposition (APEC)*. 2012.

[19] Peng, P., et al., *Joining of Silver Nanomaterials at Low Temperatures: Processes, Properties, and Applications.* ACS Applied Materials & Interfaces, 2015. **7**(23): p. 12597-12618.

[20] Siow, K.S., *Are Sintered Silver Joints Ready for Use as Interconnect Material in Microelectronic Packaging?* Journal of Electronic Materials, 2014. **43**(4): p. 947-961.

[21] Kim, M.-S. and H. Nishikawa, *Effects of bonding temperature on microstructure, fracture behavior and joint strength of Ag nanoporous bonding for high temperature die attach.* Materials Science and Engineering: A, 2015. **645**: p. 264-272.

[22] Steppan, J., et al., *A review of corrosion failure mechanisms during accelerated tests electrolytic metal migration.* Journal of the electrochemical society, 1987. **134**(1): p. 175-190.

[23] Zhao, Y., et al. *Evaluation of Ag sintering die attach for high temperature power module applications*. in *2014 15th International Conference on Electronic Packaging Technology*. 2014.

[24] Le Henaff, F., et al. *Reliability of Double Side Silver Sintered Devices with various Substrate Metallization*. in *PCIM Europe 2016; International Exhibition and Conference for Power Electronics, Intelligent Motion, Renewable Energy and Energy Management*. 2016. VDE.

[25] Schnabl, K., et al., *Nanocopper Based Solder-Free Electronic Assembly.* Journal of Electronic Materials, 2014. **43**(12): p. 4515-4521.

[26] Schmitt, W. and L.M. Chew. *Silver Sinter Paste for SiC Bonding with Improved Mechanical Properties*. in *2017 IEEE 67th Electronic Components and Technology Conference (ECTC)*. 2017.

[27] https://www.ametek-ecp.com/-/media/ametek ecp/v2/files/cw_datasheets_sds_cfsi/datasheets/pb95sn5%20data%20sheet.pdf?la=en.

[28] Murray, J., *The Al− Zn (aluminum-zinc) system.* Bulletin of Alloy Phase Diagrams, 1983. **4**(1): p. 55-73.

[29] Karakaya, I. and W. Thompson, *The Ag-Bi (silver-bismuth) system.* Journal of phase equilibria, 1993. **14**(4): p. 525-530.

[30] MacDonald, W. and T. Eagar, *Transient liquid phase bonding.* Annual review of materials science, 1992. **22**(1): p. 23-46.

[31] Schwarzbauer, H. and R. Kuhnert. *Novel large area joining technique for improved power device performance*. in *Conference Record of the IEEE Industry Applications Society Annual Meeting*. 1989. IEEE.

[32] Zhang, Z. and G.-Q. Lu, *Pressure-assisted low-temperature sintering of silver paste as an alternative die-attach solution to solder reflow*. IEEE Transactions on electronics packaging manufacturing, 2002. **25**(4): p. 279-283.

[33] Kahler, J., et al., *Sintering of copper particles for die attach.* IEEE Transactions on Components, Packaging and Manufacturing Technology, 2012. **2**(10): p. 1587-1591.

[34] *http://www.indium.com/technical-documents/whitepaper/alternative-pbfree-soldering-alloys-english#paper-request-form.*

[35] Bultitude, J., J. McConnell, and C. Shearer, *High temperature capacitors and transient liquid phase interconnects for Pb-solder replacement.* Journal of Materials Science: Materials in Electronics, 2015. **26**(12): p. 9236-9242.

[36] Noguchi, M., S.N. Joshi, and E.M. Dede. *Design of Mechanical Properties of Transient Liquid Phase Bonds with Tertiary Metal Particles*. in *2016 IEEE 66th Electronic Components and Technology Conference (ECTC)*. 2016.

[37] Garnier, A., et al. *Investigation of copper-tin transient liquid phase bonding reliability for 3D integration*. in *2013 IEEE 63rd Electronic Components and Technology Conference*. 2013. IEEE.

[38] Manikam, V.R. and K.Y. Cheong, *Die attach materials for high temperature applications: A review*. IEEE Transactions on Components, Packaging and Manufacturing Technology, 2011. **1**(4): p. 457-478.

[39] Siow, K.S. and Y. Lin, *Identifying the development state of sintered silver (Ag) as a bonding material in the microelectronic packaging via a patent landscape study.* Journal of Electronic Packaging, 2016. **138**(2): p. 020804.

[40] Suganuma, K., et al., *Low-temperature low-pressure die attach with hybrid silver particle paste.* Microelectronics Reliability, 2012. **52**(2): p. 375-380.

[41] Paknejad, S.A. and S.H. Mannan, *Review of silver nanoparticle based die attach materials for high power/temperature applications.* Microelectronics Reliability, 2017. **70**: p. 1-11.

[42] Li, J., et al., *Bonding strength of multiple SiC die attachment prepared by sintering of Ag nanoparticles.* Journal of Materials Processing Technology, 2015. **215**: p. 299-308.

[43] Wang, M., et al. *Relationship between transient thermal impedance and shear strength of pressureless sintered silver as die attachment for power devices*. in *2015 International Conference on Electronics Packaging and iMAPS All Asia Conference (ICEP-IAAC)*. 2015. IEEE.

[44] Ogura, H., et al., *Carboxylate-passivated silver nanoparticles and their application to sintered interconnection: a replacement for high temperature lead-rich solders.* Journal of electronic materials, 2010. **39**(8): p. 1233-1240.

[45] Mei, Y.H., Z. Wang, and K.S. Siow, *Reliability and Failure Mechanisms of Sintered Silver as Die Attach Joint*, in *Die-Attach Materials for High Temperature Applications in Microelectronics Packaging: Materials, Processes, Equipment, and Reliability*, K.S. Siow, Editor. 2019, Springer International Publishing: Cham. p. 125-150.

[46] Khazaka, R., L. Mendizabal, and D. Henry, *Review on joint shear strength of nano-silver paste and its long-term high temperature reliability.* Journal of electronic materials, 2014. **43**(7): p. 2459-2466.

[47] Signor, L., et al., *Evolution of the thermal conductivity of sintered silver joints with their porosity predicted by the finite element analysis of real 3D microstructures.* Journal of Electronic Materials, 2018. **47**(7): p. 4170-4176.

[48] Carr, J., et al., *Quantitative characterization of porosity and determination of elastic modulus for sintered micro-silver joints.* Journal of Materials Processing Technology, 2015. **225**: p. 19-23.

[49] Gadaud, P., et al., *Ageing sintered silver: Relationship between tensile behavior, mechanical properties and the nanoporous structure evolution.* Materials Science and Engineering: A, 2016. **669**: p. 379-386.

[50] Ordonez-Miranda, J., et al., *Measurement and modeling of the effective thermal conductivity of sintered silver pastes.* International Journal of Thermal Sciences, 2016. **108**: p. 185-194.

[51] Le Henaff, F., et al., *Lifetime evaluation of nanoscale silver sintered power modules for automotive application based on experiments and finite-element modeling.* IEEE Transactions on Device and Materials Reliability, 2015. **15**(3): p. 326-334.

[52] Paret, P.P., D.J. DeVoto, and S.V.J. Narumanchi, *Thermomechanical Modeling of High-Temperature Bonded Interface Materials*, in *Die-Attach Materials for High Temperature Applications in Microelectronics Packaging: Materials, Processes, Equipment, and Reliability*, K.S. Siow, Editor. 2019, Springer International Publishing: Cham. p. 107-124.

[53] Yu, D.-j., et al., *Applying Anand model to low-temperature sintered nanoscale silver paste chip attachment.* Materials & Design, 2009. **30**(10): p. 4574-4579.

[54] Huang, J., et al. *FEM modelling of porosity in Ag sintering die attach for RF power applications*. in *2018 19th International Conference on Thermal, Mechanical and Multi-Physics Simulation and Experiments in Microelectronics and Microsystems (EuroSimE)*. 2018.

[55] Siow, K.S., *Mechanical properties of nano-silver joints as die attach materials.* Journal of Alloys and Compounds, 2012. **514**: p. 6-19.

[56] Qi, K., *Effect of interconnection area on shear strength of sintered joint with nano-silver paste.* Soldering & Surface Mount Technology, 2008. **20**(1): p. 8-12.

[57] Wang, T., et al., *Shrinkage and Sintering Behavior of a Low-Temperature Sinterable Nanosilver Die-Attach Paste.* Journal of Electronic Materials, 2012. **41**(9): p. 2543-2552.

[58] Zhang, H., S. Nagao, and K. Suganuma, *Addition of SiC particles to Ag die-attach paste to improve high-temperature stability; grain growth kinetics of sintered porous Ag.* Journal of Electronic Materials, 2015. **44**(10): p. 3896-3903.

[59] Le Henaff, F., et al. *Reliability of Double Side Silver Sintered Devices with various Substrate Metallization*. in *PCIM Europe 2016; International Exhibition and Conference for Power Electronics, Intelligent Motion, Renewable Energy and Energy Management; Proceedings of*. 2016. VDE.

[60] Sasaki, K. and N. Mizumura, *Development of low temperature sintered nano silver pastes using MO technology and resin reinforcing technology.* Additional Papers and Presentations, 2014. **2014**(HITEC): p. 000172-000177.

[61] Bhogaraju, S.K., et al., *Die-attach bonding for high temperature applications using thermal decomposition of copper(II) formate with polyethylene glycol.* Scripta Materialia, 2020. **182**: p. 74-80.

[62] Krishnan, S., A. Haseeb, and M.R. Johan, *Preparation and low-temperature sintering of Cu nanoparticles for high-power devices.* IEEE Transactions on Components, Packaging and Manufacturing Technology, 2012. **2**(4): p. 587-592.

[63] Gao, Y., et al., *Novel copper particle paste with self-reduction and self-protection characteristics for die attachment of power semiconductor under a nitrogen atmosphere.* Materials & Design, 2018. **160**: p. 1265-1272.

[64] Ren, H., et al., *Low temperature Cu bonding with large tolerance of surface oxidation.* AIP Advances, 2019. **9**(5): p. 055127.

[65] Ding, Y. and Z. Zhang, *Nanoporous Metals*, in *Springer Handbook of Nanomaterials*, R. Vajtai, Editor. 2013, Springer Berlin Heidelberg: Berlin, Heidelberg. p. 779-818.

[66] *L. J. Gibson and M. F. Ashby, Cellular solids: structure and properties: Cambridge university press, 1999.*

[67] *R. Liu and A. Antoniou, "Influence of dealloying parameters on the elastic response of nanoporous copper," in preparation.*

[68] R. Liu and A. Antoniou, *"A relationship between the geometrical structure of a nanoporous metal foam and its modulus,"* Acta Materialia, vol. 61, pp. 2390-2402, 4// 2013.

[69] G. Pia and F. Delogu, *"Coarsening of nanoporous Au: Relationship between structure and mechanical properties,"* Acta Materialia, vol. 99, pp. 29-38, 10/15/ 2015.

[70] Wang, J., et al., *Effect of thermal coarsening on the thermal conductivity of nanoporous gold.* Journal of materials science, 2012. **47**(12): p. 5013-5018.

[71] Xia, R., et al., *Correlation of the thermal and electrical conductivities of nanoporous gold.* Nanotechnology, 2010. **21**(8): p. 085703.

[72] Yang, Q., et al., *Preparation and properties of enhanced bulk nanoporous coppers.* Materials Letters, 2012. **73**: p. 136-138.

[73] Hakamada, M. and M. Mabuchi, *Fabrication, Microstructure, and Properties of Nanoporous Pd, Ni, and Their Alloys by Dealloying.* Critical Reviews in Solid State and Materials Sciences, 2013. **38**(4): p. 262-285.

[74] Li, K., et al. *Preparation and performances of nanoporous copper for low temperature bonding*. in *2014 15th International Conference on Electronic Packaging Technology*. 2014. IEEE.

[75] Liu, W., et al., *Dealloying solution dependence of fabrication, microstructure and porosity of hierarchical structured nanoporous copper ribbons.* Corrosion Science, 2015. **94**: p. 114-121.

[76] Mao, R., et al., *Effect of preparation conditions on morphology and thermal stability of nanoporous copper.* Corrosion Science, 2012. **60**: p. 231-237.

[77] Qi, Z., et al., *Formation and characterization of monolithic nanoporous copper by chemical dealloying of Al− Cu alloys.* The Journal of Physical Chemistry C, 2009. **113**(16): p. 6694-6698.

[78] Qiu, H.-J., et al., *Using corrosion to fabricate various nanoporous metal structures.* Corrosion Science, 2015. **92**: p. 16-31.

[79] Zhang, Z., et al., *Generalized fabrication of nanoporous metals (Au, Pd, Pt, Ag, and Cu) through chemical dealloying.* The Journal of Physical Chemistry C, 2009. **113**(29): p. 12629-12636.

[80] Artymowicz, D., J. Erlebacher, and R. Newman, *Relationship between the parting limit for de-alloying and a particular geometric high-density site percolation threshold.* Philosophical Magazine, 2009. **89**(21): p. 1663-1693.

[81] Sieradzki, K., *The Relationship Between Dealloying and Transgranular Stress-Corrosion Cracking of Cu-Zn and Cu-Al Alloys.* Journal of The Electrochemical Society, 1987. **134**(7): p. 1635.

[82] Wang, X., et al., *Influence of Alloy Composition and Dealloying Solution on the Formation and Microstructure of Monolithic Nanoporous Silver through Chemical Dealloying of Al−Ag Alloys.* The Journal of Physical Chemistry C, 2009. **113**(30): p. 13139-13150.

[83] Zhang, Z., et al., *Fabrication and characterization of nanoporous gold composites through chemical dealloying of two phase Al–Au alloys.* Journal of Materials Chemistry, 2009. **19**(33): p. 6042-6050.

[84] Chen, F., et al., *Fabrication and mechanical behavior of bulk nanoporous Cu via chemical de-alloying of Cu–Al alloys.* Materials Science and Engineering: A, 2016. **660**: p. 241-250.

[85] Hayes, J.R., et al., *Monolithic nanoporous copper by dealloying Mn–Cu.* Journal of Materials Research, 2011. **21**(10): p. 2611-2616.

[86] Mohan, K., et al. *Low-temperature, organics-free sintering of nanoporous copper for reliable, high-temperature and high-power die-attach interconnections*. in *2017 IEEE Applied Power Electronics Conference and Exposition (APEC)*. 2017. IEEE.

[87] Sun, S., et al., *Solderless bonding with nanoporous copper as interlayer for high-temperature applications.* Microelectronics Reliability, 2018. **80**: p. 198-204.

[88] Abe, H., et al., *Dealloying of Cu-Zr-Ti bulk metallic glass in hydrofluoric acid solution.* Materials transactions, 2009: p. 0905110765-0905110765.

[89] Dan, Z., et al., *Fabrication of nanoporous copper by dealloying of amorphous Ti–Cu–Ag alloys.* Journal of Alloys and Compounds, 2014. **586**: p. S134-S138.

[90] Dan, Z., et al., *Nickel-stabilized nanoporous copper fabricated from ternary TiCuNi amorphous alloys.* Materials Letters, 2013. **94**: p. 128-131.

[91] Wang, Z., et al., *Fabrication and new electrochemical properties of nanoporous Cu by dealloying amorphous Cu–Hf–Al alloys.* Intermetallics, 2015. **56**: p. 48-55.

[92] El Ashram, T., A.P. Carapeto, and A.M.B. do Rego, *Rapidly Solidified Melt-spun Bi-Sn Ribbons: Surface Composition Issues.* Journal: JOURNAL OF ADVANCES IN PHYSICS, 2016. **11**(5).

[93] Ibru, T., et al., *Structure and mechanical behavior of dentin-inspired nanoporous copper*. 2020. **176**: p. 99-103.

[94] Liu, R., et al., *Synthesis and mechanical behavior of nanoporous nanotwinned copper*. Applied Physics Letters, 2013. **103**(24): p. 241907.

[95] Liu, R. and A. Antoniou, *A relation between relative density, alloy composition and sample shrinkage for nanoporous metal foams.* Scripta Materialia, 2012. **67**(12): p. 923-926.

[96] Ma, K., et al., *Origin of the Volume Contraction during Nanoporous Gold Formation by Dealloying for High-Performance Electrochemical Applications.* ACS Applied Nano Materials, 2018. **1**(2): p. 541-546.

[97] Parida, S., et al., *Volume change during the formation of nanoporous gold by dealloying.* Physical Review Letters, 2006. **97**(3): p. 035504.

[98] Seker, E., M.L. Reed, and M.R. Begley, *Nanoporous Gold: Fabrication, Characterization, and Applications.* Materials, 2009. **2**(4): p. 2188-2215.

[99] Paschalidou, E., et al., *The mechanism of generating nanoporous Au by de-alloying amorphous alloys.* 2016. **119**: p. 177-183.

[100] Li, W.-C. and T.J. Balk, *Effects of substrate curvature on dealloying of nanoporous thin films.* Scripta Materialia, 2009. **61**(12): p. 1125-1128.

[101] *http://www2.ucdsb.on.ca/tiss/stretton/database/Standard_Reduction_Potentials.htm*.

[102] Ballesteros, J., et al., *Study of the electrochemical co-reduction of Cu2+ and Zn2+ ions from an alkaline non-cyanide solution containing glycine.* Journal of Electroanalytical Chemistry, 2014. **727**: p. 104-112.

[103] Carlos, I.A. and M.R.H. de Almeida, *Study of the influence of the polyalcohol sorbitol on the electrodeposition of copper–zinc films from a non-cyanide bath.* Journal of Electroanalytical Chemistry, 2004. **562**(2): p. 153-159.

[104] Chen, P.Y., M.C. Lin, and I.W. Sun, *Electrodeposition of Cu-Zn alloy from a Lewis acidic ZnCl 2-EMIC molten salt.* Journal of the Electrochemical Society, 2000. **147**(9): p. 3350-3355.

[105] De Almeida, M., et al., *Copper–zinc electrodeposition in alkaline-sorbitol medium: Electrochemical studies and structural, morphological and chemical composition characterization.* Applied Surface Science, 2015. **333**: p. 13-22.

[106] Ferreira, F., et al., *Response surface modeling and optimization to study the influence of deposition parameters on the electrodeposition of Cu–Zn alloys in citrate medium.* Journal of Applied Electrochemistry, 2007. **37**(4): p. 473-481.

[107] Machado, V.C., A.M. Schmidt, and D.S. Azambuja, *Electrodissolution of Cu-Zn alloys in acetate media.* Journal of the Brazilian Chemical Society, 2000. **11**(4): p. 387-392.

[108] Senna, L.d., S. Díaz, and L. Sathler, *Electrodeposition of copper–zinc alloys in pyrophosphate-based electrolytes.* Journal of Applied Electrochemistry, 2003. **33**(12): p. 1155-1161.

[109] Survila, A., et al., *Codeposition of zinc and copper in gluconate-sulfate solutions.* Journal of The Electrochemical Society, 2013. **160**(10): p. D428.

[110] *http://theses.ncl.ac.uk/jspui/handle/10443/470.*

[111] Vivegnis, S., et al., *Copper–zinc alloy electrodeposition mediated by triethanolamine as a complexing additive and chemical dealloying.* Electrochimica Acta, 2019. **319**: p. 400-409.

[112] Vivegnis, S., et al., *Use of pyrophosphate and boric acid additives in the copper-zinc alloy electrodeposition and chemical dealloying.* Journal of Electroanalytical Chemistry, 2019. **848**: p. 113310.

[113] Özdemir, R. and İ. Karahan, *Effect of solution Zn concentration on electrodeposition of Cu x Zn1–x alloys: materials and resistivity characterisation.* Transactions of the IMF, 2019. **97**(2): p. 95-99.

[114] Özdemir, R., İ.H. Karahan, and O. Karabulut, *A study on the electrodeposited Cu-Zn alloy thin films.* Metallurgical and Materials Transactions A, 2016. **47**(11): p. 5609-5617.

[115] Yue, H., et al. *A Preparation Method of Patterned Nanoporous Copper*. in *Advanced Materials Research*. 2013. Trans Tech Publ.

[116] Senna, L.F.d., S.L. Díaz, and L. Sathler, *Hardness analysis and morphological characterization of copper-zinc alloys produced in pyrophosphate-based electrolytes.* Materials Research, 2005. **8**(3): p. 275-279.

[117] Tuan, N.T., et al., *Synthesis of nanoporous Cu films by dealloying of electrochemically deposited Cu–Zn alloy films.* Corrosion Science, 2014. **80**: p. 7-11.

[118] Ibru, T., et al., *Structure and mechanical behavior of dentin-inspired nanoporous copper.* Scripta Materialia, 2020. 176: p. 99-103.

[119] Coble, R. L., 1961. "Sintering Crystalline Solids. I. Intermediate and Final State Diffusion Models", Journal of Applied Physics, Vol. 32, No. 5, pp. 787–792.

[120] Chen, A., et al., Effect of annealing atmosphere on the thermal coarsening of nanoporous gold films. Applied Surface Science, 2015. 355: p. 133-138.

[121] Chen-Wiegart, Y.-c.K., et al., Structural evolution of nanoporous gold during thermal coarsening. Acta Materialia, 2012. 60(12): p. 4972-4981.

[122] Fang, Z. and H. Wang, Densification and grain growth during sintering of nanosized particles. International Materials Reviews, 2008. 53(6): p. 326-352.